



VRIJE
UNIVERSITEIT
BRUSSEL

¹ **A search for flavour changing neutral currents
2 involving a top quark and a Z boson, using the
3 data collected by the CMS collaboration at a
4 centre-of-mass energy of 13 TeV**

⁵ Isis Van Parijs

⁶ Proefschrift ingediend met het oog op het behalen van de academische graad
⁷ Doctor in de Wetenschappen.

Published in Faculteit Wetenschappen & Bio-ingenieurswetenschappen
Vrije Universiteit Brussel
At 10 November 2017.

⁸

Responsible Contact: Isis Van Parijs
Intitute for High Energy Physics
Promotor: Prof. Jorgen D'Hondt

9 First Referee: Prof. Dr. J. D'Hondt
 Date of Hand-in: 10 November 2017
 Date of Defense: 10 December 2017

Contents

| | | |
|----|---|----|
| 11 | 1 Theoretical basis | 1 |
| 12 | 1.1 Elementary particles and forces | 1 |
| 13 | 1.2 Standard Model Lagrangian, connecting fields with particles | 2 |
| 14 | 1.3 Flavours in the SM | 5 |
| 15 | 1.4 The top quark in the SM | 6 |
| 16 | 1.5 Experimental results on the SM top quark | 9 |
| 17 | 1.6 Motivation for new physics | 13 |
| 18 | 1.7 An effective approach beyond the SM: FCNC involving a top quark | 14 |
| 19 | 1.8 Experimental constraints on top-FCNC | 16 |
| 20 | 2 Experimental set-up | 19 |
| 21 | 2.1 The Large Hadron Collider | 19 |
| 22 | 2.2 The Compact Muon Solenoid | 22 |
| 23 | 2.2.1 CMS coordinate system | 23 |
| 24 | 2.2.2 Towards the heart of CMS | 24 |
| 25 | 2.2.3 Data acquisition | 32 |
| 26 | 2.2.4 Phase 1 upgrades | 32 |
| 27 | 2.2.5 CMS computing model | 34 |
| 28 | 3 Analysis techniques | 37 |
| 29 | 3.1 Hadron collisions at high energies | 37 |
| 30 | 3.2 Event generation | 40 |
| 31 | 3.2.1 Fundamentals of simulating a proton collision | 40 |
| 32 | 3.2.2 Programs for event generation | 40 |
| 33 | 3.2.3 Generating FCNC top-Z interactions | 42 |
| 34 | 3.2.4 Generating SM background events | 44 |
| 35 | 3.3 Multivariate analysis techniques: Boosted Decision Trees | 46 |
| 36 | 3.4 Statistical methodology | 48 |
| 37 | 3.4.1 The absence of signal: limits | 49 |
| 38 | 3.4.2 Adding sources of uncertainty | 51 |
| 39 | 3.4.3 Asymptotic approximation of the CL method | 52 |
| 40 | 3.4.4 Extracting the signal model parameters | 52 |
| 41 | 4 Event reconstruction and identification | 53 |

| | | |
|----|--|------|
| 42 | 4.1 Object Reconstruction | 53 |
| 43 | 4.1.1 Charged particle tracks | 54 |
| 44 | 4.1.2 Following the Muon's Footsteps | 55 |
| 45 | 4.1.3 The path of the Electron | 56 |
| 46 | 4.1.4 Primary Vertex Reconstruction | 57 |
| 47 | 4.1.5 Calorimeter clusters | 57 |
| 48 | 4.2 Putting the pieces together | 58 |
| 49 | 4.3 Particle flow identification | 59 |
| 50 | 4.3.1 Muons | 59 |
| 51 | 4.3.2 Electrons and isolated photons | 59 |
| 52 | 4.3.3 Hadrons and non-isolated photons | 59 |
| 53 | 4.3.4 Post processing | 60 |
| 54 | 4.4 Pile up mitigation and luminosity measurement | 60 |
| 55 | 4.5 Physics object reconstruction and identification | 61 |
| 56 | 4.5.1 Muons | 61 |
| 57 | 4.5.2 Electrons | 64 |
| 58 | 4.5.3 Jets | 66 |
| 59 | 4.5.4 Jets from b fragmentation | 68 |
| 60 | 4.5.5 Missing transverse energy | 71 |
| 61 | 4.6 Summary of corrections | 71 |
| 62 | 5 Event selection and categorisation | 73 |
| 63 | 5.1 Baseline event selection and filters | 73 |
| 64 | 5.1.1 Event cleaning | 76 |
| 65 | 5.1.2 Estimation of the trigger efficiency | 77 |
| 66 | 5.1.3 Corrections | 79 |
| 67 | 5.2 Analysis Strategy | 83 |
| 68 | 5.3 Data driven NPL background simulation | 83 |
| 69 | 5.4 Regions and channels | 85 |
| 70 | 5.4.1 WZ control region | 86 |
| 71 | 5.4.2 TTCR and STCR | 87 |
| 72 | 5.4.3 TTSR and STSR | 88 |
| 73 | 6 The search for FCNC involving a top quark and a Z boson | 89 |
| 74 | 6.1 Construction of template distributions | 89 |
| 75 | 6.2 Systematic uncertainties | 89 |
| 76 | 6.3 Limit setting procedure | 89 |
| 77 | 6.4 Result and discussion | 89 |
| 78 | 7 Denouement of the top-Z FCNC hunt at 13 TeV | 91 |
| 79 | Appendices | 91 |
| 80 | A Trigger scale factors | 93 |
| 81 | B Dilepton controlplots | 105■ |

CONTENTS

v

| | | |
|----|--|-------------|
| 82 | C Statistical independent regions | 107■ |
| 83 | Bibliography | 109■ |

Theoretical basis

1

85 The Standard Model (SM) [1] is a name given in the 1970s to a theory describing the fundamental
 86 particles and their interactions. This quantum field theory describes the particles and their
 87 interactions as fields and has successfully incorporated three of the four fundamental forces in
 88 the universe. In [Section 1.1](#), the particle content of the SM is summarised, while [Section 1.2](#)
 89 describes the SM Lagrangian and its symmetries. In [Section 1.3](#), the flavour content of the SM
 90 is highlighted, and [Section 1.4](#) focusses on the top quark in the SM. The latest experimental
 91 results related to the properties of the top quark are summarised in [Section 1.5](#).

92 The successful theory of the SM has some shortcomings which are discussed in [Section 1.6](#)
 93 and lead to searches for a more general theory. One of such is using an effective field theory
 94 (EFT) approach [2] to search for new physics in a model independent way. In [Section 1.7](#) an
 95 EFT model focussing on flavour changing neutral currents (FCNC) involving a top quark is
 96 presented. Its current experimental constraints are given in [Section 1.8](#).

97 1.1 Elementary particles and forces

98 The interactions in nature can be described by four forces, the strong force, the electromagnetic
 99 (EM) force, the weak force and the gravitational force. These interactions happen via particles
 100 with an integer spin known as bosons. The strong interaction is mediated by eight gluons g ,
 101 while the electromagnetic force is mediated by photons γ , and the weak force by Z and W^\pm
 102 bosons. In [Table 1.1](#), the forces and their characteristics are shown. The gravitational force is
 103 the only force not included in the SM and can be neglected for energies lower than the Planck
 scale (1.22×10^{19} GeV).

Table 1.1: The four forces of nature and their characteristics.

| | Range | Mediator |
|-----------------------|--------------|--------------------|
| Strong force | 10^{-15} m | 8 gluons |
| Electromagnetic force | ∞ | photon |
| Weak force | 10^{-18} m | W^\pm , Z bosons |
| Gravitational force | ∞ | unknown |

The fermions are the particles that make up the visible matter in the universe. They carry half integer spin and can be subdivided into leptons and quarks, where leptons do not interact strongly. Each fermion has a corresponding anti-fermion which has the same mass and is oppositely charged. The electron e is the first elementary particle discovered [3] and belongs to the first generation of leptons together with the electron neutrino ν_e . The second generation comprises the muon μ and muon neutrino ν_μ , whereas the third generation consists of the tau τ and tau neutrino ν_τ . The neutrinos are neutral particles, while the other leptons have charge $\pm q_e$ with q_e representing the elementary charge of 1.602×10^{-19} C. The masses of charged leptons differ by four orders of magnitude between the first and third generations. In the SM the neutrinos are assumed to be massless, nonetheless it is experimentally established that neutrinos do have a tiny non-zero mass [4, 5]. In Table 1.2, the leptons and their properties in the SM are summarised.

Table 1.2: The properties of the leptons in the three generations of the SM [6], where q_e represents the elementary charge.

| Generation | Particle | Mass | Charge |
|------------|------------|-------------|--------|
| First | e^- | 0.511 MeV | $-q_e$ |
| | ν_e | ≈ 0 | 0 |
| Second | μ^- | 106 MeV | $-q_e$ |
| | ν_μ | ≈ 0 | 0 |
| Third | τ^- | 1 777 MeV | $-q_e$ |
| | ν_τ | ≈ 0 | 0 |

116

The quarks can also be divided into three generations. Unlike the leptons, they carry colour charge and can interact via the strong interaction. The top quark, discovered in 1995 at the Tevatron [7, 8], is the heaviest SM particle with a mass¹ measured to be $173.34 \pm 0.27(\text{stat}) \pm 0.71(\text{syst})$ GeV [9]. The quarks and their properties are summarised in Table 1.3. In nature, only colour neutral objects can exist. This has as consequence that quarks are bound through gluons into mesons (quark+anti-quark) and baryons (three quarks). These mesons and baryons are mostly short-lived and unstable particles that rapidly decay through W^\pm and Z bosons. The only known stable baryon is the proton, made up of two up quarks and one down quark.

The scalar boson, commonly known as the Higgs boson, is the last piece of the SM discovered in 2012 [10, 11]. It is responsible for the masses of the W^\pm and Z boson, and that of the fermions.

1.2 Standard Model Lagrangian, connecting fields with particles

The SM is a quantum field theory and thus describes the dynamics and kinematics of particles and forces by a Lagrangian \mathcal{L} . The theory is based on the $SU(3)_C \times SU(2)_L \times U(1)_Y$ gauge

¹In this thesis all masses and energies are expressed in natural units, where the speed of light and \hbar are taken to be equal to one.

Table 1.3: The properties of the quarks in the three generations of the SM [6], where q_e represents the elementary charge.

| | Generation | Particle | Mass | Charge |
|--------|------------|----------------------------|--------------------|--------|
| First | up u | $2.2^{+0.6}_{-0.4}$ MeV | $\frac{2}{3} q_e$ | |
| | down d | $4.7^{+0.5}_{-0.4}$ MeV | $\frac{-1}{3} q_e$ | |
| Second | charm c | 1.28 ± 0.03 GeV | $\frac{2}{3} q_e$ | |
| | strange s | 96^{+8}_{-4} MeV | $\frac{-1}{3} q_e$ | |
| Third | top t | 173.1 ± 0.6 GeV | $\frac{2}{3} q_e$ | |
| | bottom b | $4.18^{+0.04}_{-0.03}$ GeV | $\frac{-1}{3} q_e$ | |

132 symmetry, where $SU(2)_L \times U(1)_Y$ describes the electroweak interaction and $SU(3)_C$ the strong
 133 interaction. The indices refer to colour C, the left chiral nature of the $SU(2)_L$ coupling L,
 134 and the weak hypercharge Y. Its Lagrangian is constructed such that contains symmetries
 135 representing physics conservation laws such as conservation of energy, momentum and angular
 136 momentum. The symmetries under local gauge transformations are sustained by demanding
 137 gauge invariance².

The $U(1)_Y$ group has one generator Y with an associated gauge field B_μ . The three gauge fields W_μ^1 , W_μ^2 , and W_μ^3 , are associated to $SU(2)_L$ with three generators that can be written as half of the Pauli matrices:

$$T_1 = \frac{1}{2} \begin{pmatrix} 0 & 1 \\ 1 & 0 \end{pmatrix}, \quad T_2 = \frac{1}{2} \begin{pmatrix} 0 & -i \\ i & 0 \end{pmatrix}, \quad T_3 = \frac{1}{2} \begin{pmatrix} 1 & 0 \\ 0 & -1 \end{pmatrix}. \quad (1.1)$$

The generators T^a satisfy the Lie algebra:

$$[T_a, T_b] = i\epsilon_{abc} T^c \text{ and } [T_a, Y] = 0, \quad (1.2)$$

138 where ϵ_{abc} is an antisymmetric tensor. The gauge fields of $SU(2)_L$ only couple to left-handed
 139 fermions as required by the observed parity violating nature of the weak force. The $SU(3)_C$
 140 group represents quantum chromodynamics (QCD). It has eight generators corresponding to
 141 eight gluon fields $G_\mu^{1..8}$. Unlike $SU(2)_L \times U(1)_Y$, $SU(3)_C$ is not chiral.

Under $SU(3)_C$ quarks are colour triplets while leptons are colour singlets. This implies that the quarks carry a colour index ranging between one and three, whereas leptons do not take part in strong interactions. Based on the chirality, the quarks and leptons are organized in doublets or singlets. Each generation i of fermions consists of left-handed doublets and right-handed singlets:

$$l_{L,i} = \begin{pmatrix} e_{L,i} \\ \nu_{L,i} \end{pmatrix}, \quad e_{R,i}, \quad q_{L,i} = \begin{pmatrix} u_{L,i} \\ d_{L,i} \end{pmatrix}, \quad u_{R,i}, \quad \text{and } d_{R,i} \quad (1.3)$$

²Different field configurations of unobservable fields can result in identical quantities. Transformations between such configurations are called gauge transformation and the absence of change in the measurable quantities is a characteristic called gauge invariance.

The SM Lagrangian can be decomposed as a sum of four terms

$$\mathcal{L}_{\text{SM}} = \mathcal{L}_{\text{gauge}} + \mathcal{L}_f + \mathcal{L}_{\text{Yuk}} + \mathcal{L}_\phi, \quad (1.4)$$

that are related to the gauge, fermion, Yukawa and scalar sectors. The gauge Lagrangian regroups the gauge fields of all three symmetry groups, and the fermionic part consists of kinetic energy terms for quarks and leptons. The interaction between fermions and the scalar doublet ϕ gives rise to fermion masses and is described by the Yukawa Lagrangian. The scalar part of the Lagrangian is composed of a kinematic and potential component related to the scalar boson.

For the electroweak theory, two coupling constants are introduced, namely g' for $U(1)_Y$ and g for $SU(2)_L$. The physically observable gauge bosons of this theory are the photon field A_μ , the Z boson field Z_μ^0 , and the W boson fields W_μ^\pm . These are a superposition of the four gauge fields of $SU(2)_L \times U(1)_Y$:

$$A_\mu = \sin\theta_W W_\mu^3 + \cos\theta_W B_\mu, \quad Z_\mu^0 = \cos\theta_W W_\mu^3 - \sin\theta_W B_\mu, \quad \text{and} \quad W_\mu^\pm = \sqrt{\frac{1}{2}} (W_\mu^1 \mp i W_\mu^2), \quad (1.5)$$

where θ_W represents the weak mixing angle defined as $\tan\theta_W = \frac{g'}{g}$.

The coupling constant representing the strength of the QCD interactions is denoted as g_s . In QCD there is asymptotic freedom whereby the strong coupling constant becomes weaker as the energy with which the interaction between strongly interacting particles is probed increases, and stronger as the distance between the particles increases. A consequence of this is known as colour confinement, the quarks and gluons can not exist on their own and are not observed individually. They are bound in colour neutral states called hadrons, this process is known as hadronisation.

Electroweak symmetry breaking

In $\mathcal{L}_{\text{gauge}}$ and \mathcal{L}_f are no mass terms for fermions present because only singlets under $SU(3)_C \times SU(2)_L \times U(1)_Y$ can acquire a mass with an interaction of the type $m^2 \phi^\dagger \phi$ without breaking the gauge invariance. In order to accommodate mass terms for fermions and gauge fields, electroweak symmetry breaking, leading to \mathcal{L}_ϕ is introduced.

The scalar doublet is introduced in the SM as

$$\phi = \frac{1}{\sqrt{2}} \begin{pmatrix} \varphi_1 + i\varphi_2 \\ \varphi_3 + i\varphi_4 \end{pmatrix}. \quad (1.6)$$

Its field potential is of the form

$$V(\phi) = \mu^2 \phi^\dagger \phi + \lambda (\phi^\dagger \phi)^2, \quad (1.7)$$

with $\mu^2 < 0$ and λ a positive integer. This choice of parameters gives the potential a "Mexican hat" shape. It has an infinite set of minima (ground states) and by expanding the field around an arbitrary choice of ground state, the electroweak symmetry is broken (EW):

$$\phi = \begin{pmatrix} 0 \\ \frac{v}{\sqrt{2}} \end{pmatrix} + \hat{\phi}, \quad (1.8)$$

where v is the vacuum expectation value (vev), measured to be around 245 GeV and corresponds to $\sqrt{\frac{-\mu}{\lambda}}$. The scalar doublet's four degrees of freedom are reduced to three degrees of freedom that couple to the gauge fields and fix the W^+ , W^- and Z bosons. The remaining fourth degree of freedom has given rise to a physically observable particle, called the Brout-Englert-Higgs (BEH) boson. This spontaneous symmetry breaking leaves the gauge invariance intact and gives masses to the W^\pm and Z bosons as:

$$m_W = \frac{1}{2}v|g| \quad \text{and} \quad m_Z = \frac{1}{2}v\sqrt{g'^2 + g^2}. \quad (1.9)$$

- 160 The Brout-Englert-Higgs field couples universally to fermions with a strength proportional to
161 their masses, and to gauge bosons with a strength proportional to the square of their masses.

162 1.3 Flavours in the SM

Flavour changing charged currents are introduced in 1963 by Nicola Cabibbo [12]. Via interactions with a W boson the flavour of the quarks is changed. At the time of the postulation only up, down, and strange quarks were known and the charged weak current was described as a coupling between the up quark and d_{weak} , where d_{weak} is a linear combination of the down and strange quarks, $d_{\text{weak}} = \cos\theta_c d + \sin\theta_c s$. This linear combination is a direct consequence of the chosen rotation

$$\begin{pmatrix} d_{\text{weak}} \\ s_{\text{weak}} \end{pmatrix} = \begin{pmatrix} \cos\theta_c & \sin\theta_c \\ -\sin\theta_c & \cos\theta_c \end{pmatrix} \begin{pmatrix} d \\ s \end{pmatrix} = \mathcal{R} \begin{pmatrix} d \\ s \end{pmatrix}, \quad (1.10)$$

where the rotation angle θ_c is known as the Cabibbo angle. This provides a definition for the charged weak current between u and d quarks,

$$J_\mu = \bar{u}\gamma_\mu(1 + \gamma_5)d_{\text{weak}}. \quad (1.11)$$

A consequence of Cabibbo's approach is that the s_{weak} is left uncoupled, leading to Glashow, Iliopoulos and Maiani (GIM) [13–15] to require the existence of a fourth quark with charge $\frac{2}{3}q_e$. This quark, known as the charm quark, couples to s_{weak} and a new definition of the charged weak current is modified to

$$J_\mu = (\bar{u} \quad \bar{c}) \gamma_\mu (1 + \gamma_5) \mathcal{R} \begin{pmatrix} d \\ s \end{pmatrix} = \bar{U} \gamma_\mu (1 + \gamma_5) \mathcal{R} D. \quad (1.12)$$

The neutral weak current is defined as

$$J_3 = \bar{U} \gamma_\mu (1 + \gamma_5) [\mathcal{R}, \mathcal{R}^\dagger] D, \quad (1.13)$$

- 163 and is diagonal in flavour space. This has as consequence that no flavour changing neutral
164 currents occur at tree-level interactions [1].

Kobayashi and Maskawa generalised the Cabibbo rotation matrix to accommodate a third generation of quarks. The result is a 3×3 unitary matrix known as the CKM matrix, responsible

for the mixing of weak interaction states of down-type quarks:

$$\begin{pmatrix} d_{\text{weak}} \\ s_{\text{weak}} \\ b_{\text{weak}} \end{pmatrix} = \begin{pmatrix} V_{ud} & V_{us} & V_{ub} \\ V_{cd} & V_{cs} & V_{cb} \\ V_{td} & V_{ts} & V_{tb} \end{pmatrix} \begin{pmatrix} d \\ s \\ b \end{pmatrix} = \mathcal{V}_{\text{CKM}} \begin{pmatrix} d \\ s \\ b \end{pmatrix}, \quad (1.14)$$

where \mathcal{V}_{CKM} is unitary ($\mathcal{V}_{\text{CKM}}^\dagger \mathcal{V}_{\text{CKM}} = \mathbb{1}$). A general 3×3 unitary matrix depends on three real angles and six phases. For the CKM matrix, the freedom to redefine the phases of the quark eigenstates can remove five of the phases, leaving a single physical phase known as the Kobayashi-Maskawa phase. This phase is responsible for the charge parity violation in the SM [16]. Each element V_{ij} of \mathcal{V}_{CKM} represents the transition probability of a quark i going to a quark j , and is experimentally determined to be [6]

$$\mathcal{V}_{\text{CKM}} = \begin{pmatrix} 0.97425 \pm 0.00022 & 0.2253 \pm 0.0008 & (4.13 \pm 0.49) 10^{-3} \\ 0.225 \pm 0.008 & 0.986 \pm 0.016 & (41.1 \pm 1.3) 10^{-3} \\ (8.4 \pm 0.6) 10^{-3} & (40.0 \pm 2.7) 10^{-3} & 1.021 \pm 0.032 \end{pmatrix}. \quad (1.15)$$

165 From Equation 1.15 follows that top quarks predominantly decay via charged weak currents
 166 to bottom quarks, with a probability consistent with unity. In the SM, FCNC can only occur via
 167 higher loop interactions which are highly suppressed. The expected transition probabilities for
 168 a top quark decaying via a FCNC interaction in the SM are given in Table 1.4, where it is clear
 169 that the FCNC top quark interactions of the SM is still beyond the reach of the sensitivity of
 current experiments.

Table 1.4: The predicted branching ratios \mathcal{B} for FCNC decays involving the top quark in the SM [17].

| Process | \mathcal{B} in the SM | Process | \mathcal{B} in the SM |
|-------------------------|-------------------------|-------------------------|-------------------------|
| $t \rightarrow uZ$ | $8 \cdot 10^{-17}$ | $t \rightarrow cZ$ | $1 \cdot 10^{-14}$ |
| $t \rightarrow u\gamma$ | $4 \cdot 10^{-16}$ | $t \rightarrow c\gamma$ | $5 \cdot 10^{-14}$ |
| $t \rightarrow ug$ | $4 \cdot 10^{-14}$ | $t \rightarrow cg$ | $5 \cdot 10^{-12}$ |
| $t \rightarrow uH$ | $2 \cdot 10^{-17}$ | $t \rightarrow cH$ | $3 \cdot 10^{-15}$ |

170

171 1.4 The top quark in the SM

Discovered in 1995 by the CDF and D0 collaborations at the Tevatron with proton-antiproton data [18, 19], the top quark plays an important role in studying high energy physics. Its Yukawa interaction is given by

$$\mathcal{L}_{\text{top-Yukawa}} = -\frac{\lambda_t \nu}{\sqrt{2}} \bar{t}_L t_R - \frac{\lambda_t}{\sqrt{2}} H \bar{t}_L t_R + \text{h.c.}, \quad (1.16)$$

yielding a Yukawa coupling of [6]

$$\lambda_t = \frac{\sqrt{2} m_t}{\nu} = 0.991 \pm 0.003. \quad (1.17)$$

172 This Yukawa coupling is very large compared to the other Yukawa couplings in the SM ($\mathcal{O}(10^{-2})$),
 173 leading to the belief that the top quark may have an important role in understanding the
 174 mechanism of electroweak symmetry breaking. On top of this, the very short lifetime of the top
 175 quark makes it an excellent candidate to study the properties of a bare quark. Its high mass,
 176 almost 40 times higher than the mass of the closest fermion in mass, leads to a large coupling
 177 with the Higgs boson and makes the top quark an interesting candidate to investigate how
 178 particles acquire mass.

179 The CKM matrix element V_{tb} , given in [Equation 1.15](#), is experimentally found to be much
 180 larger than V_{ts} , V_{td} , and close to unity. The top quark decays through electroweak interactions
 181 since the W boson mass is smaller than the top quark mass and the W boson can be on shell. A
 182 consequence of this is that the top quark has a very short lifetime of only $1/\Gamma_t \approx 5 \cdot 10^{-25}$ s [6]
 183 leading to the fact that the formation of bound states involving top quarks are not allowed.
 184 This lifetime is even shorter than the typical hadronisation timescale of $1/\Lambda_{\text{QCD}} \approx 10^{-23}$ s,
 185 prohibiting gluons to radiate from the top quark and keeping its spin coherent. Since the
 186 electroweak interactions have a vector-axial vector (V-A) coupling structure³, the top quark
 187 spin orientation can be derived from the angular distributions of its decay products. This makes
 188 it possible to study the polarisation of top quarks from the angular distributions in various
 189 processes.

190 The massiveness of the top quark leads to the fact that a large amount of energy is needed to
 191 create one. This is only the case for high energy collisions such as those happening in the Earth's
 192 upper atmosphere when cosmic rays collide with particles in air, or by particle accelerators.
 193 The production of top quarks happens in two ways: single via the electroweak interaction or in
 194 pairs via the strong interaction. At hadron colliders, the dominant production mechanism is top
 195 quark production via gluon ($gg \rightarrow t\bar{t}$) or quark fusion ($q\bar{q} \rightarrow t\bar{t}$). In [Figure 1.1](#), the different top
 196 quark pair production mechanisms are shown. The production channel of gluon fusion is the
 197 main contributor to the top quark pair cross section at the LHC compared to quark fusion at the
 198 Tevatron. The $gg \rightarrow t\bar{t}$ process contributes 80-90% to the total top quark pair cross section in the
 199 LHC centre-of-mass energy regime of 7-14 TeV [6]. In [Table 1.5](#) the predicted top quark pair
 production cross sections are given for the LHC and the Tevatron.

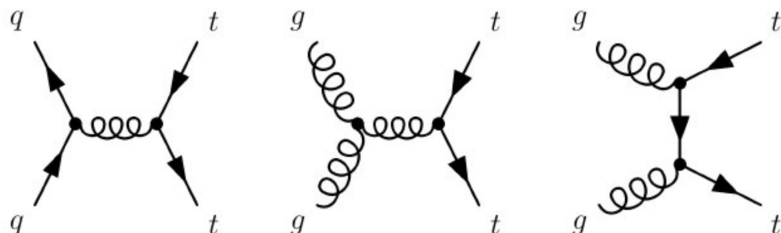


Figure 1.1: Leading order diagrams of the top quark pair production. Gluon fusion (right and middle) are the dominant processes at the LHC, while quark fusion (left) is the dominant one at the Tevatron.

200

³In the SM a vector - axial vector coupling structure $(\gamma^\mu - \gamma^\mu \gamma^5)$ is predicted that only permits left-handed fermions or right-handed anti fermions to interact with a spin-1 particle.

Table 1.5: Predictions on the top quark pair production cross sections at next-to-next-to-leading order with next-to-next-to-leading log soft gluon resummation per centre-of-mass energy [6]. The first uncertainty is from scale dependence, while the second uncertainty originates from parton density functions.

| Experiment | Top quark mass | Centre-of-mass energy | Cross section (pb) |
|------------|-------------------|-----------------------|---|
| Tevatron | $m_t = 173.3$ GeV | $\sqrt{s} = 1.96$ TeV | $\sigma_{tt} = 7.16^{+0.11+0.17}_{-0.20-0.12}$ |
| LHC | $m_t = 173.2$ GeV | $\sqrt{s} = 7$ TeV | $\sigma_{t\bar{t}} = 173.6^{+4.5+8.9}_{-5.9-8.9}$ |
| LHC | $m_t = 173.2$ GeV | $\sqrt{s} = 8$ TeV | $\sigma_{t\bar{t}} = 247.7^{+6.3+11.5}_{-8.5-11.5}$ |
| LHC | $m_t = 173.2$ GeV | $\sqrt{s} = 13$ TeV | $\sigma_{t\bar{t}} = 816.0^{+19.4+34.4}_{-28.6-34.4}$ |

201 The singly produced top quarks are produced via the electroweak interaction. These production
 202 mechanisms are subdivided at leading order into three main channels based on the virtuality
 203 ($Q^2 = -p_\mu p^\mu$) of the exchanged W boson. In Figure 1.2, the corresponding Feynman diagrams
 204 are shown. The single top quark production cross sections, given in Table 1.6, are smaller than
 205 the top quark pair production cross sections since the electroweak coupling strength is smaller
 206 than the strong coupling strength. In addition, for the single top quark production, there is the
 207 need of sea quarks (b, \bar{q}) in the initial states for which the parton density functions increase
 less steeply at low momentum fractions compared to the gluon parton density functions.

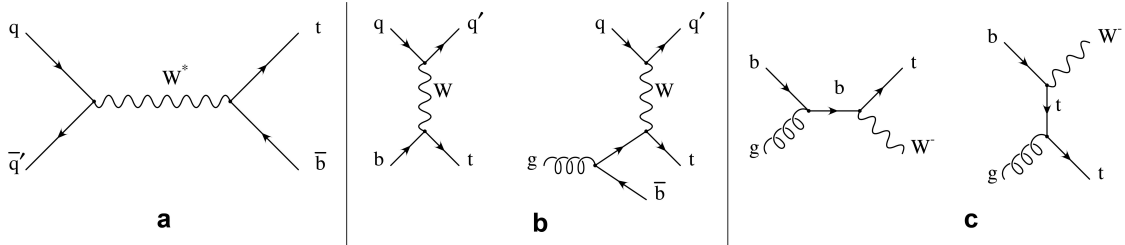


Figure 1.2: Leading order Feynman diagrams of the electroweak production of single top quarks in the s -channel (left), t -channel (middle), and for the tW associated production. Figure taken from [20].

208

209 The production via the t -channel has a virtuality of the W boson $Q^2 > 0$, making it space-like.
 210 It is produced via the scattering of the W boson of a bottom quark coming from a proton
 211 or from gluon splitting ($g \rightarrow b\bar{b}$). It has the highest single top quark cross section in proton
 212 collisions and the top quark production is roughly twice as large than the antitop quark. This is
 213 a consequence of the up-down valence quark composition of the proton. This feature makes
 214 the t -channel sensitive to the parton density functions of the proton. The s -channel is the
 215 production mechanism with the smallest cross section. Here the W boson is time-like ($Q^2 < 0$)
 216 which requires the W boson to have a large virtuality to produce the heavier top quark. It is
 217 produced from two quarks belonging to the same isodoublet (e.g. $u\bar{d}$) and subsequently decays
 218 to $t\bar{b}$. This process get enhanced by many beyond the Standard Model scenarios via the addition
 219 of new heavy particles such as W' . The tW -channel has a top quark produced in association
 220 with a W boson produced on shell $Q^2 = -m_W^2$. This mode is negligible at the Tevatron, but of
 221 relevant size at the LHC. The tW -channel is sensitive to new physics affecting the Wtb vertex.

Table 1.6: Predictions on the single top quark production cross sections at next-to-leading order per centre-of-mass energy [6]. The uncertainties from scale dependence and from parton density functions are combined in quadrature or given separately (scale + PDF). For the t -channel the relative proportions to t and \bar{t} are 65% and 35%. For the s -channel this is respectively 69% and 31%. The tW-channel has an equal proportion of top and antitop quarks. For Tevatron, the top quark mass is assumed to be 173.3 GeV, while the LHC predictions use $m_t = 172.5$ GeV [6, 21].

| Collider | Centre-of-mass energy | Cross section $\sigma_{t+\bar{t}}$ (pb) | | |
|----------|-----------------------|---|-------------------------|-----------------------------------|
| | | t -channel | s -channel | tW-channel |
| Tevatron | $\sqrt{s} = 1.96$ TeV | $2.06^{+0.13}_{-0.13}$ | $1.03^{+0.05}_{-0.05}$ | - |
| LHC | $\sqrt{s} = 7$ TeV | $63.89^{+2.91}_{-2.52}$ | $4.29^{+0.19}_{-0.17}$ | $15.74^{+0.40+1.10}_{-0.40-1.14}$ |
| LHC | $\sqrt{s} = 8$ TeV | $84.69^{+3.76}_{-3.23}$ | $5.24^{+0.22}_{-0.20}$ | $22.37^{+0.60+1.40}_{-0.60-1.40}$ |
| LHC | $\sqrt{s} = 13$ TeV | $216.99^{+9.04}_{-7.71}$ | $10.32^{+0.40}_{-0.36}$ | $71.7^{+1.80+3.40}_{-1.80-3.40}$ |

1.5 Experimental results on the SM top quark

In this section a selection of experimental results of measurements of the SM is presented. In Figure 1.3, a summary plot of the CMS cross section measurements can be found. The estimations by the CMS and ATLAS collaborations of the CKM matrix element V_{tb} from single top quark measurement are given in Figure 1.4. The most precise estimation of V_{tb} originates from a combination of t -channel cross section measurements at 7 and 8 TeV by the CMS collaboration resulting in $|f_L V_{tb}| = 0.998 \pm 0.038$ (exp.) ± 0.016 (theo.). Assuming the $f_L = 1$ and $|V_{tb}| < 1$, this result yields a limit of $|V_{tb}| > 0.92$ at 95% confidence level. The most recent top quark mass measurements are given in Figure 1.5. The CMS combined top quark mass measurement is $m_t = 172.44 \pm 0.48$ GeV from 7 and 8 TeV data.

NOTE:
REWRITE

In general the various measurements show a good agreement with the SM predictions and by lack of deviations from the SM, limits on the anomalous couplings can be derived. The estimated coupling strengths per operator contributing to single top quark production obtained from various measurements at the LHC and Tevatron are shown in Figure 1.6. These results are consistent with the SM expectation for which those operators vanish.

NOTE: Explain Wilson coeff and Wrasaw basis!

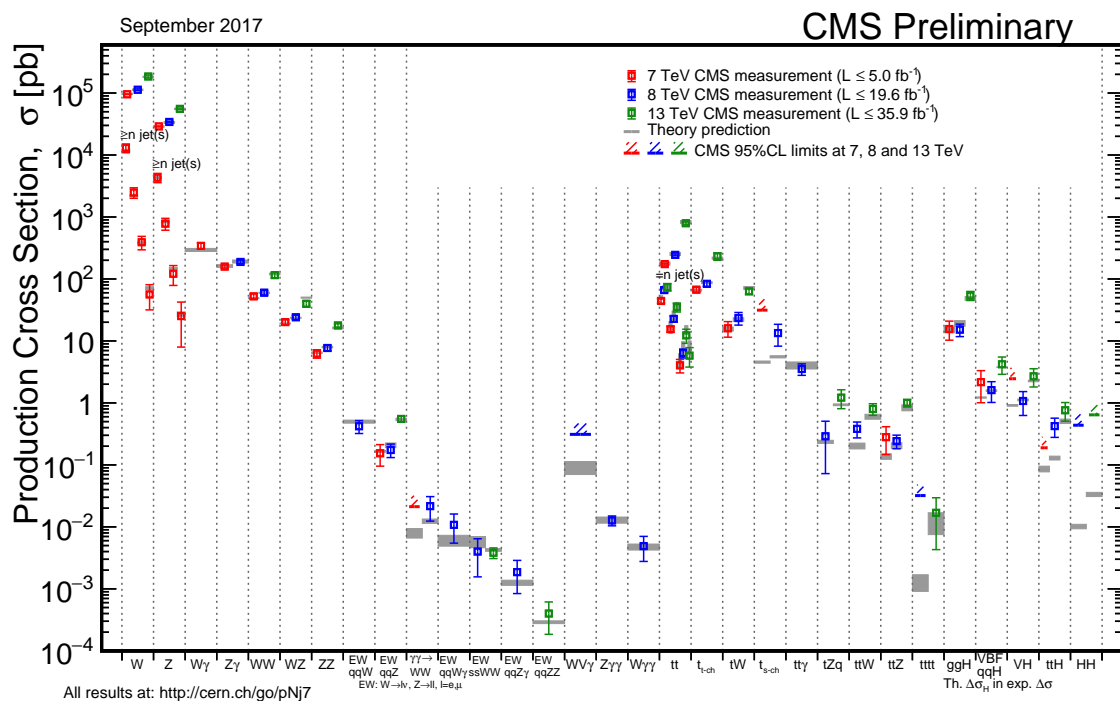


Figure 1.3: Summary of the SM cross section measurements performed by the CMS collaboration. Figure taken from [22]

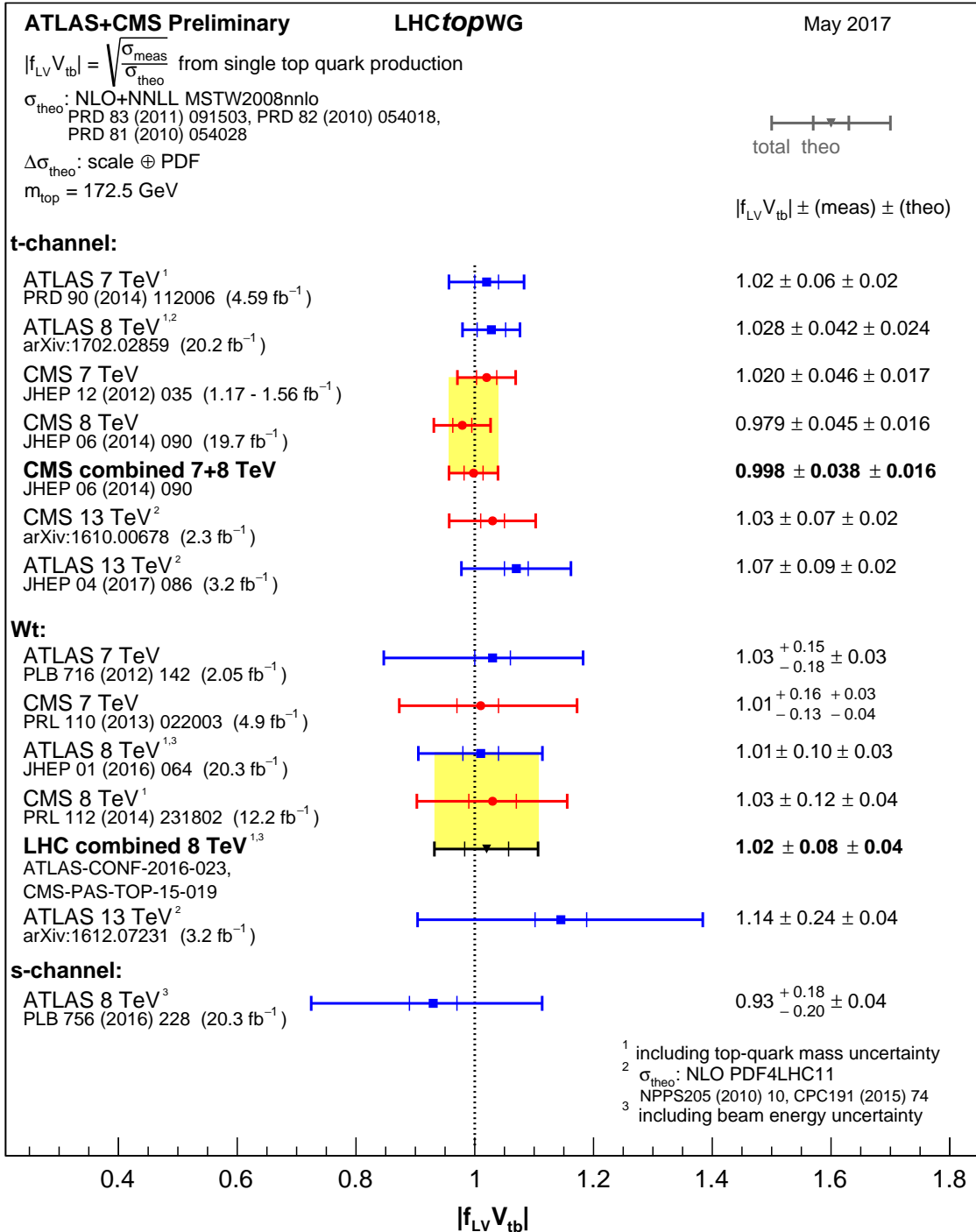


Figure 1.4: Estimations of the SM V_{tb} CKM element from single top cross section measurements. Figure taken from [23].

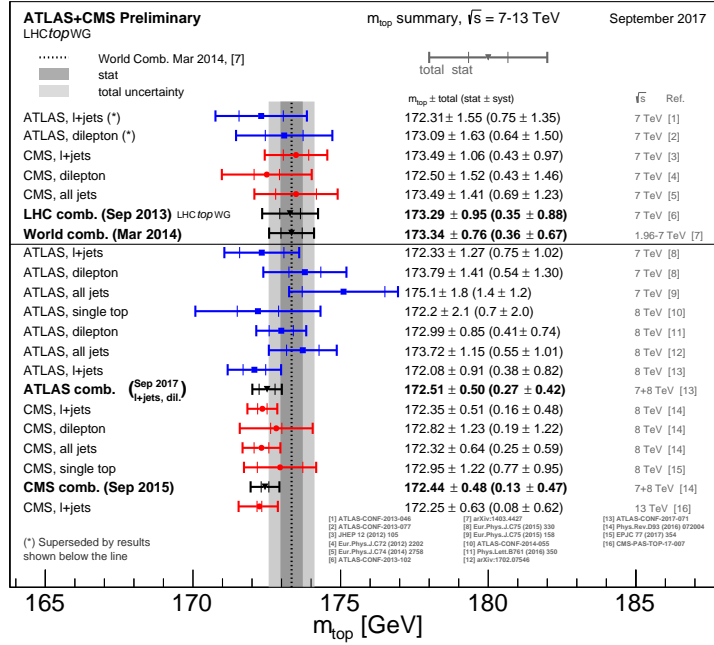


Figure 1.5: Summary of the top mass direct measurements performed by CMS and ATLAS, and compared with the LHC and LHC+Tevatron combinations. The results below the line are produced after the LHC and LHC+Tevatron combinations. Figure taken from [23].

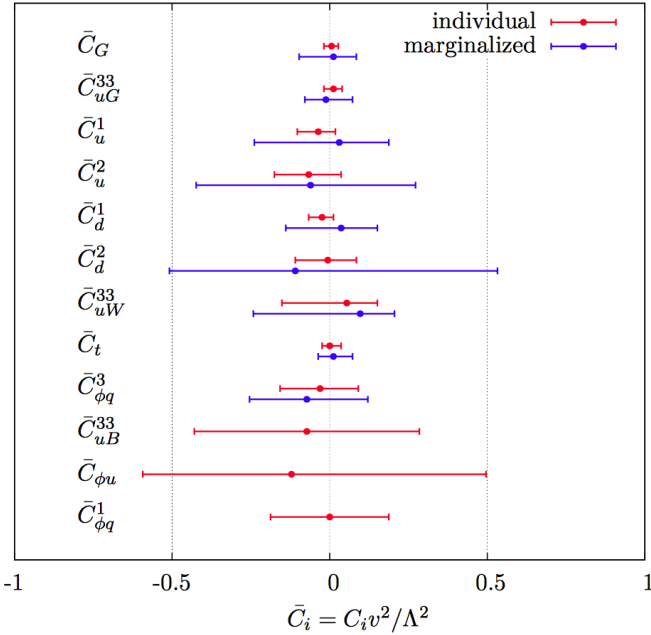


Figure 1.6: Global fit results of top quark effective field theory to experimental data including all constrained operators at dimension six. For the operators, the Warsaw basis of [24] is used. The bounds are set on the Wilson coefficients of various operators contributing to top quark production and decay in two cases (red) all other coefficients set to zero, or (blue) all other coefficient are marginalised over. Figure taken from [25].

237 1.6 Motivation for new physics

238 Many high energy experiments confirm the success of the SM. In particular the scalar boson,
 239 the cornerstone of the SM, has consecrated the theory. Unfortunately there are also strong
 240 indications that the SM ought to be a lower energy expression of a more global theory. The
 241 existence of physics beyond the SM (BSM) [BSMWiley] is strongly motivated. These motivations
 242 are based on direct evidence from observation such as the existence of neutrino masses, the
 243 existence of dark matter and dark energy, or the matter-antimatter asymmetry, and also from
 244 theoretical problems such as the hierarchy problem, the coupling unification or the large numbers
 245 of free parameters in the SM.

246 In the SM, the neutrinos are assumed to be massless, while experiments with solar, atmospheric,
 247 reactor and accelerator neutrinos have established that neutrinos can oscillate and change flavour
 248 during flight [4, 5]. These oscillations are only possible when neutrinos have masses. The
 249 flavour neutrinos (ν_e , ν_μ , ν_τ) are then linear expressions of the fields of at least three mass
 250 eigenstate neutrinos ν_1 , ν_2 , and ν_3 .

251 The ordinary or baryonic matter described by the SM describes only 5% of the mass (energy)
 252 content of the universe. Astrophysical evidence indicated that dark matter is contributing
 253 to approximately 27%, and dark energy to 68% of the content of the universe. From the
 254 measurements of the temperature and polarizations anisotropies of the cosmic microwave
 255 background by the Planck experiment [26], the density of cold non baryonic matter is determined.
 256 Cold dark matter is assumed to be only sensitive to the weak and gravitational force, leading
 257 to only one possible SM candidate: the neutrino. However, these are too light to account for
 258 the vast amount of dark matter and other models are needed. Dark energy is assumed to be
 259 responsible for the acceleration in the expansion of the universe [27].

260 At the Big Bang matter and antimatter are assumed to be produced in equal quantities.
 261 However, it is clear that we are surrounded by matter. So where did all the antimatter go?
 262 In 1967, Sakharov identified three mechanisms that are necessary to obtain a global matter
 263 antimatter asymmetry [28]. These mechanisms are those of baryon and lepton number violation,
 264 that at a given moment in time there was a thermal imbalance for the interactions in the universe,
 265 and there is charge C and charge parity CP violation⁴.

266 The large number of free parameters in the SM comes from the nine fermion masses, three
 267 CKM mixing angles and one CP violating phase, one EM coupling constant g' , one weak coupling
 268 constant g , one strong coupling constant g_s , one QCD vacuum angle, one vacuum expectation
 269 value, and one mass of the scalar boson. This large number of free parameters leads to the
 270 expectation of a more elegant and profound theory beyond the SM.

271 The hierarchy problem [29] is related to the huge difference in energy between the weak
 272 scale and the Planck scale. The vev of the Brout-Englert-Higgs field determines the weak scale
 273 that is approximately 246 GeV. The radiative corrections to the scalar boson squared mass m_H^2 ,
 274 coming from its self couplings and couplings to fermions and gauge bosons, are quadratically

⁴The rate of a process $i \rightarrow f$ can be different from the CP-conjugate process: $\tilde{i} \rightarrow \tilde{f}$. The SM includes sources of CP-violation through the residual phase of the CKM matrix. However, these could not account for the magnitude of the asymmetry observed.

proportional to the ultraviolet momentum cut-off Λ_{UV} . This cut-off is at least equal to the energy to which the SM is valid without the need of new physics. For the SM to be valid up to the Planck mass, the correction to m_H^2 becomes thirty orders of magnitude larger than m_H^2 . This implies that an extraordinary cancellation of terms should happen. This is also known as the naturalness problem of the H boson mass.

The correction to the squared mass of the scalar boson coming from a fermion f , coupling to the scalar field ϕ with a coupling λ_f is given by

$$\Delta m_H^2 = -\frac{|\lambda_f|^2}{8\pi^2} \Lambda_{\text{UV}}^2, \quad (1.18)$$

while the correction to the mass from a scalar particle S with a mass m_S , coupling to the scalar field with a Lagrangian term $-\lambda_S |\phi|^2 |S|^2$ is

$$\Delta m_H^2 = \frac{|\lambda_S|^2}{16\pi^2} \left(\Lambda_{\text{UV}}^2 - 2m_S^2 \ln \left(\frac{\Lambda_{\text{UV}}}{m_S} \right) + \dots \right). \quad (1.19)$$

As one can see the correction term to m_H^2 is much larger than m_H^2 itself. By introducing BSM physics models that introduce new scalar particles at the TeV scale that couple to the scalar boson one can cancel the Λ_{UV}^2 divergence and avoid this fine-tuning.

The choice of the $SU(3)_C \times SU(2)_L \times U(1)_Y$ symmetry group itself as well as the separate treatment of the three forces included in the SM raises concern. The intensity of the forces show a large disparity around the electroweak scale, but have comparable strengths at higher energies. The electromagnetic and weak forces are unified in a electroweak interaction, but the strong coupling constant does not encounter the other coupling constants at high energies. In order to reach a grand unification, the running of couplings can be modified by the addition of new particles in BSM models.

1.7 An effective approach beyond the SM: FCNC involving a top quark

The closeness of the top quark mass to the electroweak scale led physicist to believe that it is a sensitive probe for new physics. Studying its properties is therefore an important topic of the experimental program at the LHC. Several extensions of the SM enhance the FCNC branching ratios and can be probed at the LHC [17], from which some of them are shown in Table 1.7. Previous searches have been performed at the Tevatron by the CDF [30] and D0 [31] collaborations, and at the LHC by the ATLAS [32–36] and CMS [37–41] collaborations.

The impact of BSM models can be written in a model independent way by means of an effective field theory valid up to an energy scale Λ . The leading effects are parametrized by a set of fully gauge symmetric dimension-6 operators that are added to the SM Lagrangian and can be reduced to a minimal set of operators as discussed in [42, 43]. The full Lagrangian, neglecting neutrino physics, in the fully gauge symmetric case is given by

$$\mathcal{L}_{\text{SM+EFT}} = \mathcal{L}_{\text{SM}} + \sum_i \frac{\tilde{c}_i}{\Lambda^2} \mathcal{O}_i + \mathcal{O}\left(\frac{1}{\Lambda^3}\right), \quad (1.20)$$

Table 1.7: The predicted branching ratios \mathcal{B} for FCNC interactions involving the top quark in some BSM models [17]: quark singlet (QS), generic two Higgs doublet model (2HDM) and the minimal supersymmetric extensions to the SM (MSSM);

| Process | QS | 2HDM | MSSM | Process | QS | 2HDM | MSSM |
|-------------------------|--------------------------|--------------------------|------------------------|-------------------------|--------------------------|----------------|------------------------|
| $t \rightarrow uZ$ | $\leq 1.1 \cdot 10^{-4}$ | — | $\leq 2 \cdot 10^{-6}$ | $t \rightarrow cZ$ | $\leq 1.1 \cdot 10^{-4}$ | $\leq 10^{-7}$ | $\leq 2 \cdot 10^{-6}$ |
| $t \rightarrow u\gamma$ | $\leq 7.5 \cdot 10^{-9}$ | — | $\leq 2 \cdot 10^{-6}$ | $t \rightarrow c\gamma$ | $\leq 7.5 \cdot 10^{-9}$ | $\leq 10^{-6}$ | $\leq 2 \cdot 10^{-6}$ |
| $t \rightarrow ug$ | $\leq 1.5 \cdot 10^{-7}$ | — | $\leq 8 \cdot 10^{-5}$ | $t \rightarrow cg$ | $\leq 1.5 \cdot 10^{-7}$ | $\leq 10^{-4}$ | $\leq 8 \cdot 10^{-5}$ |
| $t \rightarrow uH$ | $\leq 4.1 \cdot 10^{-5}$ | $\leq 5.5 \cdot 10^{-6}$ | $\leq 10^{-5}$ | $t \rightarrow cH$ | $\leq 4.1 \cdot 10^{-5}$ | $\leq 10^{-3}$ | $\leq 10^{-5}$ |

where the Wilson coefficients \bar{c}_i depend on the considered theory and on the way that new physics couples to the SM particles. Considering that Λ is large, contributions suppressed by powers of Λ greater than two are neglected. Moreover, all four fermion operators are omitted for the rest of this thesis. After electroweak symmetry breaking the operators induce [17, 44] both corrections to the SM couplings and new interactions at tree level such as FCNC interactions. The FCNC interactions of the top quark that are not present in the SM are given by

$$\mathcal{L}_{\text{EFT}}^t = \frac{\sqrt{2}}{2} \sum_{q=u,c} \left[g' \frac{\kappa_{t\gamma q}}{\Lambda} A_{\mu\nu} \bar{t} \sigma^{\mu\nu} (f_{\gamma q}^L P_L + f_{\gamma q}^R P_R) q \right. \quad (1.21)$$

$$+ \frac{g}{2\cos\theta_W} \frac{\kappa_{tZq}}{\Lambda} Z_{\mu\nu} \bar{t} \sigma^{\mu\nu} (f_{Zq}^L P_L + f_{Zq}^R P_R) q \quad (1.22)$$

$$+ \frac{\sqrt{2}g}{4\cos\theta_W} \zeta_{tZq} \bar{t} \gamma^\mu (\tilde{f}_q^L P_L + \tilde{f}_q^R P_R) q Z_\mu \quad (1.23)$$

$$+ g_s \frac{\kappa_{tgq}}{\Lambda} Z_{\mu\nu} \bar{t} \sigma^{\mu\nu} (f_{gq}^L P_L + f_{gq}^R P_R) q G_{\mu\nu}^a \quad (1.24)$$

$$+ \eta_{Hqt} \bar{t} (\hat{f}_q^L P_L + \hat{f}_q^R P_R) q H + \text{h.c.} \Big], \quad (1.25)$$

NOTE: At something about Warsaw basis

where the value of the FCNC couplings at scale Λ are represented by $\kappa_{tZq}, \kappa_{tgq}, \kappa_{t\gamma q}, \zeta_{tZq}$, and η_{Hqt} . These are assumed to be real and positive, with the unit of GeV^{-1} for κ_{txq}/Λ and no unit for ζ_{xqt} and η_{xqt} . In the equation $\sigma^{\mu\nu}$ equals to $\frac{i}{2} [\gamma^\mu, \gamma^\nu]$, and the left- and right-handed chirality projector operators are denoted by P_L and P_R . The electromagnetic coupling constant is denoted by g' , the strong interaction coupling is denoted as g_s , while the electroweak interaction is parametrised by the coupling constant g and the electroweak mixing angle θ_W . The complex chiral parameters are normalized according to $|f_{xq}^L|^2 + |f_{xq}^R|^2 = 1$, $|\tilde{f}_q^L|^2 + |\tilde{f}_q^R|^2 = 1$, and $|\hat{f}_q^L|^2 + |\hat{f}_q^R|^2 = 1$. In the expression for $\mathcal{L}_{\text{EFT}}^t$, the unitary gauge is adopted and the scalar field is expanded around its vacuum expectation value with H being the SM scalar boson, and the field strength tensors of the photon A_μ , the gluon field $G_\mu^{1\dots 8}$, and the Z boson Z_μ^0 are defined as

$$A_{\mu\nu} = \partial_\mu A_\nu - \partial_\nu A_\mu, Z_{\mu\nu} = \partial_\mu Z_\nu - \partial_\nu Z_\mu, \text{ and } G_{\mu\nu} = \partial_\mu G_\nu^a - \partial_\nu G_\mu^a + g_s f_{bc}^a G_\mu^b G_\nu^c. \quad (1.26)$$

303 Denoting the structure constant of the $SU(3)_C$ group as f_{bc}^a . Note that there are two coupling
 304 constants arising in $\mathcal{L}_{\text{EFT}}^t$, which is a residue of electroweak symmetry breaking. The massive Z
 305 boson will appear in both the Z_μ^0 field as well as the covariant derivative, leading to an extra
 306 Z-vertex.

307 **1.8 Experimental constraints on top-FCNC**

Experiments commonly put limits on the branching ratios which allow an easier interpretation across different EFT models by use of the branching ratio

$$\mathcal{B}(t \rightarrow qX) = \frac{\delta_{txq}^2 \Gamma_{t \rightarrow qX}}{\Gamma_t}, \quad (1.27)$$

308 where $\Gamma_{t \rightarrow qX}$ represents the FCNC decay width⁵ for a coupling strength $\delta_{txq}^2 = 1$, and Γ_t the full
309 decay width of the top quark. In the SM, supposing a top quark mass of 172.5 GeV, the full
310 width becomes $\Gamma_t^{\text{SM}} = 1.32$ GeV [45].

311 Searches for top-FCNC usually adopt a search strategy depending on the experimental set-up
312 and the FCNC interaction of interest, looking either for FCNC interactions in the production of a
313 single top quark or in its decay for top quark pair interactions. In Figure 1.7, these two cases
314 are shown for the tZq vertex.



Figure 1.7: Feynman diagrams for the processes with a tZq FCNC interaction, where the FCNC interaction is indicated with the shaded dot. (a) Single top quark production through an FCNC interaction. (b) Top quark pair production with an FCNC induced decay.

315

316 The observation of top-FCNC interactions has yet to come and experiments have so far only
317 been able to put upper bounds on the branching ratios. An overview of the best current limits
318 is given in Table 1.8. In Figure 1.8 a comparison is shown between the current best limits set
319 by ATLAS and CMS with respect to several BSM model benchmark predictions. From there
320 one can see that FCNC searches involving a Z or H boson are close to excluding or confirming
321 several BSM theories. In Figure 1.9, the searches performed by CMS are summarised. For the
322 tZq vertex, the best limit from CMS comes from Ref. [37] where both single top quark and
323 top quark pair is studied. The observed (expected) limits 95% CL at 8 TeV for the FCNC tZq
324 interaction by CMS are $\mathcal{B}(t \rightarrow uZ) < 2.2 \cdot 10^{-4}$ ($2.7 \cdot 10^{-4}$) and $\mathcal{B}(t \rightarrow cZ) < 4.9 \cdot 10^{-4}$ ($12 \cdot 10^{-4}$).
325

⁵The decay width of a certain process represents the probability per unit time that a particle will decay. The total decay width, defined as the sum of all possible decay widths of a particle, is inversely proportional to its lifetime.

Table 1.8: Overview of the most stringent observed and expected experimental limits on top-FCNC branching ratios \mathcal{B} at 95% confidence level.

| Process | Search mode | Observed \mathcal{B} | Expected \mathcal{B} | Experiment | |
|-------------------------|-----------------------------|------------------------|------------------------|------------|------|
| $t \rightarrow uZ$ | top quark pair decay | 1.7×10^{-4} | 2.4×10^{-4} | ATLAS | [36] |
| $t \rightarrow u\gamma$ | single top quark production | 1.3×10^{-4} | 1.9×10^{-4} | CMS | [39] |
| $t \rightarrow ug$ | single top quark production | 4.0×10^{-5} | 3.5×10^{-5} | ATLAS | [33] |
| $t \rightarrow uH$ | top quark pair decay | 2.4×10^{-3} | 1.7×10^{-3} | ATLAS | [35] |
| $t \rightarrow cZ$ | top quark pair decay | 2.3×10^{-4} | 3.2×10^{-4} | ATLAS | [36] |
| $t \rightarrow c\gamma$ | single top quark production | 2.0×10^{-3} | 1.7×10^{-3} | CMS | [39] |
| $t \rightarrow cg$ | single top quark production | 2.0×10^{-4} | 1.8×10^{-4} | ATLAS | [33] |
| $t \rightarrow cH$ | top quark pair decay | 2.2×10^{-3} | 1.6×10^{-3} | CMS | [35] |

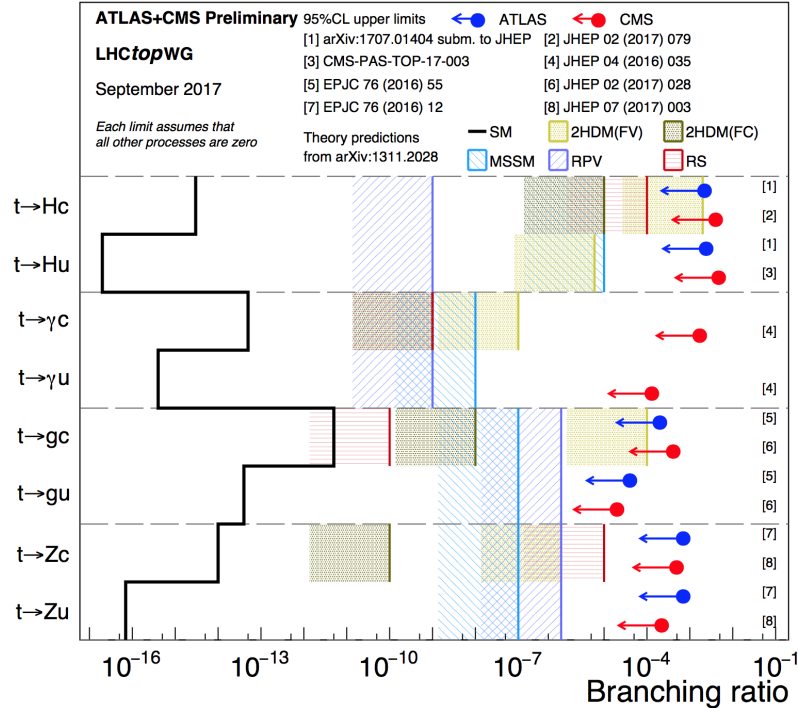
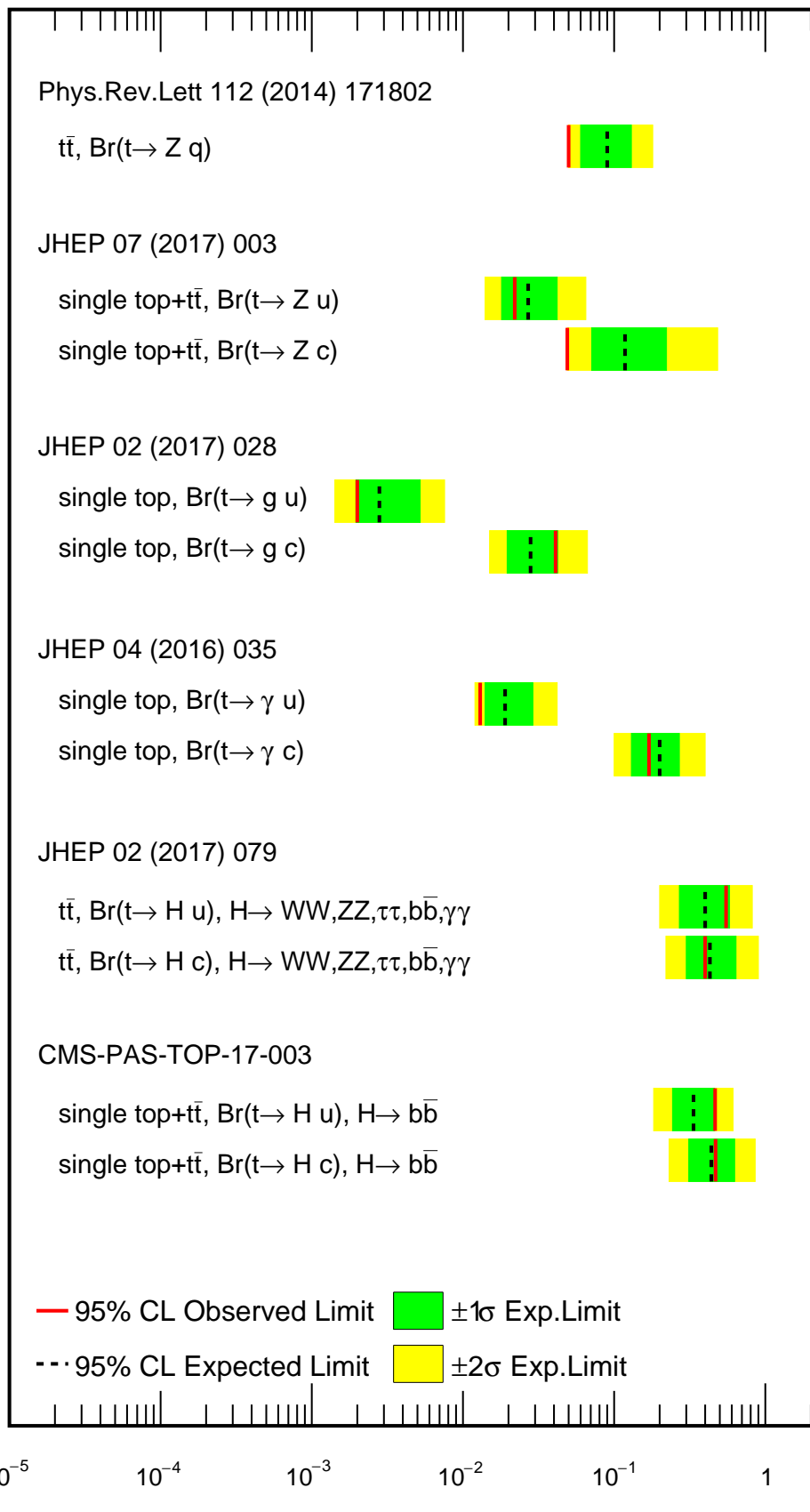


Figure 1.8: Current best limits set by CMS and ATLAS for top-FCNC interactions. Figure taken from [22]. Remake with new atlas results

CMS preliminary

September 2017



Experimental set-up

2

327 The main objective of the Large Hadron Collider (LHC) was the search for the Brout-Englert-
 328 Higgs boson. The Large Electron Positron (LEP) [46] and Tevatron [47] experiments had
 329 established that the mass of the scalar boson has to be larger than 114 GeV [48, 49], and smaller
 330 than approximate 1 TeV due to unitarity and perturbativity constraints [50]. On top of this,
 331 the search for new physics such as supersymmetry or the understanding of dark matter were
 332 part of the motivation for building the LHC. Since the start of its operation, the LHC is pushing
 333 the boundaries of the Standard Model, putting the most stringent limits on physics beyond the
 334 Standard Model as well as precision measurements of the parameters of the Standard Model. A
 335 milestone of the LHC is the discovery the scalar boson in 2012 by the two largest experiments
 336 at the LHC [10, 11].

337 This chapter is dedicated to the experimental set up of the LHC and the Compact Muon
 338 Solenoid (CMS) experiment. Section 2.1 describes the LHC and its acceleration process for
 339 protons to reach their design energies. The CMS experiment and its components are presented
 340 in Section 2.2. The upgrades performed during the long shutdown in 2013 are discussed
 341 in Section 2.2.4. The data acquistion of CMS is presented in Section 2.2.3, while the CMS
 342 computing model is shown in Section 2.2.5.

343 2.1 The Large Hadron Collider

344 The LHC has started its era of cutting edge science on 10 September 2008 [51] after approval by
 345 the European Organisation of Nuclear Research (CERN) in 1995 [52]. Installed in the previous
 346 LEP tunnels, the LHC consists of a 26.7 km ring, that is installed between 45 and 170 m under
 347 the French-Swiss border amidst Cessy (France) and Meyrin (Switzerland). Built to study rare
 348 physics phenomena at high energies, the LHC can accelerate two type of particles, protons or
 349 ions Pb^{45+} , and provides collisions at four interaction points, where the particle bunches are
 350 crossing. Experiments for studying the collisions are installed on each interaction point.

351 As can be seen in Figure 2.1, the LHC is last element in a chain that creates, injects and
 352 accelerates protons. The starting point is the ionisation of hydrogen, creating protons that are
 353 injected in a linear accelerator (LINAC 2). Here, the protons obtain an energy of 50 MeV. They
 354 continue to the proton synchrotron booster (PSB or Booster), where the packs of protons are

355 accelerated to 1.4 GeV and each pack is split up in twelve bunches with 25 ns spacing for Run 2
 356 (50 ns for Run 1). The proton synchrotron (PS) then increases their energy to 25 GeV before the
 357 super proton synchrotron (SPS) increases the proton energy up to 450 GeV. Each accelerator
 358 ring expands in radius in order to reduce the energy loss of the protons by synchrotron radiation¹
 359 Furthermore, the magnets responsible for the bending of the proton trajectories have to be
 360 strong enough to sustain to higher proton energy. Ultimately, the protons are injected into
 361 opposite directions into the LHC, where they are accelerated to 3.5 TeV (in 2010 and 2011),
 362 4 TeV (in 2012 and 2013) or 6.5 TeV (in 2015 and 2016) [53]. Before the start of the LHC
 363 in 2010, the previous energy record was held by the Tevatron collider at Fermilab, colliding
 364 proton with antiprotons at $\sqrt{s} = 1.96$ TeV. When completely filled, the LHC nominally contains
 2220 bunches in Run 2, compared to 1380 in Run 1 (design: 2200).

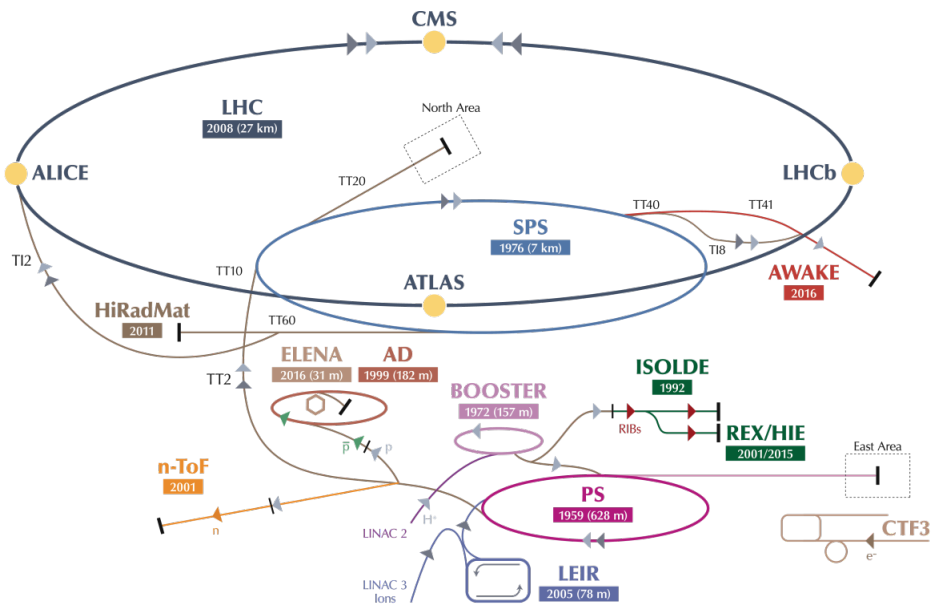


Figure 2.1: Schematic representation of the accelerator complex at CERN [54]. The LHC (dark blue) is the last element in chain of accelerators. Protons are successively accelerated by LINAC 2, the Booster, the Proton Synchrotron (PS) and the Super Proton Synchrotron (SPS) before entering the LHC.

365 Inside the LHC ring [55], the protons are accelerated by the means of radio frequency cavities,
366 while 1232 dipole magnets of approximately 15 m long, each weighing 35 t ensure the deflection
367 of the beams. The two proton beams circulate in opposite direction in separate pipes inside
368 of the magnet. Through the use of a strong electric current in the coils around the beam pipe,
369 magnetic fields are generated and cause the protons to bend in the required orbits. In order to
370 get the coil to become superconducting and able to produce - with the aid of an iron return yoke
371 - a strong magnetic field of 8.3 T, the magnet structure is surrounded by a vessel. This vessel is
372 filled with liquid Helium making it possible to cool down the magnet to 1.9 K. In order to get

¹This energy loss is proportional to the fourth power of the proton energy and inversely proportional to the bending radius.

374 more focussed and stabilised proton beams, additional higher-order multipole and corrector
 375 magnets are placed along the LHC beam line.

376 The LHC is home to seven experiments, each located on an interaction point:

- 377 • A Toroidal LHC ApparatuS (ATLAS) [56] and the Compact Muon Solenoid (CMS) [57]
 378 experiments are the two general purpose detectors at the LHC. They both have a hermetic,
 379 cylindrical structure and were designed to search for new physics phenomena along with
 380 precision measurements of the Standard Model. The existence of two distinct experiments
 381 allows cross-confirmation of any discovery.
- 382 • A Large Ion Collider Experiment (ALICE) [58] and the LHC Beauty (LHCb) [59] exper-
 383 iments are focusing on specific phenomena. ALICE studies strongly interacting matter
 384 at extreme energy densities where a quark-gluon plasma forms in heavy ion collisions
 385 (Pb-Pb or p-Pb). LHCb searches for differences between matter and antimatter with the
 386 focus on b physics..
- 387 • The forward LHC (LHCf) [60] and the TOTal cross section, Elastic scattering and diffraction
 388 dissociation Measurement (TOTEM) [61] experiments are two smaller experiments that
 389 focus on head on collisions. LHCf consists of two parts placed before and after ATLAS
 390 and studies particles created at very small angles. TOTEM is placed in the same cavern as
 391 CMS and measures the total proton-proton cross section and studies elastic and diffractive
 392 scattering.
- 393 • The Monopoles and Exotics Detector At the LHC (MoEDAL) [62] experiment is situated
 394 near LHCb and tries to find magnetic monopoles.

For the enhancement of the exploration of rare events and thus enhancing the number of collisions, high beam energies as well as high beam intensities are required. The luminosity [63] is a measurement of the number of collisions that can be produced in a detector per square meter and per second and is the key role player in this enhancement. The LHC collisions create a number of events per second given by

$$N_{\text{event}} = L \sigma_{\text{event}}, \quad (2.1)$$

where σ_{event} is the cross section of the event of interest and L the machine luminosity. This luminosity depends only on the beam parameters and is for a Gaussian beam expressed as

$$L = \frac{1}{4\pi} N_b n_b f_{\text{rev}} \frac{N_b}{\epsilon_n} \left(1 + \left(\frac{\theta_c \sigma_z}{2\sigma^*} \right)^2 \right)^{-\frac{1}{2}} \frac{\gamma_r}{\beta^*}. \quad (2.2)$$

395 The number of particles per bunch is expressed by N_b , while n_b is the number of bunches
 396 per beam, f_{rev} the revolution frequency, γ_r the relativistic gamma factor, ϵ_n the normalized
 397 transverse beam emittance - a quality for the confinement of the beam , β^* the beta function at
 398 the collision point - a measurement for the width of the beam, θ_c the angle between two beams
 399 at the interaction point, σ_z the mean length of one bunch, and σ^* the mean height of one bunch.

400 In Equation 2.2, the blue part represents the stream of particles, the red part the brilliance, and
 401 the green part the geometric reduction factor due to the crossing angle at the interaction point.

402 The peak design luminosity for the LHC reached in 2016 is $10^{34} \text{ m}^{-2}\text{s}^{-1}$, which leads to about
 403 1 billion proton interactions per second. In 2016, the LHC was around 10% above this design
 404 luminosity [64]. The luminosity is not a constant in time since it diminishes due to collisions
 405 between the beams, and the interaction of the protons and the particle gas that is trapped in
 406 the centre of the vacuum tubes due to the magnetic field. The diffusion of the beam degrades
 407 the emittance and therefore also the luminosity. For this reason, the mean lifetime of a beam
 408 inside the LHC is around 15 h. The integrated luminosity - the luminosity provided in a certain
 409 time range - recorded by CMS and ATLAS over the year 2016 is given in Figure 2.2. In Run 2,
 the peak luminosity is $13\text{-}17 \cdot 10^{33} \text{ cm}^{-2}\text{s}^{-1}$ compared to $7.7 \cdot 10^{33} \text{ cm}^{-2}\text{s}^{-1}$ in Run 1.

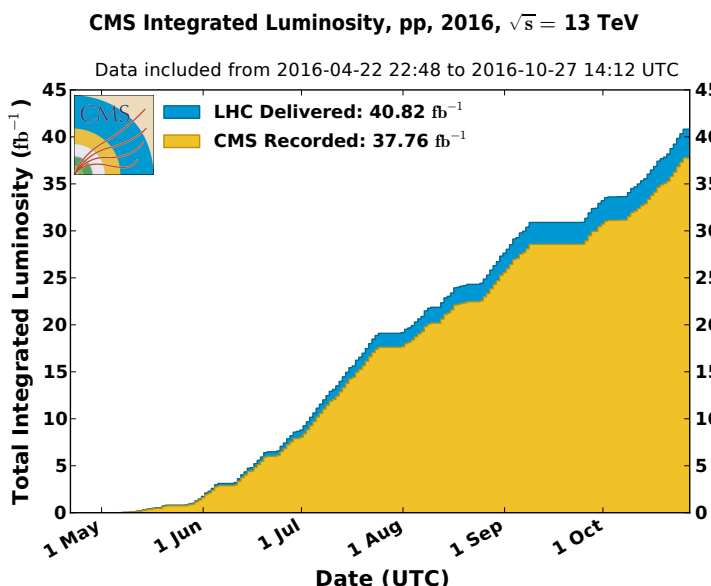


Figure 2.2: Cumulative offline luminosity measured versus day delivered to (blue), and recorded by CMS (orange) during stable beams and for proton collisions at 13 TeV centre-of-mass energy in 2016. The delivered luminosity accounts for the luminosity delivered from the start of stable beams until the LHC requests CMS to turn off the sensitive detectors to allow a beam dump or beam studies [65].

410

411 Multiple proton-proton interactions can occur during one bunch crossing, referred to as
 412 pileup. On average, the number of pileup events is proportional to the luminosity times the total
 413 inelastic proton-proton cross section. In 2016, an average of about 27 of pileup interactions
 414 has been observed in 13 TeV proton collisions at the interaction point of CMS. For 2012, this
 415 number was about 21 pileup interactions for 8 TeV collisions.

416 2.2 The Compact Muon Solenoid

417 At one of the collision points of the LHC, the CMS detector[66–68] is placed. Weighing 14 000 t,
 418 this cylindrical detector is about 28.7 m long and 15 m in diameter. It has an onion like structure

of several specialised detectors and contains a superconducting solenoid with a magnetic field of 3.8 T. Living in a hadronic environment, multi-jet processes produced by the strong interaction are a main source of background for rare physics processes. Therefore, good identification, momentum resolution, and charge determination of muons, electrons and photons are one of the main goals of the CMS detector. Additionally, a good charged particle momentum resolution and reconstruction efficiency in the inner tracker provides identification for jets coming from b quarks or tau particles can be identified. Also the electromagnetic resolution for an efficient photon and lepton isolation as well as a good hadronic calorimeter for the missing transverse energy² were kept into account while designing CMS. In Figure 2.3, an overview of the CMS detector is shown.

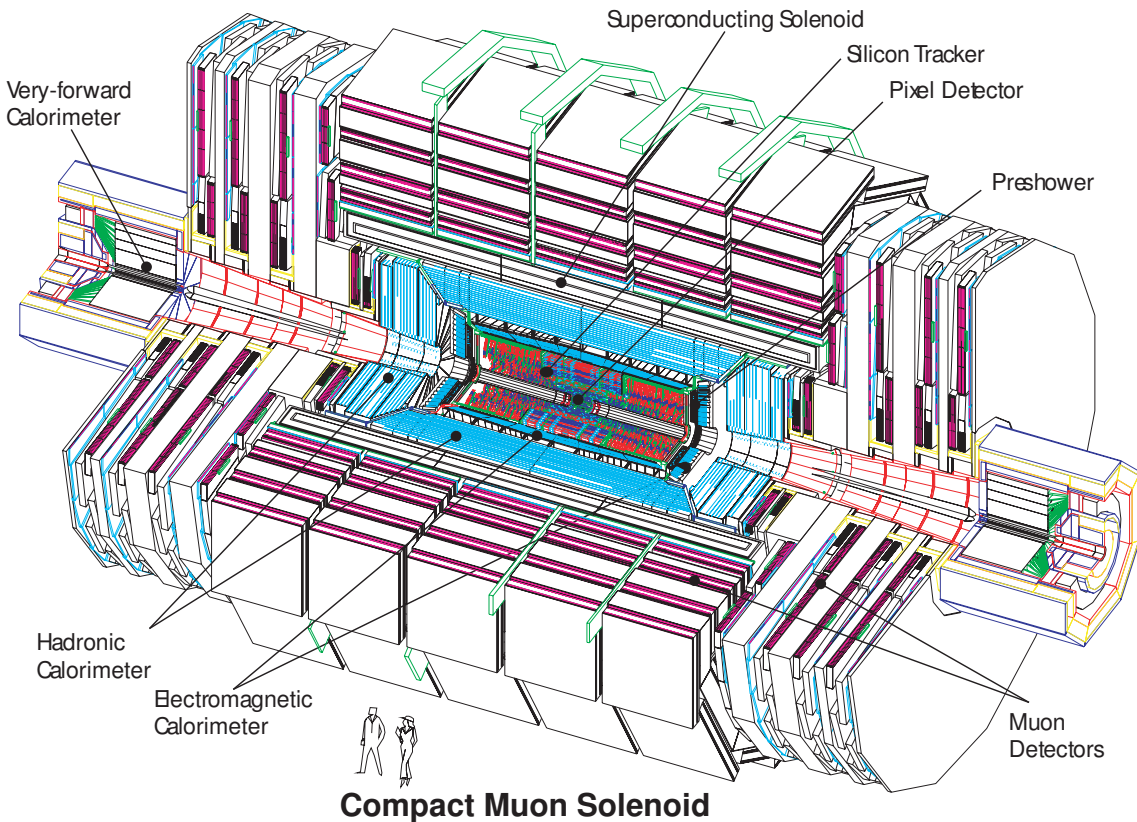


Figure 2.3: Mechanical layout of the CMS detector. Figure taken from [69].

428

429 2.2.1 CMS coordinate system

The coordinate system used by CMS can be found in Figure 2.4. The origin of the right handed orthogonal coordinate system is chosen to be the point of collisions. The x-axis points towards the centre of the LHC ring such that the y-axis points towards the sky, and the z-axis lies tangent to the beam axis. Since the experiment has a cylindrical shape, customary coordinates are used

²The missing transverse energy comes from an imbalance in the transverse plane. This will be discussed in Chapter 4.

to describe the momentum \vec{p} : the distance $p = |\vec{p}|$, the azimuthal angle³ $\phi \in [-\pi, \pi]$, the pseudo-rapidity⁴ η :

$$\eta = -\ln\left(\tan\left(\frac{\theta}{2}\right)\right). \quad (2.3)$$

For the energies considered at the LHC, where $E \gg m$, the pseudo-rapidity is a good approximation of the rapidity y

$$y = \frac{1}{2} \ln\left(\frac{E + p_z}{E - p_z}\right), \quad (2.4)$$

- 430 where the difference of rapidities of two particles is invariant under a Lorentz boost in the z-direction.

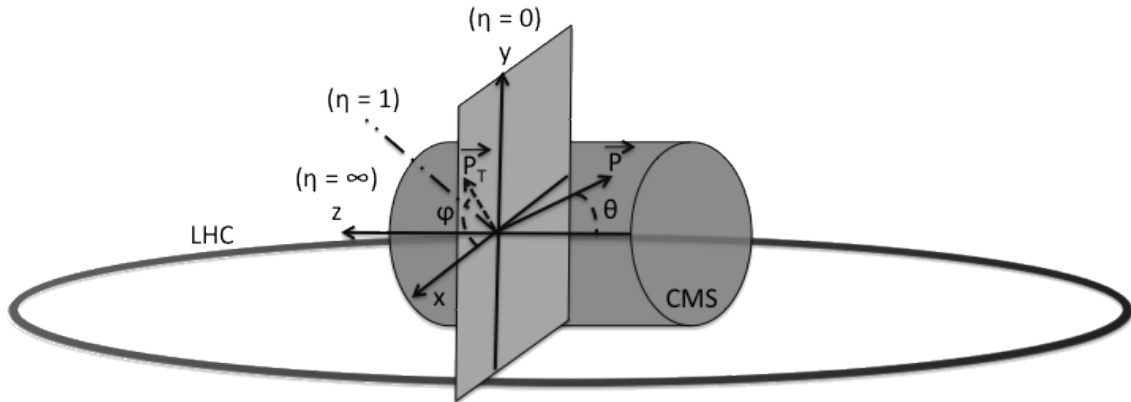


Figure 2.4: Representation of the coordinate system used by CMS. The point of origin is put at the collision point. The x-axis points towards the centre of the LHC ring such that the z-axis lies tangent to the beam axis.

- 431

432 2.2.2 Towards the heart of CMS

- 433 The CMS detector can be divided into two parts. A central barrel is placed around the beam
 434 pipe ($|\eta| < 1.4$), and two plugs (end caps) ensure the hermeticity of the detector. In [Figure 2.3](#)
 435 and [Figure 2.5](#) the onion like structure of the CMS detector is visible. The choice of a solenoid of
 436 12.9 m long and 5.9 m diameter gives the advantage of bending the particle trajectories in the
 437 transverse plane. The hadronic calorimeter ([Section 2.2.2.3](#)), the electromagnetic calorimeter
 438 ([Section 2.2.2.4](#)) and the tracker ([Section 2.2.2.5](#)) are within the solenoid ([Section 2.2.2.2](#)),
 439 while the muon chambers ([Section 2.2.2.1](#)) are placed outside the solenoid. The data used for
 440 the search presented in this thesis is collected after the long shutdown 1. After discussing each
 441 part of CMS in their Run 1 configuration, [Section 2.2.4](#) elaborates on their different upgrades
 442 for the data collected in Run 2.

³The azimuthal angle is the angle between the x-axis and the projection in the transverse plane of the momentum \vec{p} , denoted as \vec{p}_T .

⁴The pseudo rapidity is expressed by the polar angle θ between the direction of \vec{p} and the beam.

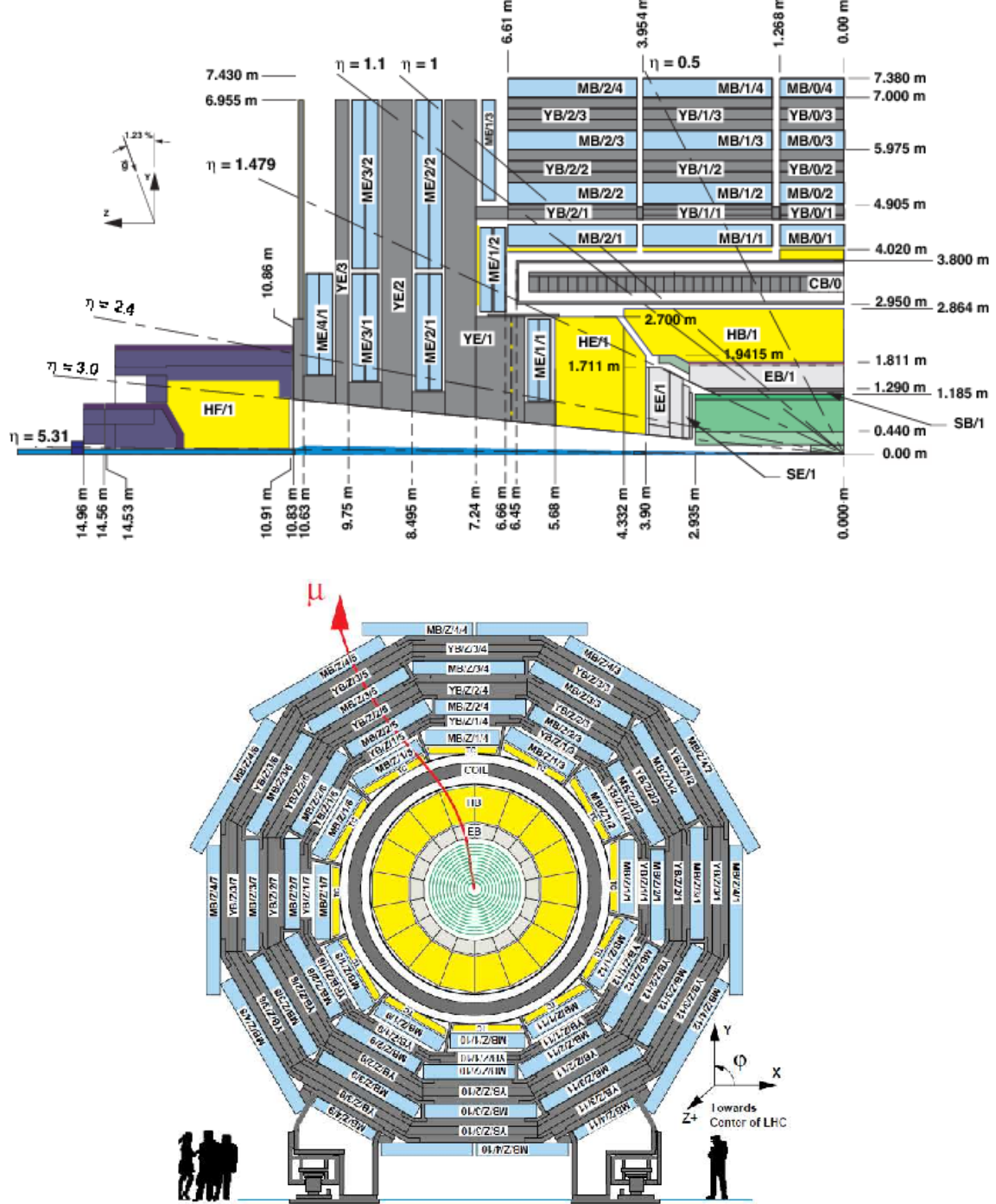


Figure 2.5: Schematic view of the CMS detector in the Run 1 configuration. The longitudinal view of one quarter of the detector is given on top, while the transversal view is shown on the bottom. The muon system barrel elements are denoted as $MBZ/N/S$, where $z = -2 \dots +2$ is the barrel wheel number, $n = 1 \dots 4$ the station number and $S = 1 \dots 12$ the sector number. Similarly, the steel return yokes are denoted as $YBZ/N/S$. The solenoid is denoted as $CB0$, while the hadronic calorimeter is denoted as HE (end cap)/ HB (barrel)/ HF (forward) and the electromagnetic calorimeter as EE (end cap)/ EB (barrel). The green part represents the tracking system (tracker + pixel). Figure taken from [70].

443 **2.2.2.1 Muon system**

444 The outermost part of CMS consists of the muon system. The magnet return yoke is interleaved
 445 with gaseous detector chambers for muon identification and momentum measurement. The
 446 barrel contains muon stations arranged in five separate iron wheels, while in the end cap four
 447 muon stations are mounted onto three independent iron discs on each side. Each barrel wheel
 448 has 12 sectors in the azimuthal angle.

449 The muon system is divided into three parts, shown in Figure 2.6. The muon rate and neutron
 450 induced backgrounds are small and the magnetic field is very low for the barrel, thus CMS can
 451 use drift tube (DT) chambers. For the end caps however, the muon and background flux is much
 452 higher and there is a need to use cathode strip chambers (CSC) which are able to provide a
 453 faster response, higher granularity and have a better resistance against radiation. In order to
 454 form a redundant trigger system, resistive plate chambers (RPC) are added. This makes a total of 250 DT, 540 CSC and 610 RPC chambers. In Figure 2.5 the arrangement is shown.

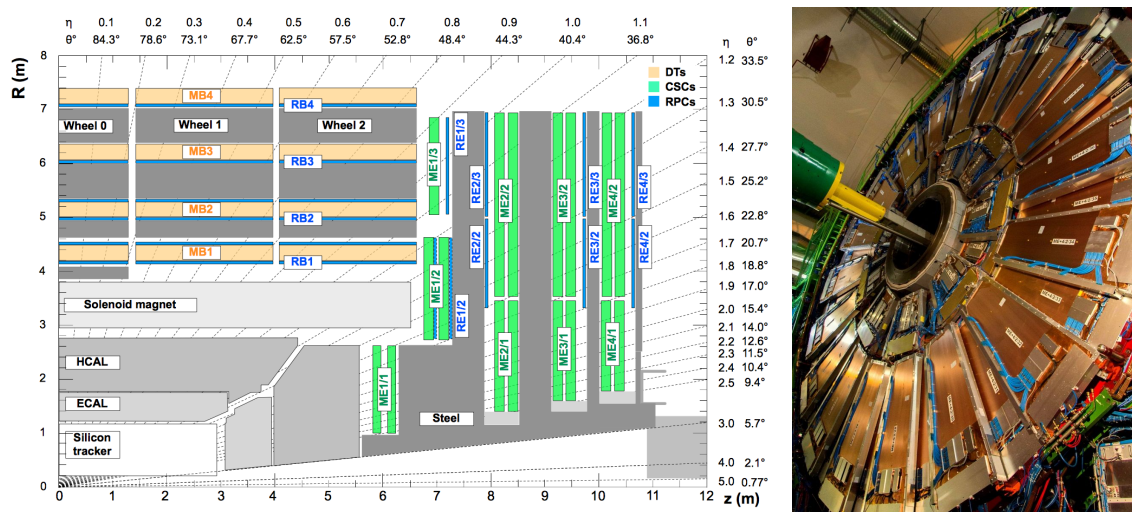


Figure 2.6: (Left) Schematic view of one quarter of the CMS muon system in the Run 1 configuration. The cathode strip chambers (CSC) are shown in green, the drift tubes (DT) are shown in yellow, while the resistive plate chambers (RPC) are shown in blue. Figure taken from [70]. (Right) Cathode strip chambers (ME+4/2 chambers on YE+3). Photo taken from [71].

455

456 Providing a measurement for $|\eta| < 1.2$, the DT chambers in the barrel are on average
 457 $2 \times 2.5 \text{ m}^2$ in size and consist of 12 layers of DT cells⁵ arranged in three groups of four. The
 458 $r\phi$ coordinate is provided by the two outside groups, while the middle group measures the
 459 z coordinate. For the outer muon station, the DT chambers contain only 8 layers of DT cells,
 460 providing a muon position in the $r\phi$ plane. There are four CSC stations in each end cap, providing
 461 muon measurements for $0.9 < |\eta| < 2.4$ (Run 1 configuration). These CSCs are multi-wired
 462 proportional chambers that consist of 6 anode wire planes crossed by 7 copper strips cathode
 463 panels in a gas volume. The r coordinate is provided by the copper strips, while the ϕ coordinate
 464 comes from the anode wires, giving a two dimensional position measurement. There are six

⁵The DT cells are 4 cm wide gas tubes with positively charged stretched wires inside.

465 layers of RPCs in the barrel muon system and one layer into each of the first three stations
 466 of the end cap. They are made from two high resistive plastic plates with an applied voltage
 467 and separated by a gas volume. Read out strips mounted on top of the plastic plates detect the
 468 signal generated by a muon passing through the gas volume. The RPCs provide a fast response
 469 with a time resolution of 1 ns and cover a range of $|\eta| < 1.8$ for the Run 1 configuration.

470 The muon system provides triggering on muons, identifying muons and improves the momentum
 471 measurement and charge determination of high p_T muons. On top of the muon system,
 472 the muon energy is deposited in the electromagnetic calorimeter, the hadronic calorimeter, and
 473 outer calorimeter. The high magnetic field enables an efficient first level trigger and allows a
 474 good momentum resolution of $\Delta p/p \approx 1\%$ for a p_T of 100 GeV and $\approx 10\%$ for a p_T of 1 TeV.
 475 There is an efficient muon measurement up to $|\eta| < 2.4$.

NOTE:
check numbers for run
2

476 2.2.2.2 Solenoid

477 Making use of the knowledge of previous experiments like ALEPH and DELPHI at LEP and H1
 478 at HERA, CMS choose for a large super conducting solenoid with a length of 12.9 m and a
 479 inner bore of 5.9 m [68]. With 2 168 turns, a current of 19.5 kA and a total energy of 2.7 GJ, a
 480 large bending power can be obtained for a modestly-sized solenoid. In order to ensure a good
 481 momentum resolution in the forward regions, a favourable length/radius was necessary. In
 482 [Figure 2.7](#), a photo of the CMS solenoid is shown.

483 The solenoid uses a high-purity aluminium stabilised conductor with indirect cooling from
 484 liquid helium, together with fully epoxy impregnation. A four-layer winding is implemented that
 485 can withstand an outward pressure of 64 atm. The NbTi cable is co-extruded by pure aluminium
 486 that acts as a thermal stabilizer and has an aluminium alloy for mechanical reinforcement. The
 487 return of the magnetic field is done by fives wheels, noted by YB in [Figure 2.5](#).

488 2.2.2.3 Hadronic calorimeter

489 The hadronic calorimeter (HCAL) is dedicated to precisely measure the energy of charged and
 490 neutral hadrons via a succession of absorbers and scintillators. This makes it crucial for physics
 491 analyses with hadronic jets or missing transverse energy. The HCAL barrel extends between
 492 $1.77 < r < 2.95$ m, where r is the radius in the transverse plane with respect to the beam. Due
 493 to space limitations, the HCAL needs to be as small as possible and is made from materials
 494 with short interaction lengths⁶. On top of this, the HCAL should be as hermetic as possible and
 495 extend to large absolute pseudo rapidities such that it can proved a good measurement of the
 496 missing transverse energy.

497 The quality of the energy measurements is dependent on the fraction of the hadronic shower
 498 that can be detected. Therefore, the HCAL barrel (HB) inside the solenoid is reinforced by an
 499 outer hadronic calorimeter between the solenoid and muon detectors (HO, see [Figure 2.8](#)),
 500 using the solenoid as extra absorber. This increases the thickness to 12 interaction lengths.

⁶Here the interaction length is the nuclear interaction length and this is the length needed for absorbing 36.7% of the relativistic charged particles. For the electromagnetic calorimeter this is defined in radiation length X_0 . The radiation length is the mean distance over which a high energy electron loses all but $1/e$ of its energy by bremsstrahlung.

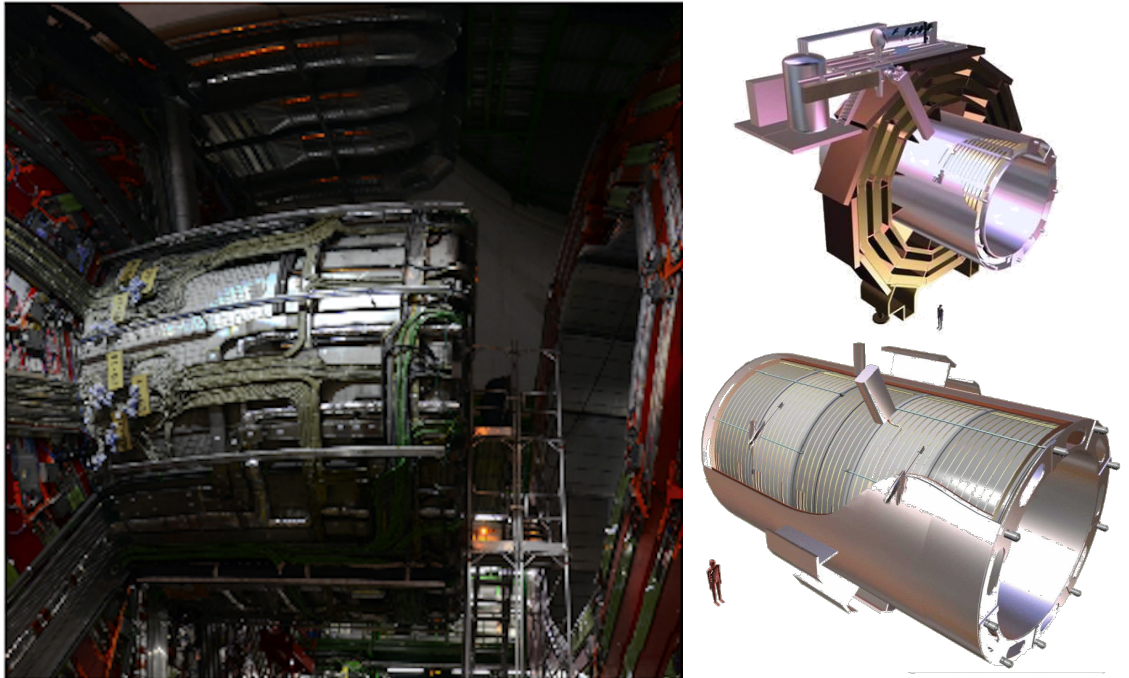


Figure 2.7: (Left) CMS solenoid during the long shutdown in 2013. (Right) An impression of the solenoid magnet taken from [72].

501 The HB and HO provide measurements for $|\eta| < 1.3$, while an end cap on each side (HE,
 502 $1.3 < |\eta| < 3$) and a forward calorimeter (HF, $3.0 < |\eta| < 5.2$) extend the pseudo rapidity
 503 range.

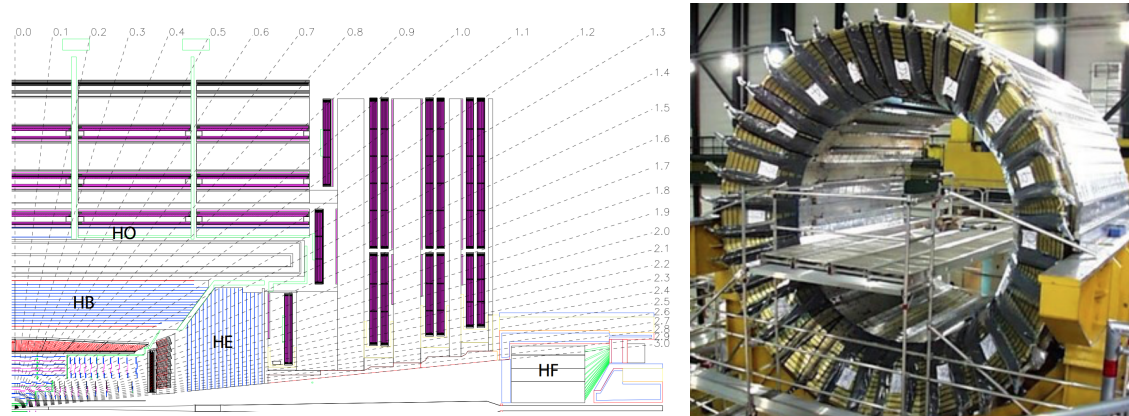


Figure 2.8: (Left) Longitudinal view of the CMS detector showing the locations of the HB, HE, HO, and HF calorimeters. Figure taken from [57]. (Right) CMS barrel calorimeter. Photo taken from [73].

504 The HB is made of 16 absorber plates where most of them are built from brass and others are
 505 made from stainless steel and is about five to ten interaction lengths thick. It is divided in $\eta \times \phi$
 506 towers and contains 2592 read out channels. The HO complements the HB and extends the
 507 reach up to twelve interaction lengths. This subsystem contains 2160 read out channels. The HE

is also composed of brass absorber plates and has a thickness corresponding to approximately ten interaction lengths, with 2592 read out channels.. The HF experiences intense particle fluxes with an expected energy of 760 GeV deposited on average in a proton interaction at a centre-of-mass of 14 TeV, compared to 100 GeV in the rest of the detector. Therefore, these are Cherenkov light detectors made of radiation hard quartz fibers. The main causes of such large energy events are high energy muons, cosmic particles and charged particles from late showering hadrons. During Run 1, it became clear that the glass windows of the photon multiplier tubes (PMTs) had to be replaced which was done during LS1 [74]. The HF represents 1728 read out channels.

The HCAL and electromagnetic calorimeter combined can measure the hadron energy with a resolution $\Delta E/E \approx 100\% \sqrt{E[\text{GeV}]} + 5\%$.

2.2.2.4 Electromagnetic calorimeter

The electromagnetic calorimeter (ECAL) is designed to measure the energy of photons and electrons and covers $|\eta| < 3$. It is an hermetic, homogeneous detector and consists of 75 848 lead tungstate (PbWO_4) crystals. These crystals have a fast response time - 80% of the light is emitted within 25 ns - and are radiation hard. The electromagnetic showers produced by passing electrons or photons ionize the crystal atoms which emit a blue-green scintillation light, that is collected by silicon avalanche photodiodes (APDs) in the barrel and vacuum phototriodes (VPTs) in the end caps. The crystals and the APD response is sensitive to temperature changes and require a stable temperature.

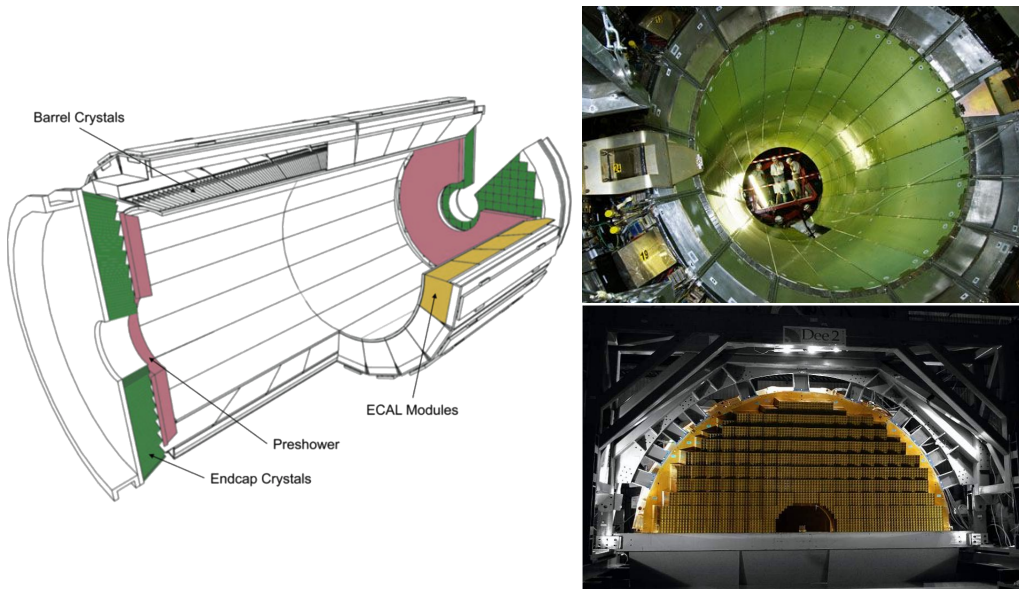


Figure 2.9: (Left) Schematic cross section of the electromagnetic calorimeter taken from [57]. (Right top) The ECAL barrel during construction [75]. (Right bottom) One half of an EE [76].

There are three regions: a central barrel (EB), an endcap region (EE) and a preshower (ES) (Figure 2.9). The EB has an inner radius of 129 cm and corresponds to a pseudo rapidity of $0 < |\eta| < 1.479$. At a distance of 314 cm from the vertex and covering a pseudo rapidity of $1.479 <$

531 $|\eta| < 3.0$, are the EE. They consist of semi-circular aluminium plates from which structural
 532 units of 5×5 crystals (super crystals) are supported. The ES is placed in front of the crystal
 533 calorimeter over the end cap pseudo rapidity range with two planes of silicon strip detectors as
 534 active elements.

The electromagnetic shower will typically involve more than one channel. More than 90% of the energy of a 35 GeV electron or photon is contained in a 5×5 matrix of crystals. Therefore, a clustering algorithm is performed in order to associate the energy deposits to the particles impinging the calorimeter. The achieved precision [77] for the barrel is 2.10^{-3} rad in ϕ and 10^{-3} in η . For the end caps this is 5.10^{-3} rad in ϕ and 2.10^{-3} in η . The energy is reconstructed by a supercluster algorithm, taking into account energy radiated via bremsstrahlung or conversion [57]. The energy resolution is given by

$$\frac{\sigma(E)}{E} = \frac{2.8\%}{\sqrt{E}} \oplus \frac{0.128}{E(GeV)} \oplus 0.3\%, \quad (2.5)$$

535 in the absence of a magnetic field, where the contributions come from the stochastic, noise and
 536 constant terms respectively. The dominating term is the constant term ($E_{shower} \approx 100$ GeV)
 537 and thus the performance is highly dependent on the quality of calibration and monitoring .

538 2.2.2.5 Inner tracking system and operations

539 The tracking system (tracker) [78] is the detecting unit closest to the point of interaction.
 540 Responsible for the reconstruction of trajectories from charged particles with $|\eta| < 2.5$ that are
 541 bent by the magnetic field, it provides a measurement of the momentum. The tracker is also
 542 responsible for the determination of the interaction point or vertex. It should be able to provide
 543 high granularity as well as fast read out, and be able to endure high radiation. For this reason,
 544 the CMS collaboration choose silicon detector technology.

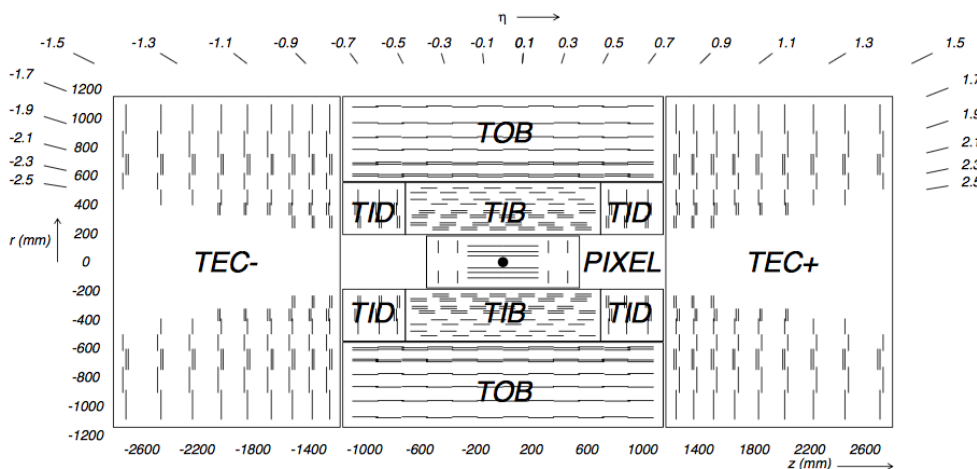


Figure 2.10: Schematic cross section through the CMS tracker. Each line represents a detector module. Double lines indicate back-to-back modules that deliver stereo hits. Figure taken from [57].

545 The tracking system consists of a cylinder of 5.8 m long and 2.5 m in diameter. It is immersed
 546 in a co-axial magnetic field of 3.8 T provided by the solenoid. As shown in Figure 2.10, the

tracker is built up from a large silicon strip tracker with a small silicon pixel tracker inside. The inner pixel region ($4.4 < r < 10.2$ cm), gets the highest flux of particles. Therefore, pixel silicon sensors of $100 \times 150 \mu\text{m}^2$ are used. It consists of three cylindrical barrels that are complemented by two discs of pixel modules at each side. The silicon strip tracker ($20 < r < 116$ cm) has three subdivisions. The Tracker Inner Barrel and Discs (TIB, TID, see Figure 2.12) are composed of four barrel layers accompanied by three discs at each end. The outer part of the tracker - Tracker Outer Barrel (TOB) - consists of 6 barrel layers. In the outer discs, there are nine discs of silicon sensors, referred to as Tracker End Caps (TEC).

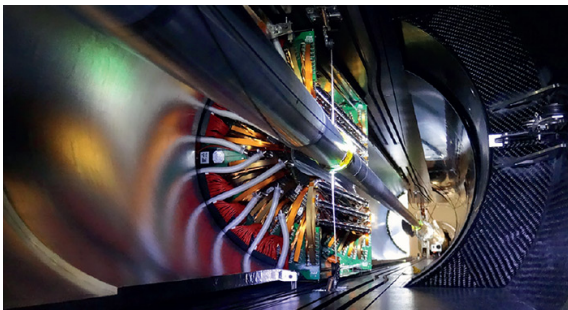


Figure 2.11: The pixel barrel being re-installed after the Long Shutdown in 2015, around the beam pipe at CMS [79].



Figure 2.12: First half of the inner tracker barrel, consisting of three layers of silicon modules [80].

The pixel, shown in Figure 2.11, has 1440 modules that cover an area of about 1 m^2 and have 66 million pixels. It provides a three-dimensional position measurement of the hits arising from the interaction from charged particles with the sensors. In transverse coordinate ($r\phi$), the hit position resolution is about $10 \mu\text{m}$, while $20\text{-}40 \mu\text{m}$ is obtained in the longitudinal coordinate (z). The sensor plane position provides the third coordinate. The TIB/TID, shown in Figure 2.12, delivers up to four $r\phi$ -measurements using a $320 \mu\text{m}$ thick silicon micro-strip sensors. These sensors are placed with their strips parallel to the beam axis in the barrel and radial in the discs. In the TIB, the first two layers have a strip pitch of $80 \mu\text{m}$, while the remaining to have a strip pitch of $120 \mu\text{m}$. This leads to a respective single point resolution of $23 \mu\text{m}$ and $35 \mu\text{m}$. For the TID, the pitch varies between $100 \mu\text{m}$ and $141 \mu\text{m}$. The TOB provides six $r\phi$ -measurements with a single point resolutions of $53 \mu\text{m}$ in the first four layers, and $35 \mu\text{m}$ in the last two layers. It consists of $500 \mu\text{m}$ thick micor strip sensors with strip pitches of $183 \mu\text{m}$ (first 4 layers) or $122 \mu\text{m}$ (last two layers). The TEC provides up to 9 ϕ -measurements via 9 discs consisting of up to 7 rings of silicon microstrip sensor of $97 \mu\text{m}$ to $184 \mu\text{m}$ average pitch.

A second co-ordinate measurement (z in the barrel, r on the discs) is provided through the use of a second micro strip detector module mounted back-to-back with a stereo angle of 100 mrad. This is done on the modules in the first two layers and rigns of the TIB, TID, and TOB, as wel as rigns 1,2, and 5 of the TECs (blue line in Figure 2.10). The resolution in the z direction is approximately $230 \mu\text{m}$ in the TIB and $530 \mu\text{m}$ in the TOB, and is varying with pitch in the TID and TEC. To allow overlay and avoid gaps in acceptance, each module is shifted slightly in r or z with respect to its neighbouring modules within a layer. With this detector lay out, at least nine points per charged particle trajectory can be measured in an $|\eta|$ range up to 2.4, where at least four of them being two dimensional. The CMS silicon tracker provides 9.3 million readout

578 channels and covers an active area of about 198 m².

579 2.2.3 Data acquisition

580 At a design luminosity of $10^{34} \text{ m}^{-2}\text{s}^{-1}$, the proton interaction rate exceeds 1 GHz. Given the
 581 large size of an event (about 1 MB), the high crossing rate, and that typically tens of collisions
 582 happen at the same time, it is impossible for the CMS experiment to store all the data generated.
 583 In order to deal with the large amount of data, a two level trigger system has been put in place.
 584 The first level (Level-1) is a custom hardware system, while a second high level trigger (HLT) is
 585 software based running on a large farm of computers.

586 CMS Level-1 Trigger

587 The Level-1 Trigger has to be a flexible, maintainable system, capable of adapting to the
 588 evolving physics programme of CMS [81]. Its output rate is restricted to 100 kHz imposed
 589 by the CMS readout electronics. It is implemented by custom hardware and selects events
 590 containing candidate objects - e.g. ionization deposits consistent with a muon, or energy clusters
 591 corresponding to an electron / photon / tau lepton / missing transverse energy / jet. Collisions
 592 with large momenta can be selected by using scalar sum of the transverse momenta of the jets.

593 By buffering the raw data from the CMS subdetectors in front-end drivers, the Level-1 Trigger
 594 has a pipeline memory of 3.2 μs to decide whether to keep an event or reject it. The trigger
 595 primitives (TP) from the calorimeters and muon detectors are processed in several steps and
 596 combined into a global trigger. This information is then combined with the input from the other
 597 subsystems for the HLT. The separate inputs are synchronized to each other and the LHC orbit
 598 clock and sent to the global trigger module. Here, Level-1 Trigger algorithms are performed
 599 within 1 μs to decide whether to keep the event.

600 CMS HLT Trigger

601 The HLT is an array of commercially available computers with a programmable menu that has
 602 an output rate of on average 400 Hz for off-line event storage. The data processing is based on
 603 an HLT path. This is a set of algorithmic steps to reconstruct objects to define selection criteria.
 604 Here, the information of all subdetectors can be used to perform algorithms on higher level
 605 reconstructed objects.

606 2.2.4 Phase 1 upgrades

607 Before the start of taking collision data for 13 TeV operations on 3 June 2015, CMS had a long
 608 shutdown (LS1) [82]. During this shutdown, the section of the beryllium beam pipe within CMS
 609 was replaced by a narrower one. This operation required the pixel to be removed and reinserted
 610 into CMS. In Run 2, higher particle fluxes with respect to Run 1 are expected. To avoid long
 611 damage caused by the intense particle flux at the heart of CMS, the tracker is been made ready
 612 to operate at much lower temperature than during Run 1. The electromagnetic calorimeter
 613 preshower system had been damaged during Run 1, therefore the preshower discs were removed,
 614 repaired and reinstalled successfully inside CMS in 2014. To help the discrimination between
 615 interesting low momentum muons coming from collisions and muons caused by backgrounds, a

616 fourth triggering and measurement station for muons was added in each of the end caps. Several
 617 new detectors were installed into CMS for measuring the collision rate within the detector and
 618 monitors beam related backgrounds.

619 During the LS1, the muon system underwent major upgrades [83, 84]. In the fourth station
 620 of each end cap, the outermost rings of CSC and RPC chambers were completed, providing an
 621 angular coverage of $1.2 < |\eta| < 1.8$ for Run 2, increasing the system redundancy, and allowing
 622 tighter cuts on the trigger quality. In order to reduce the environmental noise, outer yoke discs
 623 have been placed on both sides for the end caps. At the innermost rings of the first station,
 624 the CSCs have been upgraded by refurbishing the readout electronics to make use of the full
 625 detector granularity instead of groups of three as was the case for Run 1. In Figure 2.6 (right),
 626 the refurbishing of the CSCs is shown.

627 Since the HF experiences intense particle fluxes, it became clear during Run 1 that the glass
 628 windows of the PMTs need replacing. For the ECAL in Run 1, the energy reconstruction happened
 629 via a weighted sum of the digitized samples [85]. For Run 2 however, the reconstruction had
 630 to be made more resistant for out of time pile up and a multi-fit approach has been set into
 631 place. In this approach, the pulse shape is modelled as a sum of one in-time pulse plus the out
 632 of time pulses [77]. The energy resolution is better than 2% in the central barrel region and
 633 2-5 % elsewhere.

During the first data taking period of the LHC (2010 to 2013), the tracker operated at $+4^\circ\text{C}$. With the higher LHC beam intensities from 2015 onwards, the tracker needs to be operated at much lower temperatures. The reason for this is that with intense irradiation, the doping concentration changes, the leakage current increases proportional to the fluence and the charge collection efficiency decreases due to charge trapping. Mostly the leakage current (I) is affected by the temperature change:

$$I \propto T^2 e^{-\frac{E_g}{2kT}}, \quad (2.6)$$

634 where T is the operating temperature, E_g the band gap and k the Boltzmann constant. There is
 635 approximately a factor 15 between the leakage currents at room temperatures and at -10°C .

636 During the LS1, the CMS cooling plant was refurbished [86] and the fluorocarbon cooling
 637 system overhauled. To help to suppress the humidity inside the tracker, new methods for vapour
 638 sealing and insulation were applied. Furthermore, several hundred high-precision sensors are
 639 used to monitor the humidity and temperature. In order to get as dry air as possible, a new
 640 dry-gas plant provides eight times more dry gas (air or nitrogen) than during the first run, and
 641 allows regulation of the flow. As a final addition, the cooling bundles outside the tracker are
 642 equipped with heater wires and temperature sensors in order to maintain safe operations above
 643 the cavern dew point. For the data taking in 2015-2016, the tracker operated at -15°C .

644 In Run 2, with the increase in centre of mass energy and a higher luminosity, a larger number
 645 of simultaneous inelastic collisions per crossing is expected with respect to Run 1. For this, the
 646 CMS Level-1 has been upgraded [87]. All hardware, software, databases and the timing control
 647 system have been replaced for Run 2, where the main changes are that the muon system now
 648 uses the redundancy of the muon detector system earlier to make a high resolution muon trigger.

649 Other upgrades are that the calorimeter system isn't bound any more for streaming data and
650 the global trigger has more Level-1 Trigger algorithms.

651 After the first half of Run 2, the innermost part of detection material in CMS (pixel) was
652 upgraded by adding a fourth layer , enhancing the particle tracking capabilities of CMS. The
653 data used in the framework of this thesis however is from before this upgrade. More information
654 on the Pixel upgrade can be found in Refs. [88, 89].

655 **2.2.5 CMS computing model**

656 The selected data is stored, processed and dispersed via the Worldwide Large Hadron Collider
657 GRID (WLCG) [90, 91]. This has a tiered structure that functions as a single, coherent system.

658 At CERN and the Wigner Research Center for physics, a single Tier-0 is located. The raw data
659 collected by CMS is archived here, and a first reconstruction of the data is done. This data is
660 then already in a file format usable for physics analysis. Furthermore, it is able to reprocess
661 data when new calibrations become available. The Tier-0 site distributes this data to a total of
662 14 Tier-1 centres. They carry out data reprocessing and store real data as well as simulated
663 data. The Tier-1 further distributes the data to over 150 Tier-2 centres. These make the data
664 accessible for physics analysis and are also being used for the production of simulated data. The
665 data is made accessible for physicists around the world.

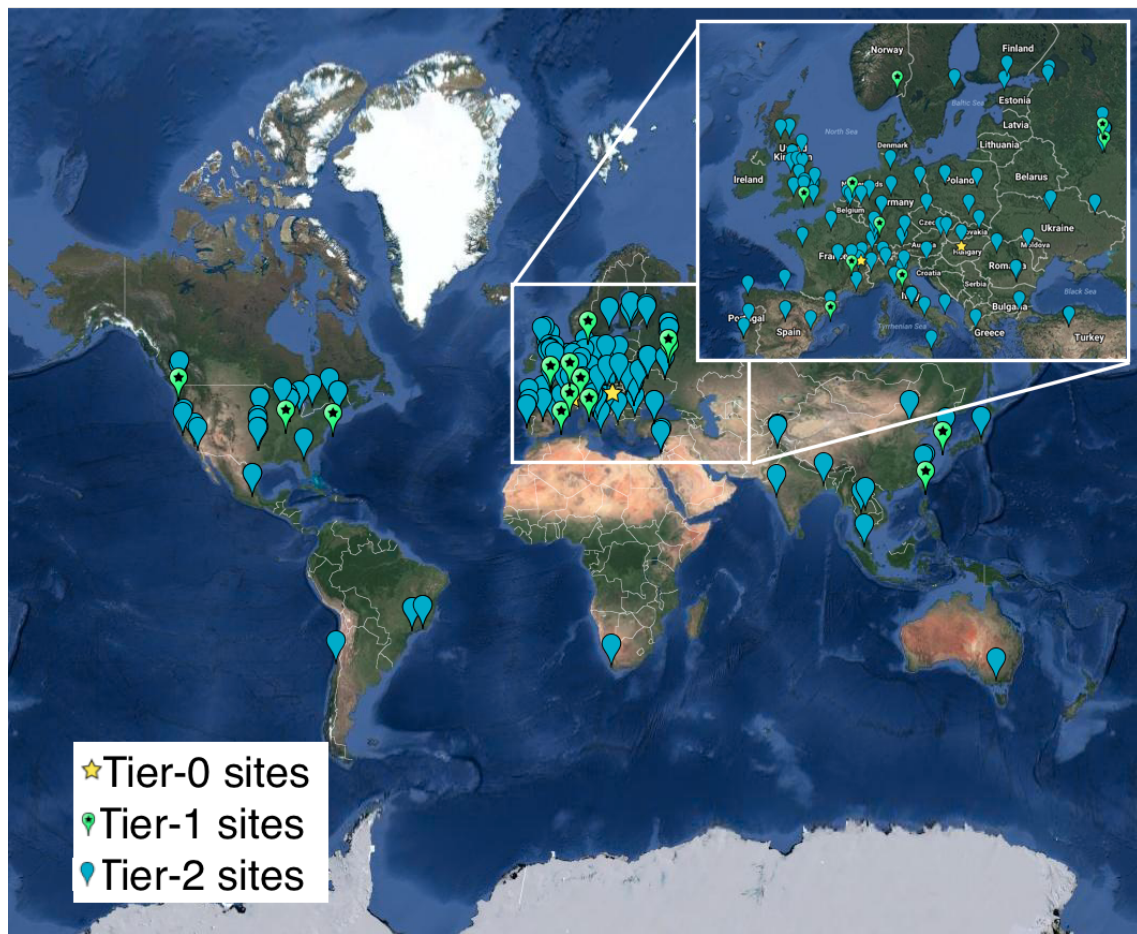


Figure 2.13: Worldwide LHC Computing Grid in 2017 [92].

3

666

Analysis techniques

667 In order to disentangle the collisions coming from high energy experiments, many tools have
668 been developed. In [Section 3.1](#), the predictions behind hadron collision at high energies are
669 presented. These are used to generate events via Monte Carlo event generators, explained in
670 [Section 3.2](#). Machine learning helps to differentiate between signal- and background like events.
671 In [Section 3.3](#), the multivariate technique of boosted decision trees is explained. This yields
672 powerful discriminants for separating signal and background events and provides distributions
673 that go through template-based maximum likelihood fits. The fitting method used in the search
674 presented in this thesis is discussed in [Section 3.4](#).

675 3.1 Hadron collisions at high energies

In hadron collisions at sufficiently high momentum transfer, all partons can be approximated as free making it possible to treat hadron-hadron scattering as a single parton-parton interaction. The momentum of the parton can then be expressed as a fraction of the hadron momentum

$$\vec{p}_{\text{parton}} = x \vec{p}_{\text{hadron}}, \quad (3.1)$$

where x is referred to as the Björken scaling variable. The interaction $p_A p_B \rightarrow X$ can then be factorised in terms of partonic cross sections $\hat{\sigma}_{ij \rightarrow X}$ [93]

$$\sigma_{p_A p_B \rightarrow X} = \sum_{ij} \iint dx_1 dx_2 f_i^A(x_1, Q^2) f_j^B(x_2, Q^2) d\hat{\sigma}_{ij \rightarrow X}, \quad (3.2)$$

676 where i and j are the partons resolved from protons A and B, $f_i(x_i, Q^2)$ the parton density
677 functions (PDF), and Q^2 the factorisation scale more commonly denoted as μ_F . The factorisation
678 scale is the scale at which the hadronic interaction can be expressed as a product of the partonic
679 cross section and the process independent PDF. In [Figure 3.1](#), the kinematic regions in x and
680 μ_F are shown for fixed target and collider experiments.

681 The parton density functions (PDF) [94–96] give the momentum distribution of the proton
682 amongst its partons at an energy scale μ_F . These function can not be determined from first prin-
683 ciples and have to obtained from global fits to data. The PDFs are obtained from measurements on

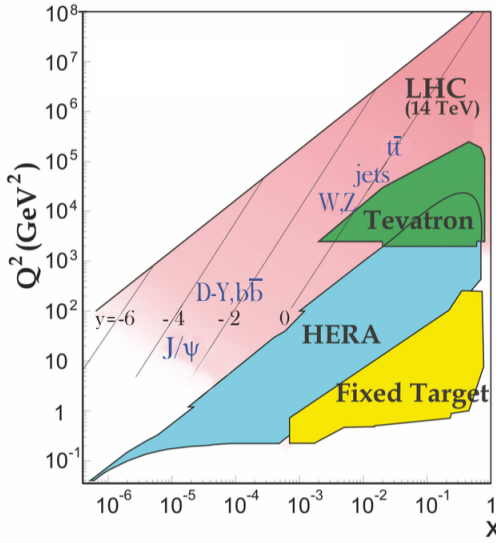


Figure 3.1: Kinematic regions in momentum fraction x and factorisation scale Q^2 probed by fixed-target and collider experiments. Some of the final states accessible at the LHC are indicated in the appropriate regions, where y is the rapidity. In this figure, the incoming partons have $x_{1,2} = (M/14\text{TeV})e^{\pm y}$ with $Q = M$ where M is the mass of the state shown in blue in the figure. For example, exclusive J/ψ and Υ production at high $|y|$ at the LHC may probe the gluon PDF down to $x \sim 10^{-5}$. Figure taken from [6].

684 deep inelastic scattering using lepton-proton collision by the HERA collider [97], supplemented
 685 with proton-antiproton collisions from Tevatron at Fermi lab [98], and proton collision data
 686 from the ATLAS, CMS and LHCb collaborations at the LHC (Run 1) [99]. These measurements
 687 are included in global PDF sets known as the PDF4LHC recommendation [96]. From their
 688 measurement at scale μ_F these PDFs can be extrapolated using the DGLAP equations [100].
 689 The PDFs are used to calculate the cross section of a certain process and are therefore used
 690 as input for the Monte Carlo generators used to make the simulated data samples at the LHC.
 691 In the framework of this thesis, the NLO PDF4LHC15_100 set is used. This set is an envelope
 692 of three sets, CT14, MMHT2014 and NNPDF3.0 [96]. In Figure 3.2 the dependency of the PDFs
 693 on the momentum fraction x is shown for the NNPDF3.0 set on hadronic scale ($\mu_F^2 = (10\text{GeV})^2$)
 694 and LHC scale ($\mu_F^2 = (10^4\text{GeV})^2$). For most values of the momentum fraction, the gluon density
 695 dominates, meaning that it is easier to probe muons than the quarks. For x close to one, the
 696 parton densities of the up and down quarks (the valence quarks of the proton) dominate over
 697 the gluon density. The charm, anti-up, and anti-down quarks have lower densities in general
 698 since those are sea quarks which originate in the proton only through gluon splitting. The
 699 resolution scale Q^2 is typically taken to be the energy scale of the collision. For the top quark pair
 700 production a scale of $Q^2 = (350\text{GeV})^2$ is chosen, meaning that the centre-of-mass energy of the
 701 hard interaction is about twice the top quark mass. The uncertainty on the parton distributions
 702 is evaluated using the Hessian technique [101], where a matrix with a dimension identical to
 703 the number of free parameters needs to be diagonalised. In the case of PDF4LHC15_100 set, this
 704 translates into 100 orthonormal eigenvectors and 200 variations of the PDF parameters in the
 705 plus and minus direction.

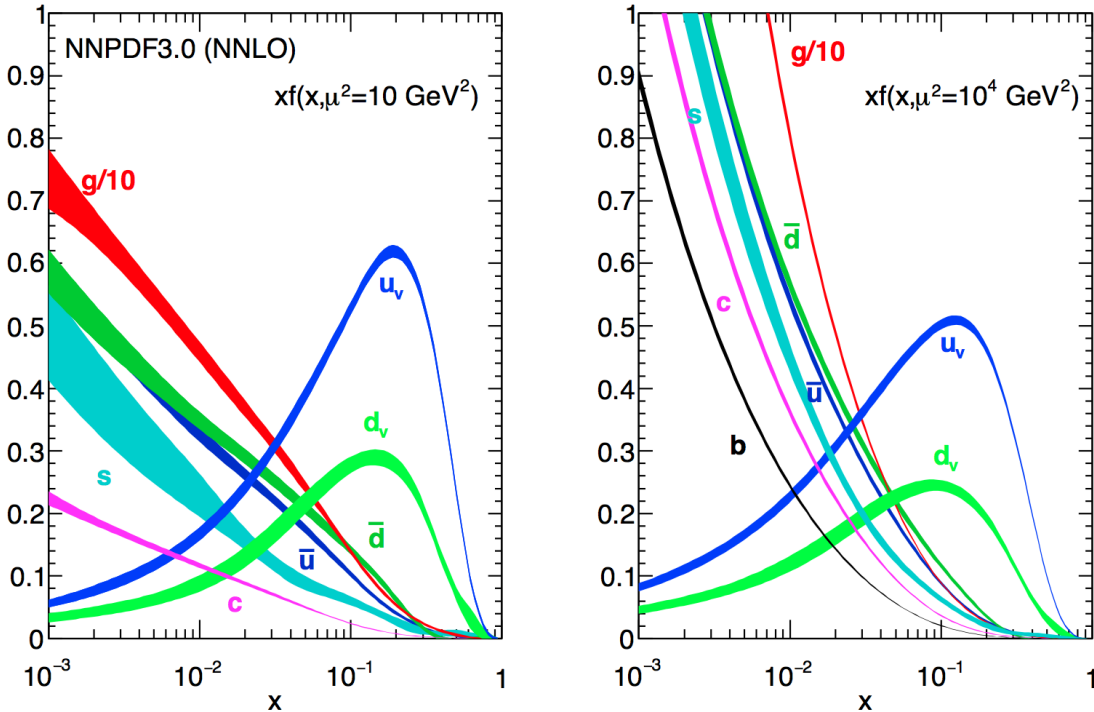


Figure 3.2: The momentum fraction x times the parton distribution functions $f(x)$, where $f = u_v, d_v, \bar{u}, \bar{d}, s, c$, or g as function of the momentum fraction obtained in the NNLO NNPDF3.0 global analysis at factorisation scales $\mu^2 = 10 \text{ GeV}^2$ (left) and $\mu^2 = 10^4 \text{ GeV}^2$ (right), with $\alpha_s(M_Z^2) = 0.118$. The gluon PDF has been scaled down by a factor of 0.1. Figure taken from [6].

At high energies, divergences can appear from quantum fluctuations. For the theory still to be able to describe the experimental regime, a renormalization scale μ_R is used to redefine physical quantities. A consequence of this method is that the coupling constants will run as function of μ_R . Beyond this scale, the high energy effects such as the loop corrections to propagators (self energy) are absorbed in the physical quantities through a renormalization of the fields. In particular the running behaviour of the strong coupling constant¹ α_s is found to be

$$\alpha_s = \frac{\alpha_s(\mu_0^2)}{1 + \alpha_s(\mu_0^2) \frac{33-2n_f}{12\pi} \ln\left(\frac{|\mu_R^2|}{\mu_0^2}\right)}, \quad (3.3)$$

with n_f the number of quarks and μ_0 the reference scale on which the coupling is known. The current world average of the strong coupling constant at the Z boson mass is $\alpha_s(\mu_R = m_Z) = 0.1181 \pm 0.0011$ [6]. From Equation 3.3 one can see easily that the coupling strength decreases with increasing renormalization scale, this known as asymptotic freedom. Additionally, following the behaviour of $\alpha_s(\mu_R^2)$, a limit $\Lambda_{\text{QCD}} \approx 200 \text{ MeV}$ is found for which α_s becomes larger than one. Under this limit, the perturbative calculations of observables can no longer be done.

¹The strong coupling constant is defined as $\alpha_s = \frac{g_s^2}{4\pi}$.

Cross sections can be written in terms of interacting vertices contributing to the matrix element (ME) originating from elements of a perturbative series [102], allowing them to be expanded as a power series of the coupling constant α

$$\sigma = \sigma_{\text{LO}} \left(1 + \left(\frac{\alpha}{2\pi} \right) \sigma_1 + \left(\frac{\alpha}{2\pi} \right)^2 \sigma_2 + \dots \right). \quad (3.4)$$

712 Leading order (LO) accuracy contains the minimal amount of vertices in the process, then
 713 depending on where the series is cut off one speaks of next-to-leading order (NLO), or next-
 714 to-next-to-leading order (NNLO) accuracy in α . Predictions including higher order correction
 715 tend to be less affected by theoretical uncertainties originating from a variation of the chosen
 716 renormalization and factorisation scales.

717 3.2 Event generation

718 In order to compare reconstructed data with theoretical predictions, collision events are gener-
 719 ated and passed through a simulation of the CMS detector and an emulation of its readout. For
 720 the detector simulation, a so-called Full Simulation package [103, 104] based on the Geant4
 721 toolkit [105] is employed. It allows a detailed simulation of the interactions of the particles
 722 with the detector material.

723 3.2.1 Fundamentals of simulating a proton collision

724 The procedure of to generate $\text{pp} \rightarrow \text{X}$ events can be subdivided into sequential steps [106–108],
 725 as shown in Figure 3.3.

726 The interaction of two incoming protons is often soft and elastic leading to events that are not
 727 interesting in the framework of this thesis. More intriguing are the hard interaction between two
 728 partons from the incoming protons. The matrix elements of a hard scattering process of interest
 729 is the starting point of the generation of events. Monte Carlo techniques are used to sample the
 730 corresponding cross section integral and the resulting sample of events reflect the probability
 731 distribution of a process over its final state phase space. After obtaining the sample of events of
 732 the hard interaction, a parton shower (PS) program is used to simulate the hadronisation of
 733 final state partons into hadrons which then decay further. Additionally, radiation of soft gluons
 734 or quarks from initial or final state partons is simulated. These are respectively referred to as
 735 initial state radiation (ISR) or final state radiation (FSR). Contributions from soft secondary
 736 interactions, the so-called underlying event (UE), and colour reconnection effects are also taken
 737 into account. A brief overview of the employed programs used for the event generation of the
 738 signal and main background processes used in the search presented in the thesis are given in
 739 Section 3.2.2.

NOTE: 737
Should I
add more 738
details? 739

740 3.2.2 Programs for event generation

741 The FEYNRULES package [109] allows the calculation of the Feynman rules in momentum space
 742 for any quantum field theory model. By use of a Lagrangian, the set of Feynman rules associated
 743 with this Lagrangian are calculated. Via the Universal FeynRules Output (UFO) [110] the
 744 results are then passed to matrix element generators.

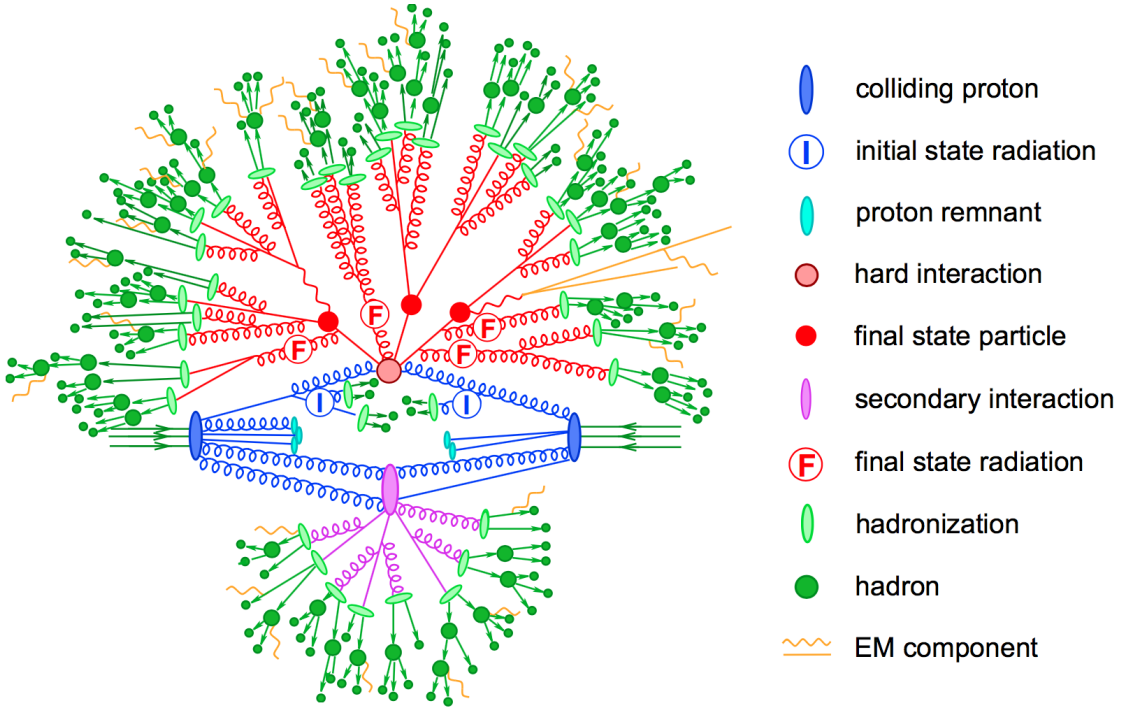


Figure 3.3: Sketch of a hadron collision as simulated by a Monte-Carlo event generator. The red blob in the centre represents the hard collision, surrounded by a tree-like structure representing Bremsstrahlung as simulated by parton showers. The purple blob indicates a secondary hard scattering event. Parton-to-hadron transitions are represented by light green blobs, dark green blobs indicate hadron decays, while yellow lines signal soft photon radiation. Figure taken from [108].

745 The MadGraph program [111] is used to interpret the physics model and calculate the cor-
 746 responding Feynman diagrams and matrix elements. After this, MadEvent [112] is used to
 747 calculate the corresponding partons. These generated parton configurations are then merged
 748 with Pythia [113–115] parton showers using the MLM merging scheme [116].

749 The MadGraph5_aMC@NLO program [117] combines the LO MadGraph [111] and the aMC@NLO
 750 program into a common framework. This combination supports the generation of samples
 751 at LO or NLO together with a dedicated matching to parton showers using the MLM [116]
 752 or FXFX [118] schemes respectively. The FXFX scheme produces a certain fraction of events
 753 with negative weights originating from the subtraction of amplitudes that contain additional
 754 emissions from the NLO matrix element to prevent double-counting.

755 The POWHEG box (versions 1,2) [119–124] contains predefined implementations of various
 756 processes at NLO. It applies the POWHEG method for ME- to PS- matching, where the hardest
 757 radiation generated from the ME has priority over subsequent PS emission to remove the overlap
 758 with the PS simulation.

759 The JHU generator (version 7.02) [125–128] is used to generate the parton level information
 760 including full spin and polarization correlations. It is commonly used for studying the spin and
 761 parity properties of new resonances such as $ab \rightarrow X \rightarrow VV$, where $V = Z, W, \gamma$.

762 The generation of events from processes involving the production and decay of resonances
 763 creates a computational heavy load, especially at NLO. The narrow width approximation
 764 assumes that the resonant particle is on-shell. This makes the production and decay amplitude
 765 factorize, allowing to perform the simulation of the production and decay of heavy resonances
 766 like top quarks or Higgs bosons to be performed in separate steps. The MadSpin program [129]
 767 extends this approach and accounts for off-shell effects through a partial reweighting of the
 768 events. Additionally, spin correlation effects between production and decay products are taken
 769 into account.

770 The Pythia program (versions 6,8) [113–115] generates events of various processes at LO.
 771 However more commonly it is only used for its PS simulation and is then interfaced with other
 772 LO and NLO event generators to perform subsequent parton showering, hadronisation, and
 773 simulation of the underlying event. In this thesis the underlying event tunes [130] are the
 774 CUETP8M2T4, CUETP8M1 and CUETP8M2.

775 The detector response is simulated via the Geant4 [105] program. This program tracks the
 776 particles through the detector material via a detailed description of the detector and generates
 777 several hits throughout several sensitive layers. In addition, the response of the detector
 778 electronics to these hits are simulated.

779 3.2.3 Generating FCNC top-Z interactions

780 The FCNC processes are generated by interfacing the Lagrangian in Equation 1.25 with
 781 MadGraph5_aMC@NLO by means of the FeynRules package and its Universal FeynRules
 NOTE: W₇₈₂
 RH and not₇₈₃ Output format. The complex chiral parameters are arbitrary chosen to be $f_{Xq}^L = 0$ and $f_{Xq}^R = 1$.
 LH?
 784 The signal rates are estimated by use of the MadGraph5_aMC@NLO program for estimating the
 785 partial widths. The anomalous couplings are left free to float for this estimation, and only one
 coupling allowed to be non-vanishing at a time. The results are presented in Table 3.1.

786 The anomalous single top cross sections are calculated by convolution of the hard scattering
 787 matrix elements with the LO order set of NN2.3LO [Ball:2012cx] partons densities. The NLO
 788 effects are modelled by multiplying each LO cross section by a global k -factor. The LO single
 789 top production cross section and the global k -factors for the top-Z production are shown in
 790 Table 3.2. The hard scattering events are then matched to parton showers to Pythia to account
 791 for the simulation of the QCD environment relevant for hadronic collisions.

The top pair cross sections are derived from the SM $t\bar{t}$ cross section, calculated with MadGraph5_aMC@NLO at NLO ($\sigma_{t\bar{t}} = 6.741 \cdot 10^2 \text{ pb}$), and considering the decay $t\bar{t} \rightarrow (bW^\pm)(X_{qt})$. The branching ratio $\mathcal{B}(t \rightarrow bW^\pm)$ is assumed to be equal to one and the FCNC branching ratio is calculated as

$$\mathcal{B}(t \rightarrow qX) = \frac{\Gamma_{t \rightarrow qX}}{\Gamma_t^{\text{SM}} + \Gamma_t^{\text{FCNC}}} \approx \frac{\Gamma_{t \rightarrow qX}}{\Gamma_t^{\text{SM}}}, \quad (3.5)$$

NOTE: 792 where $\Gamma_{t \rightarrow qX}$ is given in Table 3.1, and the assumption $\Gamma_t^{\text{FCNC}} \ll \Gamma_t^{\text{SM}}$ is made. In Table 3.3 the
 793 resulting NLO cross sections for the top-Z FCNC interactions are given.

794 The generation at leading order of the single top FCNC process $tZ + 0,1 \text{ jet}$ including a merging
 795 technique can not be done since the $tZ+1 \text{ jet}$ also contains contribution of top pair where one

NOTE: 792
 these par-
 793 tial widths
 are at LO,
 how does
 794 this relate
 to NLO that
 is used? Or
 795 is there no
 difference?

Table 3.1: Leading order partial widths related to the anomalous decay modes of the top quark, where the new physics scale Λ is given in GeV.

| Anomalous coupling | vertex | Partial decay width (GeV) | |
|------------------------------|-------------|---------------------------|----------------------------------|
| κ_{gqt}/Λ | $t g u$ | $3.665220 \cdot 10^5$ | $(\kappa_{tg u}/\Lambda)^2$ |
| | $t g c$ | $3.664620 \cdot 10^5$ | $(\kappa_{tg c}/\Lambda)^2$ |
| $\kappa_{t\gamma q}/\Lambda$ | $t\gamma u$ | $1.989066 \cdot 10^4$ | $(\kappa_{t\gamma u}/\Lambda)^2$ |
| | $t\gamma c$ | $1.988904 \cdot 10^4$ | $(\kappa_{t\gamma c}/\Lambda)^2$ |
| κ_{tZq}/Λ | $tZ u$ | $1.637005 \cdot 10^4$ | $(\kappa_{tZ u}/\Lambda)^2$ |
| | $tZ c$ | $1.636554 \cdot 10^4$ | $(\kappa_{tZ c}/\Lambda)^2$ |
| ζ_{tZq} | $tZ u$ | $1.685134 \cdot 10^{-1}$ | $(\zeta_{tZ u})^2$ |
| | $tZ c$ | $1.684904 \cdot 10^{-1}$ | $(\zeta_{tZ c})^2$ |
| η_{tHq} | $tH u$ | $1.904399 \cdot 10^{-1}$ | $(\eta_{tH u})^2$ |
| | $tH c$ | $1.904065 \cdot 10^{-1}$ | $(\eta_{tH c})^2$ |

Table 3.2: Leading order single top production cross section for $pp \rightarrow tZ$ or $\bar{t}Z$, where the new physics scale is given in GeV. The NLO k -factors [131] are given in the last column.

| Anomalous coupling | Cross section (pb) | NLO k -factor |
|------------------------------|--------------------|----------------------------------|
| $\kappa_{tg u}/\Lambda$ | $3.272 \cdot 10^7$ | $(\kappa_{tg u}/\Lambda)^2$ |
| $\kappa_{tg c}/\Lambda$ | $3.021 \cdot 10^6$ | $(\kappa_{tg c}/\Lambda)^2$ |
| $\kappa_{t\gamma u}/\Lambda$ | $2.260 \cdot 10^5$ | $(\kappa_{t\gamma u}/\Lambda)^2$ |
| $\kappa_{t\gamma c}/\Lambda$ | $2.654 \cdot 10^4$ | $(\kappa_{t\gamma c}/\Lambda)^2$ |
| $\kappa_{tZ u}/\Lambda$ | $1.728 \cdot 10^6$ | $(\kappa_{tZ u}/\Lambda)^2$ |
| $\kappa_{tZ c}/\Lambda$ | $2.040 \cdot 10^5$ | $(\kappa_{tZ c}/\Lambda)^2$ |
| $\zeta_{tZ u}$ | 7.484 | $(\zeta_{tZ u})^2$ |
| $\zeta_{tZ c}$ | 1.038 | $(\zeta_{tZ c})^2$ |

Table 3.3: Next to leading order top pair cross section for the top-Z FCNC interactions with with a full leptonic decay.

| Anomalous coupling | Process | Cross section (pb) |
|------------------------|--|---|
| κ_{tZu}/Λ | $t\bar{t} \rightarrow (b\ell^+\nu)(\bar{u}\ell^+\ell^-)$ | $2.727008 \cdot 10^5 \left(\kappa_{tZu}/\Lambda\right)^2$ |
| | $t\bar{t} \rightarrow (\bar{b}\ell^-\bar{\nu})(u\ell^+\ell^-)$ | $2.727008 \cdot 10^5 \left(\kappa_{tZu}/\Lambda\right)^2$ |
| κ_{tZc}/Λ | $t\bar{t} \rightarrow (b\ell^+\nu)(\bar{c}\ell^+\ell^-)$ | $2.726257 \cdot 10^5 \left(\kappa_{tZc}/\Lambda\right)^2$ |
| | $t\bar{t} \rightarrow (\bar{b}\ell^-\bar{\nu})(c\ell^+\ell^-)$ | $2.726257 \cdot 10^5 \left(\kappa_{tZc}/\Lambda\right)^2$ |
| ζ_{tZu} | $t\bar{t} \rightarrow (b\ell^+\nu)(\bar{u}\ell^+\ell^-)$ | $2.827184 \left(\zeta_{tZu}\right)^2$ |
| | $t\bar{t} \rightarrow (\bar{b}\ell^-\bar{\nu})(u\ell^+\ell^-)$ | $2.827184 \left(\zeta_{tZu}\right)^2$ |
| ζ_{tZc} | $t\bar{t} \rightarrow (b\ell^+\nu)(\bar{c}\ell^+\ell^-)$ | $2.806801 \left(\zeta_{tZc}\right)^2$ |
| | $t\bar{t} \rightarrow (\bar{b}\ell^-\bar{\nu})(c\ell^+\ell^-)$ | $2.806801 \left(\zeta_{tZc}\right)^2$ |

796 quark is decaying in tZ. Therefore, single top and top pair processes must be made independently
 797 though this violates gauge invariance. In the official release of MadGraph5_aMC@NLO this is not
 798 allowed and the generator experts bypassed this by creating the single top process without
 799 the extra hard jet. Since cross section for tZ + 1 jet is relatively small, these contributions
 800 are neglected and the single top signal is generated without any extra jets, while top pair is
 801 generated up to two extra jets.

802 3.2.4 Generating SM background events

803 The SM tZq events were generated using the MadGraph5_aMC@NLO generator, interfaced with
 804 Pythia version 8.2 [115] for parton showering and hadronisation. The WZ+jets, tZ, tZq,
 805 and tW samples are produced using the MadGraph5_aMC@NLO(version 5.222) [117], which
 806 includes up to one hadronic jet at next to leading order (NLO) QCD accuracy. Other minor
 807 background (e.g. WW, ZZ, tWZ and tH) are simulated using different generators such as
 808 MadGraph [111], MadSpin [129] and JHU [125–128]. All events are interfaced to Pythia for
 809 parton shower and hadronisation.

NOTE: Add source

The complete list of SM samples is given in Table 3.4 , along with their cross sections. The cross sections without a reference are coming from the generator with which the sample has been made, for some of them the uncertainties are provided by the Generator Group . For each MC sample, the integrated luminosity that the sample represents is estimated as the number of simulated events divided by the cross section of the generated process. For processes generated with MadGraph5_aMC@NLO, the effective number of simulated events is used, taking into account positive and negative event weights. The correction factor for those events is defined as

$$C = \frac{\text{Nb. of pos. weights} + \text{Nb. of neg. weights}}{\text{Nb. of pos. weights} - \text{Nb. of neg. weights}} \times \text{mc baseweight} \quad (3.6)$$

Table 3.4: SM MC samples used in this analysis with their corresponding cross section and MadGraph5_aMC@NLO correction C when applicable. The generators used for each sample are indicated.

| Process | Generator | Cross section (pb) | C |
|--|----------------------------------|---|------|
| $WZ \rightarrow 3\ell\nu$ | MadGraph5_aMC@NLO+Pythia | 5.26 | 1.61 |
| tZq with $Z \rightarrow \ell^+\ell^-$ | MadGraph5_aMC@NLO+Pythia | 0.0758 | 3.77 |
| tqH with $H \rightarrow ZZ \rightarrow \ell^+\ell^-\ell^+\ell^-$ | JHU+Pythia | $8.80 \cdot 10^{-6}$ | - |
| $t\bar{t}W + \text{jets}$ with $W \rightarrow \ell\nu$ | MadGraph5_aMC@NLO+MadSpin+Pythia | 0.2043 ± 0.0020 | 1.94 |
| $t\bar{t}Z \rightarrow 2\ell + 2\nu + \text{other}$, with $m_{\ell\ell} > 10$ GeV | MadGraph5_aMC@NLO+Pythia | 0.2529 ± 0.0004 | 2.15 |
| $t\bar{t}H, \text{no } b\bar{b} \text{ decays}$ | POWHEG+Pythia | 0.2151 | - |
| $t\bar{t}H, b\bar{b} \text{ decays}$ | POWHEG+Pythia | 0.2934 | - |
| $WW \rightarrow 2\ell 2\nu$ | POWHEG+Pythia | 12.178 | - |
| $ZZ \rightarrow 4\ell$ | POWHEG+Pythia | 0.3366 | - |
| WZZ | MadGraph5_aMC@NLO+Pythia | 0.05565 | 1.14 |
| ZZZ | MadGraph5_aMC@NLO+Pythia | 0.01398 | 1.17 |
| single top quark tWZ , with $Z_\mu \rightarrow \ell^+\ell^-$ | MadGraph+Pythia | 0.001123 | - |
| single top quark t-channel \bar{t} | POWHEG+MadSpin+Pythia | $44.33^{+1.76}_{-1.49}$ | - |
| single top quark t-channel t | POWHEG+MadSpin+Pythia | $26.38^{+1.32}_{-1.18}$ | - |
| single top quark $t\bar{W}$ | POWHEG+Pythia | $35.85 \pm 0.90 \text{ (scale)} \pm 1.70 \text{ (PDF)}$ | - |
| single top quark tW | POWHEG+Pythia | $35.85 \pm 0.90 \text{ (scale)} \pm 1.70 \text{ (PDF)}$ | - |
| $t\bar{t}$ | POWHEG+Pythia | $831.76^{+19.77+35.06}_{-29.20-35.06}$ | - |
| $Z/\gamma^* + \text{jets}$, with $m_{\ell\ell} > 50$ GeV | MadGraph5_aMC@NLO+Pythia | $3 \times (1921.8 \pm 0.6 \pm 33.2)$ | 1.49 |
| $Z/\gamma^* + \text{jets}$, with $10 \text{ GeV} < m_{\ell\ell} < 50 \text{ GeV}$ | MadGraph+Pythia | 18610 | - |

810 3.3 Multivariate analysis techniques: Boosted Decision Trees

811 The need of processing large quantities of data and discriminating between events with largely
 812 similar experimental signatures makes multivariate statistical analysis (MVA) a largely used
 813 method in the physics community. Multivariate classification methods based on machine
 814 learning techniques are a fundamental ingredient to most analyses. The advantage of using
 815 a MVA classifier is that it can achieve a better discrimination power with respect to a simple
 816 cut and count analysis with poorly discriminating variables. These variables are referred to
 817 as weak variables and have similar distributions for signal and background samples. A risk of
 818 using MVA classifiers is overtraining. This happens when there are too many model parameters
 819 of an algorithm adjusted to too few data points. This leads to an increase in the classification
 820 performance over the objectively achievable one.

821 There are many software tools that exist for MVA. In this thesis the Tool for Multivariate
 822 Analysis (TMVA) [132] is used. This software is an open source project included into
 823 ROOT [133]. All multivariate techniques in TMVA belong to supervised learning algorithms. By
 824 training on events for which the outcome is known, a mapping function is determined that
 825 describes a classification or an approximation of the underlying behaviour defining the target
 826 value (regression).

827 In this thesis boosted decision trees (BDT) are employed for the classification of events as
 828 implemented in the TMVA framework [132]. This multivariate technique is based on a set of
 829 decision trees where each yields a binary output depending on the fact that an event is signal- or
 830 background-like. The advantage of such a multivariate technique is that several discriminating
 831 variables can be combined into a powerful one-dimensional discriminant D.

In Figure 3.4 a schematic view of a decision tree is shown. The starting point is the root node. Then a consecutive set of a total of i questions (nodes) regarding discriminating variables x_i are asked with only two possible answers per question (binary splits). The decision tree is constructed by training on a dataset for which the outcome is already provided, such as simulation dataset with signal and background processes (supervised learning). For each node a criterion $x_i > C_i$ is found by maximizing the separation gain between nodes

$$\text{separationgain} \approx \text{gain}(\text{parent}) - \text{gain}(\text{daughter, Signal}) - \text{gain}(\text{daughter, Background}), \quad (3.7)$$

with the gain computed using the Gini index

$$\text{gain}(\text{cell}) \approx p(1-p), \quad (3.8)$$

832 where p denotes the purity of a selection $x > C$. This is repeated until the maximum of nodes is
 833 reached and at the end of the sequence, the leaf nodes are labelled either signal S or background
 834 B, depending on the majority of events that end up on those nodes.

Different trees can be combined into a forest where the final output is determined by the majority vote of all trees, forming the sum of so-called weak learners into one strong learner. From one training collection, trees are derived by reweighting events, and combined into a single classifier as the weighted average of each individual decision tree. A method for making such forests is boosting a tree. In this method, misclassified events are weighted higher so

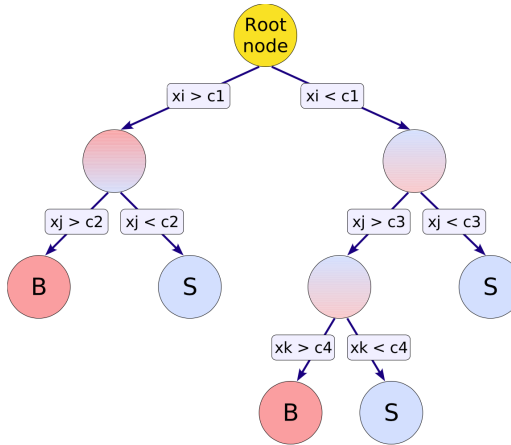


Figure 3.4: Schematic view of a decision tree. Figure taken from [132].

that future learner concentrate on these events. This has as advantage that the response of the decision trees are stabilised against fluctuations in the training sample which enhances the performance. Additionally, the trees can be kept very shallow, in this thesis the maximal number of nodes is set the three, which improves the robustness against overtraining. Examples of such boosting algorithms are Adaptive Boosting (AdaBoost) and Gradient Boosting [134]. In AdaBoost, each weight of the misclassified events are enhanced while reducing the weight of correctly classified events after each training such that future events learn those better

$$\alpha_{n+1} = \left(\frac{1 - \epsilon_n}{\epsilon_n} \right)^\beta, \quad (3.9)$$

where ϵ_n denotes the misclassification error of the current tree n and β is a learning rate. The weight w_i at node i is then equal to $w_i = \ln \alpha_i$. The final weight is the sum of all classifiers weighted by their errors. The learning rate is typically chosen to be $\beta \leq 0.5$ to allow more boosting steps. Gradient boosting has a similar approach and combines a gradient descent with boosting. Instead of fitting the base-learner to the reweighted data as in AdaBoost, it is fitted to the negative gradient vector of the loss function evaluated at the previous node. Misclassified events will result in a majority vote with large gradients of the loss function. Also for the Gradient boost, the learning rate is typically slow, this also known as shrinkage. In this thesis Gradient boost is used with a shrinkage of 0.2-0.3.

Additionally, the Gradient boost is used in combination with bagging, so-called stochastic gradient boosting. Bagging is a resampling technique draws a subset of events from the training data where the same event is allowed to be randomly picked several times from the parent sample. The tree is then trained on this subset and this is repeated many times. It is based on the assumption that sampling from a dataset that follows a distribution is the same as sampling from the distribution itself [135]. If one draws an event out of the parent sample, it is more likely to draw an event out of the phase space that has a high probability density, as the original dataset will have more events in the regions. Since the selected event is kept in the original sample, the parent sample stays unchanged so that randomly extracted samples have

853 the same parent distribution, albeit statistically fluctuated. Bagging smears over the statistical
 854 fluctuations in the training data, making it suitable for stabilising the response of the classifier
 855 and increasing the performance by eliminating overtraining. In stochastic gradient boosting the
 856 bagging resampling procedure uses random sub-samples of the training events for growing the
 857 trees.

858 The discriminating power of a BDT is assessed by analysing the receiver operating characteristic
 859 (ROC) curve. These curves show the background rejection over the signal efficiency of the
 860 remaining sample. By looking at the area under the curve with respect to random guessing
 861 (AUC), the best classifier can be identified. This follows the Neyman-Pearson lemma that
 862 the best ROC curve is given by the likelihood ratio $\mathcal{L}(x|Signal)/\mathcal{L}(x|Background)$ [135]. No
 863 discrimination power will result in an AUC of 0%, while 50% means fully separated event
 classes. In Figure 3.5 an example of ROC curve is shown.

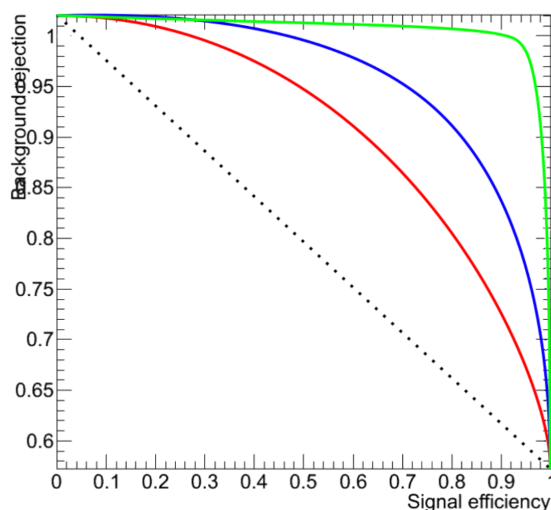


Figure 3.5: Example of ROC curves. In this example, the green method is better than the red one, which is better than the blue one. The dashed line represents a case where there is no separation. Figure taken from [136].

864

865 3.4 Statistical methodology

866 The search performed in the framework of this thesis requires the simultaneous analysis of data
 867 from different decay channels. The statistical methodology used for this search is developed by
 868 the ATLAS and CMS collaborations in the context of the LHC Higgs Combination group. The
 869 description of the methodology can be found in Refs. [137–140].
 870 The Higgs Combined Tool [141] is a RooStats [142] framework which runs different statistical
 871 methods. In this section, only the statistical tools necessary for the performed search are
 872 described. The results presented in this thesis are obtained using the asymptotic formulae [143].

873 In general the event yields of signal and background processes are denoted as s and b
 874 respectively. These represent event counts in multiple bins or unbinned probability density

functions. By use of simulation, predictions on both signal and background yields are made. These predictions are subject to multiple uncertainties that are accounted for by introducing nuisance parameters θ such that $s = s(\theta)$ and $b = b(\theta)$. In the following, the actual observed events are denoted as data or observation.

3.4.1 The absence of signal: limits

The absence of a signal is characterised in high energy physics by the Bayesian and modified classical frequentist statistical approaches. They allow to quantify the level of incompatibility of data with a signal hypothesis in terms of confidence levels (CL). The convention is to require a 95% CL for excluding a signal.

An analysis targeting a certain signal production mechanism can either set approximate model-independent limits on signal cross sections times branching ratio ($\sigma \times \mathcal{B}$) or on the signal cross section times branching ratio times detector acceptance ($\sigma \times \mathcal{B} \times \mathcal{A}$). In order to test various theories, the latter is not useful unless the acceptance \mathcal{A} is provided. However, many analysis are not able to present result in a form of limits on $\sigma \times \mathcal{B} (\times \mathcal{A})$, therefore an alternative is adopted to set limits in the signal strength modifier μ . The signal strength modifier is defined to equally change all the cross sections of all production mechanisms of the signal by the same scale.

In this thesis, the modified frequentist approach for confidence levels is used [144, 145]. The classical frequentist uses a test statistic q_μ based on the profile likelihood ratio to determine how signal- or background-like the data is. However, it does not allow nuisance parameters and is modified to incorporate these. First a likelihood $\mathcal{L}(\text{data} | \mu, \theta)$ is constructed as

$$\mathcal{L}(\text{data} | \mu, \theta) = \text{Poisson}(\text{data} | \mu s(\theta) + b(\theta)) p(\tilde{\theta} | \theta). \quad (3.10)$$

The probability density function (pdf) $p(\tilde{\theta} | \theta)$ describes all sources of uncertainty and is described in Section 3.4.2. The data in Equation 3.10 represents either the actual observation or pseudo-data to construct sampling distributions. For a binned likelihood, the Poisson probabilities to observe n_i events in bin i is given as

$$\text{Poisson}(\text{data} | \mu s(\theta) + b(\theta)) = \prod_i \frac{(\mu s_i(\theta) + b_i(\theta))^{n_i}}{n_i!} e^{-\mu s_i(\theta) - b_i(\theta)}. \quad (3.11)$$

At the LHC, the test statistic is defined as

$$q_\mu = -2 \ln \frac{\mathcal{L}(\text{data} | \mu, \hat{\theta}_\mu)}{\mathcal{L}(\text{data} | \hat{\mu}, \hat{\theta}_\mu)}, \quad (3.12)$$

where the likelihood is maximised in the numerator (maximum likelihood estimator, MLE) for a given μ and (pseudo) data at $\hat{\theta}_\mu$, while $\hat{\mu}$ combined with $\hat{\theta}$ defines the point for which the likelihood reaches its global maximum. The estimated signal strength modifier $\hat{\mu}$ can not become negative since a signal rate is positive defined by physics. Furthermore, an upper constraint on the MLE $\hat{\mu} \leq \mu$ is imposed to guarantee a one sided confidence interval. This has

as consequence that upward fluctuations of the data ($\hat{\mu} > \mu$) are not considered against the signal hypothesis of data with a signal with strength μ .

The criterion for excluding the signal at $1 - \alpha$ confidence level is the ratio of the probabilities to observe a value of the test statistic at least as large as the one observed in data q_μ^{obs} , under the signal plus background ($s + b$) and background only (b) hypothesis is defined as

$$\text{CL} = \frac{P(q_\mu \geq q_\mu^{\text{obs}} | \mu s + b)}{P(q_\mu \geq q_\mu^{\text{obs}} | b)} \leq \alpha. \quad (3.13)$$

These probabilities are defined as

$$\begin{aligned} p_\mu &= P(q_\mu \geq q_\mu^{\text{obs}} | \mu s + b) = \int_{q_\mu^{\text{obs}}}^{\infty} f(q_\mu | \mu, \theta_\mu^{\text{obs}}) dq_\mu, \\ 1 - p_b &= P(q_\mu \geq q_\mu^{\text{obs}} | b) = \int_{q_{\mu=0}^{\text{obs}}}^{\infty} f(q_\mu | \mu = 0, \theta_{\mu=0}^{\text{obs}}) dq_\mu, \end{aligned} \quad (3.14)$$

where p_μ and p_b are called the p-values associated to the two hypothesis, and $f(q_\mu | \mu, \theta_\mu^{\text{obs}})$ and $f(q_\mu | \mu = 0, \theta_{\mu=0}^{\text{obs}})$ are the pdfs of the signal plus background and background only hypothesis constructed from toy Monte Carlo pseudo data. These pdfs are shown in Figure 3.6 and are generated with nuisance parameters fixed to $\hat{\theta}_{\mu=0}^{\text{obs}}$ and $\hat{\theta}_\mu^{\text{obs}}$. These values of the nuisance parameters for the background only $\hat{\theta}_{\mu=0}^{\text{obs}}$ and signal plus background $\hat{\theta}_\mu^{\text{obs}}$ hypothesis that best describe the data are found by maximising the likelihood from Equation 3.10. The 95% CL level upper limit on μ is achieved by adjusting μ until $\text{CL} = 0.05$

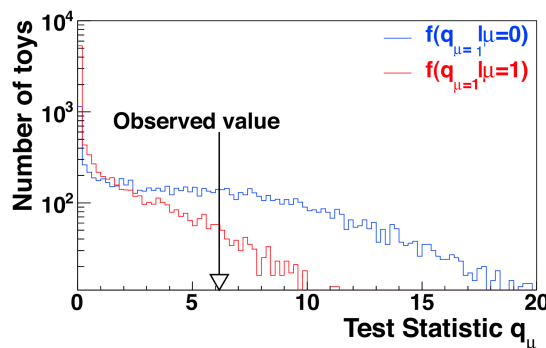


Figure 3.6: Test statistic distributions for pseudo data generated for the signal plus background ($\mu = 1$) and background only ($\mu = 0$) hypothesis. Figure taken from [140].

905

906 The expected median upper limit and the $\pm 1\sigma$ and $\pm 2\sigma$ bands for a hypothesis is generated
907 by a large set of pseudo data and calculate the CLs and the value of μ at 95% CL for each of
908 them. A cumulative probability distribution can be build by starting the integration from the

909 side corresponding to low event yields. The median expected value is where the cumulative
 910 distribution function crosses the 50% quantile. The $\pm 1\sigma$ (68%) and $\pm 2\sigma$ (95%) bands are
 911 defined by the crossings of the 16% and 84%, and 2.5% and 97.5% quantiles.

912 3.4.2 Adding sources of uncertainty

913 In this thesis, all sources of uncertainties are assumed to be either 100% correlated or uncor-
 914 related. Partially correlated uncertainties are broken down to subcomponents that fit those
 915 requirements, allowing to include all constraints in the likelihoods in a clean factorised form.

A systematic uncertainty pdf $p(\theta|\tilde{\theta})$ for the nuisance θ with nominal value $\tilde{\theta}$ is used. It reflects the degree of belief of what the true value of the θ is. In this thesis, the approach from the Higgs Combined Tool is used where the pdfs $p(\theta|\tilde{\theta})$ are re-interpret as posteriors of real or imaginary measurements $\tilde{\theta}$

$$p(\theta|\tilde{\theta}) \sim p(\tilde{\theta}|\theta) \pi_\theta(\theta), \quad (3.15)$$

916 where $\pi_\theta(\theta)$ is the hyper prior for the (imaginary) measurements. For the pdfs used by the
 917 Higgs Combine Tool (normal, log normal, gamma distribution), hyper priors can remain flat.
 918 This allows to use the pdf $p(\tilde{\theta}|\theta)$ to constrain the likelihood of the main measurement in a
 919 frequentist calculation. Additionally this allows to build a sampling distribution of the test
 920 statistic [140].

The statistical uncertainties on the Monte Carlo prediction in each bin are obtained following the Barlow-Beeston-light approach [146]. In this approach a single Gaussian constrained nuisance parameter is assigned to scale the sum of the process yields in each bin, constrained by the total uncertainty. This method has as advantage that it minimises the number of parameters required in the maximum likelihood fit. Considering n_{tot} events in a bin with background process i in the bin

$$n_{\text{tot}} = \sum_{i \in \text{bkg}} n_i, \quad (3.16)$$

the total uncertainty e_{tot} is given by

$$e_{\text{tot}} = \sqrt{\sum_{i \in \text{bkg}} e_i^2}, \quad (3.17)$$

921 with e_i the uncertainty on background i and is given by the sum of squares of weights used to
 922 fill the bins. The Gaussian constrained parameter x has then a nominal value of zero and scales
 923 the yield as $n_{\text{tot}} + x e_{\text{tot}}$.

924 Choices of systematic uncertainty density functions

For uncertainties that are unconstrained by a priori measurements that do not involve the data going into the statistical analysis, flat priors are used. When there are a priori measurements available such as those from control regions, one can use either a Gaussian pdf, a log-normal pdf, or a gamma distribution. The Gaussian pdf is suited for describing uncertainties on parameters

with both positive and negative values. This prior is however not suitable for positively defined observables such as cross sections, cut efficiencies, luminosity, etc. and is not used in this thesis. An alternative option is the log normal pdf which is used in the rest of this thesis

$$\rho(\theta) = \frac{1}{\sqrt{2\pi} \ln(\kappa)} \exp\left(-\frac{(\ln(\theta/\tilde{\theta}))^2}{2(\ln \kappa)^2}\right) \frac{1}{\theta}. \quad (3.18)$$

The parameter κ characterises the width of the log normal pdf. For example $\kappa = 1.10$ implies that the observable can be larger or smaller by a factor 1.10, both deviation having a chance of 16%. The gamma distribution is used for describing statistical uncertainties associated with a number of Monte Carlo events in simulation or a number of observed events in a data control sample. In this thesis, the gamma distribution is only used for the latter. The event rate in the signal region n is related to the number of events in the control region N as $n = \alpha N$. Ignoring the uncertainties on α , the predicted rate follows

$$\rho(n) = \frac{1}{\alpha} \frac{n/\alpha)^N}{N!} \exp(-n/\alpha). \quad (3.19)$$

925 The mapping between the posteriors $\rho(\theta|\tilde{\theta})$ and the auxiliary measurement pdfs $p(\tilde{\theta}|\theta)$ are
926 given in [140].

927 3.4.3 Asymptotic approximation of the CL method

928 In order to significantly reduce computing time, the Asymptotic CL method is used. This method
929 avoids an ensemble of toy Monte Carlo samples and instead replaces it by one representative
930 dataset, called Asimov dataset. This dataset is constructed such that all observed quantities are
931 set equal to their MLE values ($\hat{\theta}_{\text{Asimov}} = \theta_0$). More information about this procedure can be
932 found in Refs. [138].

933 3.4.4 Extracting the signal model parameters

From a scan of the profile likelihood ratio,

$$q(a) = -2 \ln \frac{\mathcal{L}(\text{obs} | s(a) + b, \hat{\theta}_a)}{\mathcal{L}(\text{obs} | s(\hat{a}) + b, \hat{\theta})}, \quad (3.20)$$

the signal model parameters are evaluated. The likelihood is maximised by the parameters \hat{a} and $\hat{\theta}$. The likelihood

$$\mathcal{L}_{\max} = \mathcal{L}(\text{obs} | s(\hat{a}) + b, \hat{\theta}) \quad (3.21)$$

934 is called the best-fit set.

935 The 68% and 95% CL on a given parameter of interest a_i is then evaluated from $q(a_i) = 1$ or
936 $q(a_i) = 3.84$ respectively, where all other unconstrained model parameters are treated in the
937 same way as the nuisance parameters [139].

Event reconstruction and identification

4

939 After the detector simulation described in [Section 3.2](#), the simulated data has the exact same
 940 format as the real collision data recorded at the CMS experiment. Therefore the same software
 941 can be used for the reconstruction of both simulation and real data. In [Section 4.1](#), the object
 942 reconstruction is explained. After reconstructing the objects, they are connected ([Section 4.2](#)) to
 943 physics objects need to be identified ([Section 4.3](#)) and corrected for pile up ([Section 4.4](#)). The
 944 objects used for physics analysis have extra requirements as shown in [Section 4.5](#). A summary
 945 of all the corrections applied to data and simulation is given in [Section 4.6](#).

946 4.1 Object Reconstruction

947 In [Figure 4.1](#), the particle interaction in a transverse slice of the CMS detector is shown. The
 948 particles enter first the tracker where charged particle trajectories, so-called tracks, and origins
 949 or vertices are reconstructed from signals (hits) in the sensitive layers. Charged particles get
 950 bent by the magnetic field making it able to measure the electric charges and momenta of
 951 charged particles. In the ECAL, the electron and photons are absorbed and the corresponding
 952 electromagnetic showers are detected as clusters of energy in adjacent cells. From this, the
 953 energy and the direction of the particles can be determined. The charged and neutral hadrons
 954 can initiate a hadronic shower in the ECAL that is fully absorbed in the HCAL. The clusters
 955 from these showers are also used to estimate the energy and direction. Muons and neutrino's
 956 pass through the calorimeters without little to no energy loss. The neutrino's escape the CMS
 957 detector undetected while muons produce hits in the muon detectors.

958 The traditional hadron colliders reconstruction is as follows. The reconstruction of isolated
 959 photons and electrons is primarily done by the ECAL, while the identification of muons is based
 960 on the muon detectors. Hadrons and photons form jets which are measured by the calorimeters
 961 without any contribution from the tracker or muon detectors. Jets can be tagged using the
 962 tracker as coming from hadronic τ decays or b hadronisation based on the properties of the
 963 relevant charged particle tracks. The missing transverse energy \vec{p}_T is defined as the vectorial
 964 sum of the undetectable particle transverse momenta, and can be reconstructed without any
 965 information from the tracker. The particle flow (PF) [[147](#)] reconstruction correlates the tracks
 966 and clusters from all detector layers with the identification of each final state particle, and

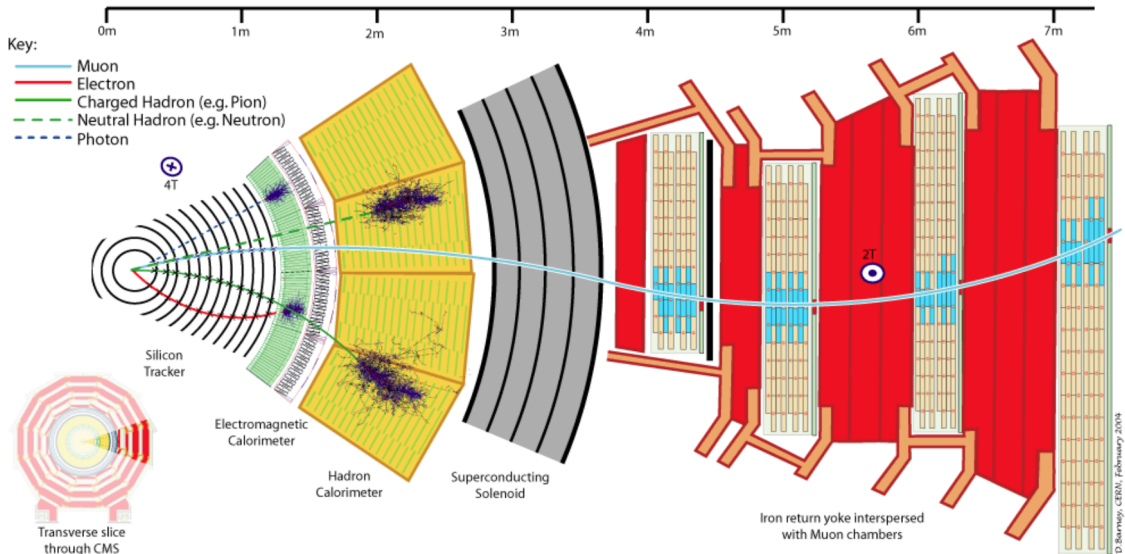


Figure 4.1: Cross-section of the CMS detector with all parts of the detector labelled. This sketch shows the specific particle interactions from a beam interaction reign to the muon detector. The muon and charged pion are positively charged, the electron is negatively charged. Figure taken from [147].

967 combines the corresponding measurements to reconstruct the properties. In the particle flow
 968 algorithm, the muon is identified by a track in the inner tracker connected to a track in the
 969 muon detector as described in Section 4.1.2. The electrons are identified by a track and an
 970 ECAL cluster, not connected to an HCAL cluster as described in Section 4.1.3. The ECAL and
 971 HCAL clusters without a track link identify the photons and neutral hadrons, while the addition
 972 of the tracker determines the energy and direction of a charged hadron.

973 Coarse-grained detectors can cause signals of different particles to merge and reduce the
 974 ability of identifying and reconstructing the particles. Therefore, particle flow identification
 975 requires sufficiently segmented subdetectors such that a global event description is possible.
 976 The CMS detector is built to meet to requirements of the particle flow reconstruction. It has
 977 an efficient and pure muon identification system, a hermetic HCAL with coarse segmentation,
 978 a higher segmented ECAL, a fine-grained tracker and a large magnetic field to separate the
 979 calorimeter deposits of charged and neutral particles in jets.

980 4.1.1 Charged particle tracks

981 An iterative tracking algorithm is responsible for the reconstruction of the tracks made by
 982 charged particles in the inner tracking system. Each iteration consists of four steps [68]: the
 983 track-seed generation, the pattern recognition algorithm, removal of track-hit ambiguities and
 984 a final track fit.

985 The seed generation is the first step. It consists of finding reconstructed hits that are usable
 986 for seeding the subsequent track-finding algorithm. They are identified from a group of at
 987 least three reconstructed hits in the tracker, or from a pair of hits while requiring the origin
 988 of the track segment to be compatible with the nominal beam-collision point. Since the pixel

989 has a higher granularity compared to the strip tracker, its seed generation efficiency is higher.
 990 The overall efficiency exceeds 99%. The second step of each iteration, the pattern recognition
 991 algorithm, uses the seeds as a starting point for a Kalman filter method [148, 149]. This
 992 algorithm extrapolates the seed trajectory towards the next tracker layer taking into account
 993 the magnetic field and multiple scattering effects. The track parameters are updated when a
 994 compatible hit in the next layer is found. This procedure continues until the outermost layer is
 995 reached. Since the Kalman filter method can result in multiple tracks associated to the same
 996 seed, or different tracks sharing the same hits, a removal of ambiguities is necessary. This
 997 ambiguity resolving is done by removing tracks that are sharing too many hits from the list
 998 of track candidates. The tracks with the highest number of hits or with the lowest χ^2 in the
 999 track fit is kept. The updated track parameters are then refitted using the Kalman filter method,
 1000 where all hits found in the pattern recognition step are taken into account. The fit is done twice
 1001 - once outwards from the beam line towards the calorimeters, and inwards from the outermost
 1002 track hit to the beam line -, improving the estimation of the track parameters.

1003 All hits that are unambiguously associated to the final track are removed from the list of
 1004 available hits. In order to associate the remaining hits, the procedure is repeated with looser
 1005 track reconstruction criteria. The use of the iterative track reconstruction procedure has a
 1006 high track finding efficiency, where the fake track reconstruction rate is negligible. For muons,
 1007 this results in a global track reconstruction efficiency exceeding 98%, and 75-98% for charged
 1008 hadrons.

1009 4.1.2 Following the Muon's Footsteps

1010 The muon reconstruction [150] has three subdivisions: local reconstruction, regional reconstruc-
 1011 tion and global reconstruction. The local reconstruction is performed on individual detector
 1012 elements such as strip and pixel hits in the inner tracking system, and muon hits and/or seg-
 1013 ments in the muon chambers. Independent tracks are reconstructed in the inner tracker - called
 1014 tracker tracks - and in the muon system, called standalone muon tracks. Based on these tracks,
 1015 two reconstructions are considered.

1016 The outside-in approach is referred to as Global Muon reconstruction. For each standalone
 1017 muon track, a inner tracker track is found by comparing the parameters of the two tracks prop-
 1018 agated onto a common surface. Combining the hits from the tracker track and the standalone
 1019 track, gives a fit via the Kalman filter technique [148, 149] for a global muon track.

1020 The second approach is an inside-out reconstruction, creating tracker muons. All candidate
 1021 tracker tracks with a $p_T > 0.5$ GeV and total momentum $p > 2.5$ GeV are extrapolated to the
 1022 muon system taking into account the magnetic field, the average expected energy losses, and
 1023 multiple Coulomb scattering in the detector material. The extrapolated track and the muon
 1024 segments are considered matched when the difference in the position in the x coordinates is
 1025 smaller than 3 cm, or when the ratio of this distance to its uncertainty is smaller than four. When
 1026 at least one muon segment - DT or CSC hits - matches the extrapolated track, the corresponding
 1027 tracker track is indicated as a tracker muon.

1028 For low transverse momenta ($p_T \lesssim 5$ GeV), the tracker muon reconstruction is more efficient
 1029 than the global muon approach. This is due to the fact that tracker muons only require a

1030 single muon segment in muon system, while the global muon approach requires typically
 1031 segments in at least two muon stations. These tracker muons are used for identifying muons
 1032 from the hadronisation of b or c quarks. The global muon approach typically improves the
 1033 tracker reconstruction for $p_T \gtrsim 200$ GeV. These are labelled isolated when in a cone of
 1034 $\Delta R = \sqrt{\Delta\phi^2 + \Delta\eta^2} = 0.3$ around the muon, the sum of the transverse momenta of additional
 1035 tracker tracks and energy deposits in the calorimeter is less than 10% of the muon's transverse
 1036 momentum.

1037 4.1.3 The path of the Electron

1038 The electrons in CMS radiate more than 70% of their energy in the inner track through
 1039 bremsstrahlung before reaching the ECAL. This has as consequence that the electron tracks are
 1040 increasingly curved in the magnetic field as a function of its flight distance. Standard tracking
 1041 algorithms are based on Kalman filtering which assume that the energy loss is Gaussian dis-
 1042 tributed, and are therefore not suitable to fit the electron tracks. A different filtering algorithm,
 1043 the Gaussian sum filter (GSF) [151] is used in the electron track reconstruction instead.

1044 In CMS, the electrons are reconstructed in two ways. The older ECAL based tracking is
 1045 developed to identify high energetic isolated electrons. This tracking algorithm starts from
 1046 ECAL clusters with a transverse energy above 4 GeV and extrapolates from these cluster the
 1047 position of the hits in the tracker. In order to account for bremsstrahlung, neighbouring clusters
 1048 in η and ϕ are grouped together into a supercluster from which then the direction is determined
 1049 to find the position of the particles in the tracker. This has as consequence that for electrons
 1050 or positrons in jets, energy deposits of surrounding particles will be entering the supercluster
 1051 leading to a wrong position of the electron/positron in the tracker. Another disadvantage of the
 1052 ECAL based tracking is that for low p_T electrons, the trajectories will be very curved and the
 1053 supercluster will not contain all of the energy deposit, leading to a higher misconstruction rate.

1054 The faults of the ECAL based tracking are lifted by adding a tracker based algorithm. This
 1055 algorithm uses all the tracks with a p_T higher than 2 GeV found with iterative tracking as
 1056 seeds. Iterative tracking uses the Kalman Filter algorithm several times with an average track
 1057 reconstruction efficiency but high purity. In contrary with a global combinatorial fit, the iterative
 1058 tracking accepts tracks with a small transverse momentum that are not leaving any energy
 1059 in the ECAL, and tracks from particles that only interact with the inner tracker layers. When
 1060 the electron or positron radiated a small amount of energy, the corresponding track can be
 1061 reconstructed across the whole tracker and safely propagated to the ECAL surface. When there is
 1062 a larger amount of energy radiated however, the pattern recognition might fail to accommodate
 1063 for the change in the electron momentum leading to a track reconstructed with a small number
 1064 of hits. The solution for this is a preselection based on the χ^2 and number of hits and the
 1065 selected tracks are fitted again with Gaussian-Sum-Filter which can accommodate substantial
 1066 energy losses across the trajectory.

1067 The electron seeds from the ECAL- and tracker-based procedures are merged into a unique
 1068 collection and are then refitted by using the summed Gaussian distributions as uncertainty per
 1069 hit in the track fit.

1070 The electron efficiency is measured in 8 TeV proton collision data to be better than 93%
 1071 for electrons with an ECAL supercluster energy of $E_T > 20$ GeV [152]. For electrons with an
 1072 $E_T > 25$ GeV in 13 TeV proton collision data, the efficiency is about 96%[153].

1073 4.1.4 Primary Vertex Reconstruction

1074 The primary vertex (PV) reconstruction should be able to measure the location of all proton
 1075 interaction vertices in each event: the signal vertex an all vertices from pile up events. It
 1076 consists of a vertex finding and a vertex fitting algorithm and happens in three steps. Tracks are
 1077 selected to be consistent with being produced promptly in the primary interaction by imposing
 1078 requirements on the track parameters [78]. By grouping reconstructed tracks according to the
 1079 z coordinate of their closest approach to the beam line, vertices for all interaction in the same
 1080 beam crossing are found, at CMS this is done by a deterministic annealing algorithm [154] based
 1081 on a statistical mechanics model. On top of this, a vertex fitting algorithm like the Adaptive
 1082 Vertex fitter [155], is performed. This creates the three-dimensional primary-vertex position.
 1083 With this fit, the contribution from long-lived hadron decays is reduced by down weighting the
 1084 tracks with a larger distance to the vertex. The primary vertex corresponding to the highest
 1085 sum of squared track transverse momenta is noted as the point of the main interaction. The
 1086 resolution on the primary vertex is about 14 μm in $r\phi$ and about 19 μm in the z direction for
 1087 primary vertices with the sum of the track $p_T > 100$ GeV for 2016 data taking.

1088 4.1.5 Calorimeter clusters

1089 The cluster algorithm in the calorimeter detects and measures the energy and direction of stable
 1090 neutral particles such as photons and neutral hadron. Additionally, it used to separate neutral
 1091 particles from charged hadron energy deposits, and reconstructs and identifies electrons and
 1092 their bremsstrahlung photons. Furthermore, the cluster algorithm contributes to the energy
 1093 measurements of charged hadrons that don't have accurate tracks parameters, e.g. for low
 1094 quality and high transverse momentum tracks. The clustering is performed separately in each
 1095 subdetector: ECAL barrel and endcaps, HCAL barrel and end caps, and the two preshower
 1096 layers. The HF has no clustering algorithm since the electromagnetic or hadronic components
 1097 give rise to an HF EM or HF HAD cluster.

1098 The clustering algorithm consist of different steps. First seeds are identified when cells have
 1099 an energy larger than the seeding threshold and larger than their neighbouring cells. Then
 1100 topological clusters are made by accumulating cells that share at least a corner with a cell
 1101 already in the cluster and an energy above a cell threshold set to twice the noise level. The third
 1102 step is a expectation maximization algorithm that reconstructs the cluster [147]. This algorithm
 1103 assumes that the energy deposits are Gaussian distributed and is an iterative algorithm with
 1104 two steps at each iteration. The first step calculates the expected fraction of the energy, while
 1105 the second step performs a maximum likelihood fit. The positions and energies of the Gaussian
 1106 functions are then taken as cluster parameters.

1107 The calorimeter clusters are used for reconstructing photons and neutral hadrons. The clusters
 1108 that are not in the vicinity of the extrapolated charged tracks are easily identified as neutral
 1109 hadrons or photons. For the energy deposits that overlap with charged hadrons however, the
 1110 neutral particle energy deposit can only be detected as an excess over the charged particle

deposit. For this reason, a good calibration of the electromagnetic and hadronic calorimeter is vital.

The ECAL calibration is performed before the hadron cluster calibration or particle identification. For run 1, the ECAL response to electrons and photons as well as the cell-to-cell relative calibration is determined with test beam data, radio active sources, and cosmic ray measurements. For run 2, the collision data collected at 7 and 8 TeV was used to refine the calibration. The effect of the thresholds in the clustering algorithm are estimated from simulated single photons with energies varying from 0.25 to 100 GeV. The photons used for the calibration should not have a conversion prior to their entrance to ensure the calibration of single clusters. In all ECAL regions and for all energies, the calibrated photon energies agree with the true photon energies within 1%.

In contrary to the photons, the hadrons deposit in general energy in both ECAL and HCAL. Since the calorimeter response in the HCAL depends on the fraction of shower energy deposited in the ECAL, the ECAL and HCAL cluster energies are recalibrated together to get an estimate of the true hadron energy. Since the calibration is done for hadrons, single neutral hadrons such as K_L^0 are used for determining the calibration constants. The hadrons interaction with the tracker material are rejected for the calibration purposes. This calibration is checked with isolated charged hadron selected from early data recorded at $\sqrt{s} = 0.9, 2.2$ and 7 TeV.

4.2 Putting the pieces together

A link algorithm connects the several PF elements from the various CMS subdetectors. It tests any pair of elements in an event and is restricted to considering nearest neighbours in the $\eta\phi$ -plane. The quality of the link is determined via the distance between the two elements and PF blocks of elements are formed from elements with a direct link or indirect link through common elements.

The link between a central tracker track and a calorimeter clusters is made by extrapolating the tracker track to the two layers of the preshower, the ECAL, and the HCAL. If this extrapolated position is within the cluster area, the two are linked. When there are several ECAL or HCAL clusters for the same track, the link with the smallest distance is kept. A dedicated cluster algorithm accounts for the energy of the photons emitted through bremsstrahlung at for photons that have converted to an electron-positron pair.

The ECAL to HCAL cluster and ECAL to preshower cluster links are established when the cluster position in the more granular calorimeter, ECAL or preshower, is in accordance with the cluster envelope of the less granular calorimeter, HCAL or ECAL. When there are multiple HCAL clusters linked to the same ECAL cluster, the link with the smallest distance is kept. This is also true for multiple ECAL clusters with the same preshower clusters. The ECAL supercluster is linked with the ECAL cluster when they share at least one ECAL cell.

Nuclear interactions in the tracker can lead to kinks in hadron trajectories as well as the production of secondary particles. This leads to charged particle tracks linked together via a common displaced vertex. The displaced vertices considered should have at least three tracks, with at most one incoming track, and the invariant mass of the outgoing tracks should exceed 0.2 GeV. The link between a track and the muon detectors is done via local, regional, and global reconstruction as explained in [Section 4.1.2](#).

1153 4.3 Particle flow identification

1154 The identification and reconstruction follows a particular order in each PF block. After each
 1155 identification and reconstruction the corresponding PF elements (tracks and clusters) are
 1156 removed from the PF block. The muons are the first to be identified and reconstructed. These
 1157 are reconstructed if their momenta are compatible with corresponding track only momenta. Then
 1158 the electron and its corresponding brehmstrahung photons, are identified and reconstructed by
 1159 using of the GSF tracking. At the same time, the energetic and isolated photons are identified as
 1160 well. The remaining elements in the PF block are subjected to a cross identification of charged
 1161 hadrons, neutral hadrons, and photons that arise from parton fragmentation, hadronisation,
 1162 and decays in jets. The charged hadron candidate is made from the remaining candidates that
 1163 have a charged particle track associated with them. Then the charged particle energy fraction
 1164 is subtracted from the calibrated energy of the linked calorimeter clusters and the remaining
 1165 energy is assigned to the neutral energy. Depending on the excess of neutral energy in the ECAL
 1166 and HCAL clusters, a photon or a neutral hadron is assigned respectively. The pseudorapidity
 1167 range of the inner tracker limits the information on the particles charge to $|\eta| < 2.4$. Outside
 1168 this range a simplified identification is done for hadronic and electromagnetic candidates only.

1169 4.3.1 Muons

1170 A set of selection requirements based on the global and tracker muon properties is responsible
 1171 for muon identification. The muons are considered isolated when the additional inner tracks
 1172 and calorimeter energy deposits within a distance to the muon direction in the $\eta\phi$ -plane is
 1173 smaller than 0.3. The muons coming from charged hadron decays or heavy flavour decays need
 1174 more stringent criteria. This due to the fact that charged hadrons can be misidentified as muons
 1175 because of e.g. punch-through, or muons can be seen as charged hadrons, and will absorb the
 1176 energy deposits of nearby particles.

1177 4.3.2 Electrons and isolated photons

1178 The electrons and photons are reconstructed together as discussed before. An electron candidate
 1179 seeded from a GSF track is considered an electron when the linked ECAL cluster is not linked
 1180 to three or more additional tracks. The photon seeds are ECAL superclusters with transverse
 1181 energies above 10 GeV that have no links with a GSF track. After associating photons from
 1182 brehmstrahung with the associated electrons, the remaining energy is associated to the photons
 1183 and the photon direction is taken to be that of the supercluster. The electron direction is
 1184 chosen to be that of the GSF track and its energy is a combination of the ECAL energy with
 1185 the momentum of the GSF track. Photons are retained if they are isolated, while electrons
 1186 should satisfy additional criteria based on a multivariate analysis for isolated and non-isolated
 1187 electrons.

1188 4.3.3 Hadrons and non-isolated photons

1189 After muon, electron and isolated photon identification, the remaining particles are hadrons
 1190 from jet fragmentation and hadronisation. These can show up as charged hadrons (e.g. π^\pm ,
 1191 K^\pm , or protons), neutral hadrons (e.g. K_L^0 or neutrons), non isolated photons (e.g. from π^0
 1192 decays), and additional muons from early decays of charged hadrons.

1193 The photons and neutral hadrons are assigned to calorimeter clusters without any link to
 1194 tracks. When the calorimeter clusters between the ECAL and HCAL are linked, the clusters are
 1195 assumed to arise from the same hadron shower. If their is not such a link, HCAL clusters are
 1196 assigned to neutral hadrons, while the ECAL clusters are assigned to photons based on the fact
 1197 that neutral hadrons leave only 3% of their energy in the ECAL. The HCAL clusters linked with
 1198 tracks, that are not linked with other HCAL clusters, are assigned to charged hadrons. These
 1199 tracks are then linked with remaining ECAL clusters.

1200 Hadron interactions can result in the creation of extra particles originating from a secondary
 1201 vertex. These extra particles are identified by having a common secondary vertex and replaced
 1202 in the PF list as one single primary charged hadron.

1203 4.3.4 Post processing

1204 After identification and reconstruction of all particles as described above. An artificial large
 1205 missing transverse momentum \vec{p}_T can be reconstructed. The cause of the \vec{p}_T is mostly
 1206 misidentified or misreconstructed high- p_T muons originating from cosmic rays, misconstruction
 1207 of the muon's momentum, or punch-through charged hadrons. A post processing step is applied
 1208 to solve this \vec{p}_T . Events with genuine large \vec{p}_T due to the presence of neutrino's are unaffected
 1209 by this post processing.

1210 4.4 Pile up mitigation and luminosity measurement

1211 The particle flow algorithm is design without taking pile up into account. For the 8 TeV dataset,
 1212 an average of about 21 pile up interactions happen per bunch cross section. For the dataset
 1213 taken at 13 TeV, the number of pile up interactions increases to about 27 interactions per
 1214 bunch crossing. These interactions are spread around the beam axis around the centre of the
 1215 CMS coordinate system and follow a normal distribution with a standard deviation of about
 1216 5 cm [147]. The number of pile up interactions is estimated from the number of interaction
 1217 vertices reconstructed from charged particle tracks, or from the instantaneous luminosity of the
 1218 given bunch crossing with dedicated detectors and the inelastic proton-proton crossing.

The luminosity of the CMS interaction point is estimated from measuring certain process rates with luminometers such as the pixel detector, HF calorimeter, and the pixel luminosity telescope [156]. The instantaneous luminosity from recorded process rate R is then determined as

$$Ldt = \frac{Rdt}{\sigma_{fid}}, \quad (4.1)$$

1219 where $\sigma_{fid} = \sigma \times A$ corresponds to the fiducial cross section recorded in the luminometer
 1220 acceptance A which is determined using van der Meer scans [157]. The overall uncertainty on
 1221 the luminosity measurement is estimated to be 2.5%.

1222 The luminosity is used to infer to number of pile up interactions in data, which can be used
 1223 to corrected the predefined pile up interactions in simulation. The average number of pile up
 1224 interactions in data is estimated per luminosity section by multiplying the luminosity times

1225 the total inelastic cross section. Then an event weight can be derived from the ratio of the
 1226 distributions of pile up interactions in data and simulation. For 13 TeV collisions, the inelastic
 1227 cross section is measured to be 71.3 ± 3.5 mb [157]. However a better agreement in data and
 1228 simulation for the pile up sensitive variables, such as the number of primary vertices, is found
 1229 with a lower cross section of 69 mb.

1230 The pile up vertices are separated from the primary vertex by requiring that the primary vertex
 1231 is the vertex with the highest quadratic sum of the transverse momenta of the corresponding
 1232 tracks. The charged hadrons coming from these pile up vertices are identified via their tracks
 1233 and are removed from the list of reconstructed particles to be used for physics analysis. This
 1234 method is the so-called pile up charged hadron subtraction and denoted as CHS [158]. For the
 1235 reconstructed particles outside the tracker acceptance as well as photons and neutral hadrons,
 1236 the CHS method doesn't work. Therefore, the transverse density from pile up interactions
 1237 is estimated using jet clustering techniques and their effect is subtracted from the particles
 1238 transverse momenta. Additionally, the pile up contribution can be estimated locally as described
 1239 for the muons and electrons described in [Section 4.5.1](#) and [Section 4.5.2](#).

1240 4.5 Physics object reconstruction and identification

1241 The particle flow objects are used for building physics objects that are used for analysis. These
 1242 objects are jets, muons, electrons, photons, taus and missing transverse momentum \vec{p}_T . They
 1243 are used to compute other quantities such as particle isolation and have extra requirements
 1244 that are analysis dependent. In the following section, only the physics objects used throughout
 1245 this thesis are discussed.

1246 4.5.1 Muons

1247 The muon candidates used for analysis in this thesis correspond to the tight working point (WP).
 1248 The tight working point yields the most genuine muons and rejects falsely reconstructed ones.
 1249 Detailed reports on the performance can be found in [159].

1250 In order to reject objects wrongly reconstructed as muons from hadron showers that reach the
 1251 muon system (punch-throughs), the global muon fit is required to include at least one valid
 1252 hit in the muon chambers and for which at least two muon segments in two muon stations
 1253 is present. Additionally, the muon tracks should have a global fit yielding a goodness-of-fit of
 1254 $\chi^2/\text{ndof} < 10$. The decay of muons in flight is suppressed by requiring at least one pixel hit in
 1255 the muon track. Furthermore, a minimum of five hits in the tracker is required. Cosmic muons
 1256 and muons originating from pile up interactions are rejected by constricting the distance of
 1257 the muon with respect to the primary vertex by putting limits on $d_{x,y} < 2$ mm and $d_z < 5$ mm.
 1258 Also muons according to the loose muon working point will be used in the thesis. These are
 1259 either global muons or tracker muons reconstructed from the particle flow muon object. In
 1260 [Figure 4.2](#), the muon efficiencies for data and simulation is presented. These efficiencies are
 1261 estimated from tag-and-probe methods that select $Z \rightarrow \mu^- \mu^+$ and tag one muon that passes
 1262 the identification criteria. The other muon is used as probe and one measures how many times
 1263 it passes the identification criteria to get the efficiency. Overall, the efficiency is about 95-100%,
 1264 with two drops due to the crack between the wheels of the DT system. The differences between

1265 data and simulation are corrected by applying p_T - and η -dependent scale factors ($\epsilon_{\text{data}}/\epsilon_{\text{MC}}$)
 1266 to simulated events. In Table 4.1, the muon requirements for the muons used throughout this
 thesis are summarised.

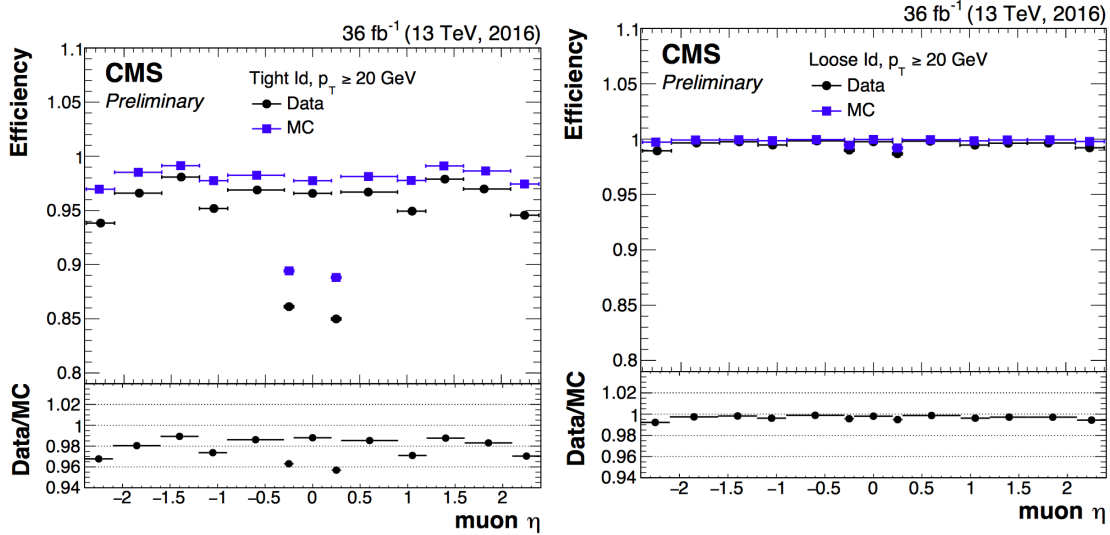


Figure 4.2: Comparison of the muon tight ID (left) and loose ID (right) efficiencies in data and simulation as a function of the pseudorapidity of the muon using the full 2016 dataset. Figure taken from [159].

1267

In addition to the identification criteria, the muons are required to be spatially isolated from EM and hadronic activity. The lepton isolation is defined as estimating the total transverse energy of the particles emitted around the direction of the lepton by defining a cone of radius ΔR in $\eta\phi$ plane around the lepton direction. Then a summed energy is calculated from the charged hadrons (CH), neutral hadrons (NH), photons (γ), excluding the lepton itself. This sum is then corrected to remove the energy coming from pile up interactions. The relative isolation for muons \mathcal{I}_μ is defined as [147]:

$$\mathcal{I}_\mu = \frac{\sum p_T(\text{CH}) + \max(0, \sum E_T(\text{NH}), \sum E_T(\gamma) - 0.5 \times \sum E_T(\text{CH}))}{p_T(\mu)}, \quad (4.2)$$

1268 where a cone of $\Delta R = 0.4$ is adopted and the pile up mitigation is based on the $\Delta\beta$ correction.
 1269 The $\Delta\beta$ correction estimates the pile up energy as half of the contribution coming from charged
 1270 hadrons. For tight ID muons, this relative isolation should $\mathcal{I}_\mu < 0.15$, while for loose muons
 1271 this should be $\mathcal{I}_\mu < 0.25$. In Figure 4.3, the isolation efficiencies as a function of the pseudo
 1272 rapidities using the tag and probe method are shown for the tight muon ID. The efficiencies are
 1273 85-100% with a decline for low- p_T muons since they are most likely coming from hadronic
 1274 or heavy flavour decays. The differences between data and simulation are accounted for by
 1275 applying η - and p_T -dependent scale factors on the simulation.

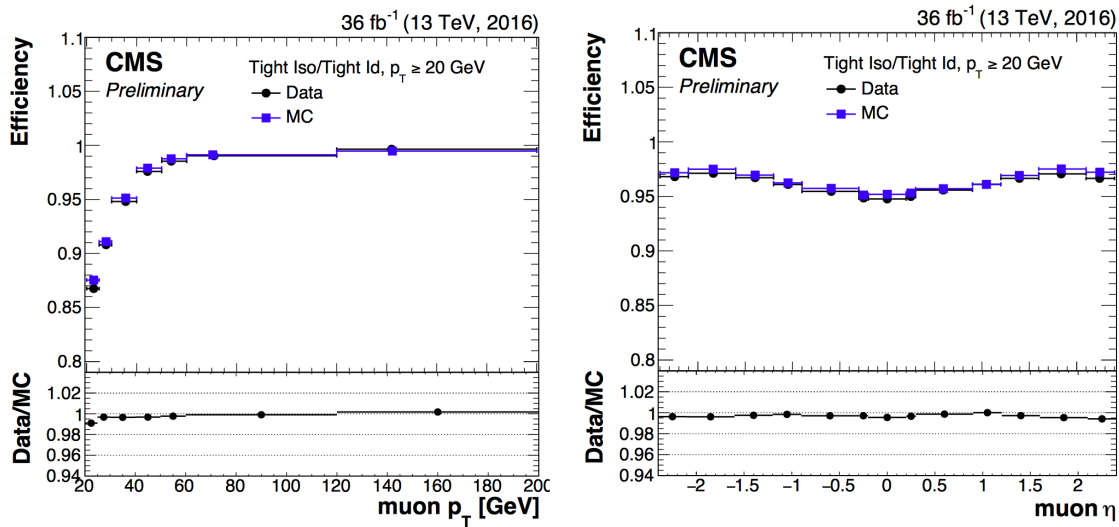


Figure 4.3: Comparison of the muon tight isolation requirement with the muon tight ID efficiencies in data and simulation as a function of the transverse momentum (left) or pseudorapidity (right) of the muon using the full 2016 dataset. Figure taken from [159].

Table 4.1: Muon requirements for the tight and loose working points, used throughout this thesis.

| Property | Loose Muons | Tight Muons |
|--|------------------|-------------------------|
| Global muon or Tracker Muon | One or the other | Both |
| Particle Flow muon | Y | Y |
| χ^2/ndof of global muon track fit | N/A | < 10 |
| Nb. of hit muon chambers | N/A | > 0 |
| Nb. of muon stations contained in the segment | N/A | > 1 |
| Size of the transverse impact parameter of the track wrt. to the PV | N/A | $d_{xy} < 2 \text{ mm}$ |
| Longitudinal distance wrt. the PV | N/A | $d_z < 5 \text{ mm}$ |
| Nb. of pixel hits | N/A | > 0 |
| Nb. of tracker layers with hits | N/A | > 5 |
| Relative Isolation | < 0.25 | < 0.15 |

1276 **4.5.2 Electrons**

1277 The electrons candidates used correspond to the tight and veto working points. The study of
 1278 the electron reconstruction and identification performance can be found in [153].

1279 Starting from an electron PF candidate with a GSF track that is outside the barrel-endcap
 1280 transition region ($1.4443 < |\eta| < 1.5660$), several requirements are set. The electrons from
 1281 photon conversions are dismissed by requiring the electron track to have not have more than one
 1282 (two or three) missing hit in the innermost layer for the tight (veto) working point. Additionally,
 1283 a photon conversion veto is applied by testing if a pair of electron tracks is originating from a
 1284 common displaced vertex. For the 8 TeV datasets more refined cuts are placed on the electron
 1285 object using a multivariate analysis. For the 13 TeV dataset this is replaced with more refined
 1286 cuts on the shower shape variables such as the difference in η or ϕ between the energy weighted
 1287 supercluster position in the ECAL and the track direction in at the innermost tracker position
 1288 ($\Delta\eta_{in}$, $\Delta\phi_{in}$), and the ECAL crystal based shower covariance in the η direction ($\sigma_{\eta\eta}$). These
 1289 cuts also include energy related variables such as the absolute difference between the inverse
 1290 electron energy measured in the ECAL and the inverse momentum measured in the tracker
 1291 ($|1/E - 1/p|$), and the ratio of the energy measured in the HCAL and ECAL (H/E). Unlike the
 1292 muon case, the identification criteria also contain requirements on the isolation of the electrons.

Similar to the muons, the electron relative isolation is determined from the sum of the particles in a cone around the electron itself. The cone radius used for electrons is $\Delta R = 0.3$ and a ρ correction for pile up mitigation is applied. For this correction, the expected pile up energy inside the isolation cone is estimated from the median density energy per area of pile up contamination (ρ), computed event by event, and the effective area ($A_{eff.}$) [147]. This effective area is estimated from simulation and denotes the expected amount of neutral energy from pile up interactions per ρ within the isolation cone as a function of the pseudo rapidity of the associated ECAL superclusters Table 4.2 shows the values used for 13 TeV data. The relative electron isolation \mathcal{I}_e is calculated as

$$\mathcal{I}_e = \frac{\sum p_T(CH) + \max(0., \sum E_T(NH), \sum E_T(\gamma) - \rho \times A_{eff.})}{p_T(e)}. \quad (4.3)$$

Table 4.2: The effective areas $A_{eff.}$ used for the electron relative isolation [160].

| η region | $A_{eff.}$ |
|-------------------------|------------|
| $0 < \eta < 0.1752$ | 0.1703 |
| $1.0 < \eta < 0.1479$ | 0.1715 |
| $1.479 < \eta < 2.0$ | 0.1213 |
| $2.0 < \eta < 2.2$ | 0.1230 |
| $2.2 < \eta < 2.3$ | 0.1635 |
| $2.3 < \eta < 2.4$ | 0.1937 |
| $2.4 < \eta < 2.5$ | 0.2393 |

1293

1294 The efficiency of electron identification is estimated from $Z \rightarrow e^- e^+$ events via the tag-and-
 1295 probe method and is shown in Figure 4.4 for the tight working point. The efficiencies reach

1296 95 – 100%. The difference between data and simulation are corrected by dedicated p_T - and η dependent scale factors as well.

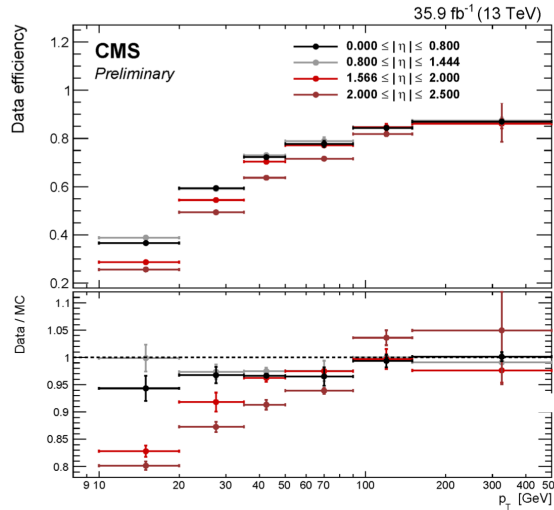


Figure 4.4: Electron identification efficiency as function of the electron transverse momentum from the full 2016 dataset. Figure taken from [153].

1297

Table 4.3: Electron requirements used in this analysis. The requirements are set in the barrel ($|\eta_{supercluster}| \leq 1.479$) and the end caps ($|\eta_{supercluster}| > 1.479$).

| Properties | $ \eta_{supercluster} \leq 1.479$ | | $ \eta_{supercluster} > 1.479$ | |
|-----------------------------|------------------------------------|-----------------------------|---------------------------------|-----------------------------|
| | Veto electron | Tight electron | Veto electron | Tight electron |
| $\sigma_{\eta\eta}$ | < 0.0115 | < 0.00998 | < 0.037 | < 0.0292 |
| $ \Delta\eta_{inl} $ | < 0.00749 | < 0.00308 | < 0.00895 | < 0.00605 |
| $ \Delta\phi_{in} $ | < 0.228 | < 0.0816 | < 0.213 | < 0.0394 |
| H/E | < 0.356 | < 0.0414 | < 0.211 | < 0.0641 |
| relative isolation | < 0.175 | < 0.0588 | < 0.159 | < 0.0571 |
| $ 1/E - 1/p $ | $< 0.299 \text{ GeV}^{-1}$ | $< 0.0129 \text{ GeV}^{-1}$ | $< 0.15 \text{ GeV}^{-1}$ | $< 0.0129 \text{ GeV}^{-1}$ |
| expected missing inner hits | ≤ 2 | ≤ 1 | ≤ 3 | ≤ 1 |
| pass conversion veto | Y | Y | Y | Y |

1298 **4.5.3 Jets**

Jets are reconstructed from all reconstructed particles without the charged hadrons associated to pile up vertices (PF+CHS jets). The clustering is done via the anti- k_T algorithm [161] with a radius parameter for the cone size of the resulting jet of $R = 0.5$ for 8 TeV data and $R = 0.4$ for the more boosted 13 TeV dataset. The initial step of the anti- k_T algorithm considers all candidates as protojets and starts to calculate the distances for protojets i and j as

$$d_{ij} = \min\left(\frac{1}{p_{T,i}^2}, \frac{1}{p_{T,j}^2}\right),$$

$$d_i = \frac{1}{p_{T,i}^2}. \quad (4.4)$$

1299 For each iteration the two distances are calculated. When $d_{ij} < d_i$, the two protojets are merged
 1300 and their four momentum is summed. If d_i is the smallest distance, the protojet is renamed
 1301 as final jet and ignored in the subsequent steps. More information about the jet algorithm
 1302 performance can be found in [162].

1303 The jets used for the analysis discussed in this thesis uses the loose identification working point
 1304 given. The criteria on the constituents of the jets are given in Table 4.4. These requirements
 1305 find their origin on the assumption that a proper jet originating from the hadronisation of a
 1306 quark or gluon consists of multiple PF particles and types. The jet should consist of more than
 1307 one constituent and the neutral hadron fraction and neutral EM energy fractions should be less
 1308 than 99%. For the jets within the tracker acceptance ($|\eta| < 2.4$), at least one constituent has to
 1309 be a charged hadron resulting in a charged hadron energy fraction above 0%. Additionally the
 1310 charged EM energy fraction should be less than 99%. On top of these requirements, objects
 1311 that are labelled as jets and found in vicinity of any isolated lepton, $\Delta R < 0.3$, are removed
 1312 from the jet collection in that event.

Table 4.4: Jet criteria used throughout the thesis. The last three requirements are only for jets within the tracker acceptance.

| Properties | Loose Jet ID |
|-------------------------|--------------|
| Neutral hadron fraction | < 0.99 |
| Neutral EM fraction | < 0.99 |
| Number of constituents | > 1 |
| Charged hadron fraction | > 0 |
| Charged multiplicity | > 0 |
| Charged EM fraction | < 0.99 |

1313 The energy of the reconstructed jets deviate from the energies of the corresponding jets
 1314 clustered from the hadronisation products of true partons from simulations due to non linear
 1315 subdetector response and efficiencies. The jet energy corrections (JEC) calibrate the jets
 1316 in order to have the correct energy scale and resolution. Jet energy scale corrections (JES)
 1317 are determined as a function of pseudorapidity and the transverse momentum from data and
 1318 simulated events by combining several channels and methods. This is extensively described

in [163]. These corrections account for the effects of pile up, the uniformity of the detector response, and residual data-simulation jet energy scale differences. Furthermore, the jet energy resolution (JER) is measured in data and simulation as function of pile up, jet size and jet flavour. A detailed understanding of both the energy scale and the transverse momentum resolution of the jets is crucial for many physics analysis, and these are commonly the main source of systematic uncertainty. The performance of the jet energy corrections for the 13 TeV dataset can be found in [164].

The JEC are factorised and subsequently correct for the offset energy due to pile up, the detector response to hadrons, and residual differences between data and simulation as a function of the jet pseudorapidity and transverse momentum. The consecutive steps of JEC are shown in Figure 4.5. The off set corrections remove the dependence of the jet energy response of

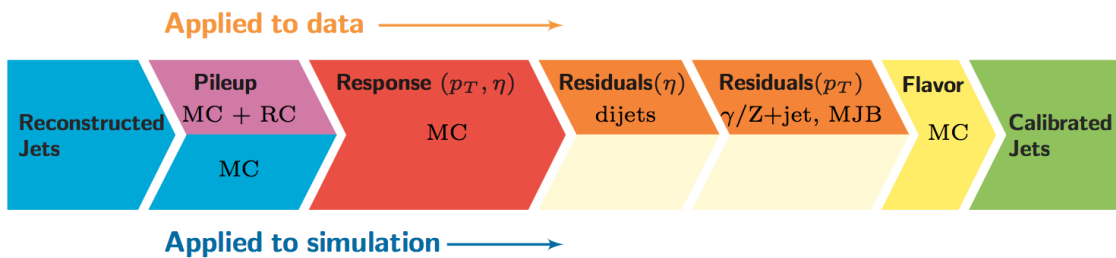


Figure 4.5: The sequence of the JEC for data and simulations. The corrections marked with MC are derived from simulation studies, while RC stands for random cone, and MJB for the analysis of multi-jet events. Figure taken from [163].

additional pile up activity. It is based on the jet area method, which uses the effective area of the jets multiplied by the average density in the event to calculate the offset energy to be subtracted of the jets. The correction factors are derived by comparing the jet response with and without pile up events overlaid. The residual differences between data and detector simulation are determined using the random cone method (RC). For this method, many jets are reconstructed in each event by clustering particles through placing random cones. This provides a mapping of the $\eta\phi$ -space and the average p_T of those jets gives the average energy offset due to pile up [163]. The next level of corrections have as goal to have an uniform energy response independent of the transverse momentum or pseudorapidity of the jet. These corrections are determined from simulated events by matching the reconstructed to true particle jets and comparing their momenta. The residual corrections between data and simulation are determined by comparing the transverse momentum balance in various types of events (multi-jet, Z + jets, and γ + jets), using a reference jet in the barrel region. The jet flavour corrections are optional and not used for this thesis. More information on the jet flavour corrections can be found in [163]. For jets with a transverse momentum above 30 GeV, the uncertainties from the various corrections are 3-5% for the 13 TeV dataset [164].

After applying JEC, the transverse momentum resolution of the jet is extracted from data and simulated events. There are two methods used to rescale the reconstructed four momentum chosen based on whether or not the simulated jet can be matched to a true jet in simulation.

The factors are defined as

$$c_{\text{matched}} = 1 + \frac{p_T^{\text{reco.}} - p_T^{\text{true}}}{p_T^{\text{reco.}}} (s_{\text{JER}} - 1),$$

$$c_{\text{unmatched}} = 1 + N(0, \sigma_{\text{JER}}) \sqrt{\max(s_{\text{JER}}^2 - 1, 0)},$$
(4.5)

where $N(0, \sigma_{\text{JER}})$ denotes a sample value from a normal distribution centred at zero with standard deviation the relative resolution in simulation σ_{JER} , and s_{JER} the η -dependent resolution scale factors. These scale factors are derived from data from di-jet or $\gamma + \text{jets}$ events and analysing the p_T balance. The resolution scale factors (data/simulation) are found to be 1.1-1.2 except for the transition regions around $|\eta| = 3$ and $|\eta| = 1.4$ [164] and given in Table 4.5.

Table 4.5: Jet energy scale factors in bins of η with uncertainty

| $ \eta $ | SF | Uncertainty (\pm) |
|----------|-------|-----------------------|
| 0-0.5 | 1.109 | 0.008 |
| 0.5-0.8 | 1.138 | 0.013 |
| 0.8-1.1 | 1.114 | 0.013 |
| 1.1-1.3 | 1.123 | 0.024 |
| 1.3-1.7 | 1.084 | 0.011 |
| 1.7-1.9 | 1.082 | 0.035 |
| 1.9-2.1 | 1.140 | 0.047 |
| 2.1-2.3 | 1.067 | 0.053 |
| 2.3-2.5 | 1.177 | 0.041 |

1351

4.5.4 Jets from b fragmentation

Jets originating from the hadronisation of bottom quarks can be discriminated from jets from gluons and light-flavour quarks as well as charm quark fragmentation through the use of b-tagging. There are a multitude of algorithms developed within CMS to perform b-tagging [165, 166] on jets that fall within the pseudorapidity acceptance of the trackers. These algorithms exploit the properties of the b quark to identify the jets formed by its fragmentation. These hadrons have relative large masses, long lifetimes and daughter particles with hard momentum spectra. Additionally, their semi-leptonic decays can be exploited as well. To use b-jet identification in an analysis, one needs to know its efficiency and misidentification probability. In general these are function of the pseudorapidity and transverse momentum of the considered jet. Their performances are directly measured from data by use of b-jet enriched jet samples (multi-jet or top-quark decays).

This thesis uses b-jets identified by the Combined Secondary Vertex version 2 (CSVv2) algorithm [165]. This algorithm combines secondary vertices together with track based lifetime information by use of a multivariate technique. The secondary vertex is reconstructed from displaced tracks within a jet, as illustrated in Figure 4.6. The final state b quark is encapsulated in a B meson (e.g. B^\pm, B_0, B_S) after the hadronisation. This B meson has relatively long

1369 lifetime and can travel a measurable distance from the primary vertex before decaying¹. After
 1370 reconstruction, the secondary vertices are required to be in accordance with the B meson
 1371 hypothesis bases on the amount of shared tracks with the primary vertex, the invariant vertex
 mass to reject kaon decays, and the direction of the tracks compared to the jet axis.

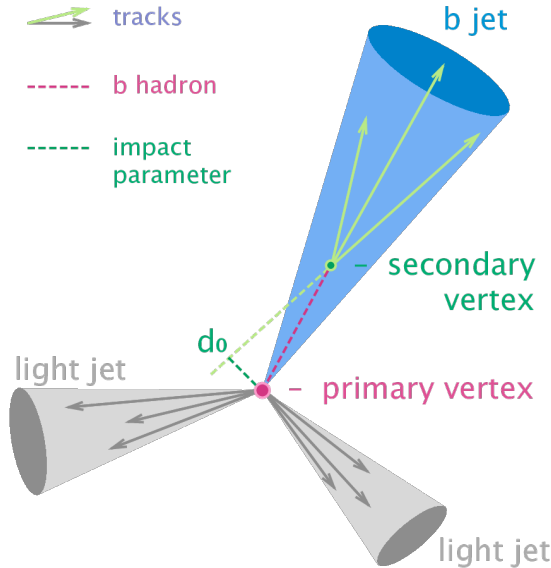


Figure 4.6: Sketch showing the common principle of the identification of b-jets. Figure taken from [167]

1372

1373 The b-tagging algorithm performances are evaluated taking into account two cases: discrim-
 1374 ination of b-tagged jets originating from charm quarks, and discrimination of b-tagged jets
 1375 against jets coming from gluons or light (u, d, s) quarks. In Figure 4.7, the misidentification
 1376 probabilities for different b-tagging algorithms within CMS are shown. Based on the misiden-
 1377 tification probabilities for a certain threshold on the CSVv2 discriminator, different working
 1378 points (WP) are defined. These are shown in Table 4.6. The analysis presented in this thesis
 1379 uses the loose working point which has an average efficiency of 81% and a misidentification
 rate of 10%.

Table 4.6: Working points used for tagging jets as coming from b quarks for the CSVv2 discriminant.

| WP | CSVv2 discr cut | b-tag eff. | misid. prob. |
|------------|-----------------|----------------|-----------------|
| Loose (L) | > 0.5426 | $\approx 81\%$ | $\approx 10\%$ |
| Medium (M) | > 0.8484 | $\approx 66\%$ | $\approx 1\%$ |
| Tight (T) | > 0.9535 | $\approx 46\%$ | $\approx 0.1\%$ |

1380

The efficiency of tagging a jet as coming from a bottom quark in simulation typically deviates somewhat from data. Efficiency scale factors $\epsilon_b^{\text{data}} / \epsilon_b^{\text{MC}}$ are derived from data to account for

¹For example, B^\pm mesons have a lifetime of about 1.6 ps [6] and travel 4-9 mm before decaying if their momenta is 40-100 GeV.

NOTE: Find reason why I am not using cMVA, omdat CSVv2 op ttbar events is gemanen en cMVA op multijet?

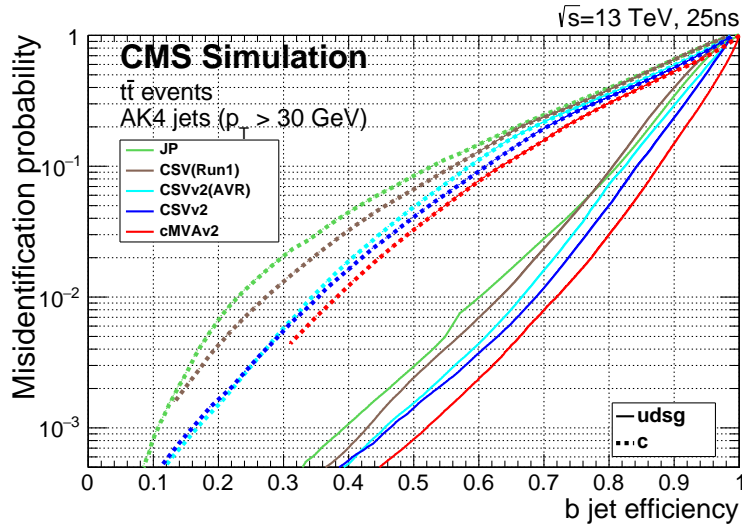


Figure 4.7: Misidentification probabilities of various b-tagging algorithm in simulation. Figure taken from [166].

those differences. These scale factors are η -, p_T -, and flavour dependent, where the flavour of the jet is determined from matched generated hadrons. For cut based analyses these scale factors are applied to the b-tagging efficiencies and mistag rates according to the chosen working point [166]. For shape based analysis however, such as the one presented in this thesis, the scale factor are applied on the distribution of the b-tagging discriminator. This is the so-called IterativeFit method [168]. It uses a tag and probe method to measure the scale factors for both b, c, and light flavoured jets simultaneously. The scale factors to account for the differences in simulation and data for the probe jet are determined iteratively to account for the impact of the b-, c-flavour, and light flavour scale factors on eachother. In a fist step, no scale factors are applied. Then the scale factor is measured by applying the scale factors of the previous iteration to simulation until the scale factors become stable. Throughout the procedure, the scale factor for charm jets are set unity with an uncertainty that is twice the one of the b scale factor. The scale factors obtained in η -, p_T -, and CSVv2 discriminant values are determined with the bin content N of the considered $(\eta, p_T, \text{discriminant})$ bin as

$$\begin{aligned} SF_b &= \frac{N_b^{\text{data}} - N_b^{\text{MC}}}{N_b^{\text{MC}}}, \\ SF_{g,u,d,s} &= \frac{N_{g,u,d,s}^{\text{data}} - N_{g,u,d,s}^{\text{MC}}}{N_{g,u,d,s}^{\text{MC}}}, \\ SF_c &= 1. \end{aligned} \tag{4.6}$$

1381 The uncertainties related to the IterativeFit method cover possible shape discrepancies between
 1382 data and simulation. The uncertainty coming from the purity of the sample is subdivided into
 1383 two uncorrelated uncertainties based on the purity of the light flavoured (lf) and heavy flavoured
 1384 (hf) jet contributions in the sample. Furthermore, the jet energy scale results in jets migrating

from one p_T bin to another, having an influence on bin dependent scale factors. The statistical fluctuations of the limited amount of entries in each bin are also accounted for and have an influence on the scale factor uncertainties. These have four uncorrelated sources: two for heavy flavour and two for light flavour jets. Since the uncertainty on the scale factors for the jets originating from a charm quark (cf) is determined from the uncertainty on the b scale factors resulting in two independent uncertainties [168].

4.5.5 Missing transverse energy

The missing transverse momentum \vec{p}_T and energy E_T^{miss} resulting from particles that do not interact with the detector material, are calculated to balance the vectorial sum of the transverse momenta of all particles:

$$\begin{aligned} E_T &= |\vec{p}_T|, \\ \vec{p}_T &= - \sum_{i=1}^{N_{\text{particles}}} \vec{p}_{T,i}. \end{aligned} \quad (4.7)$$

The z -component can not be calculated from the momentum imbalance since the boost along the z -axis, determined by the momentum fraction, can not be reconstructed.

The missing transverse energy is influenced by the minimum thresholds in calorimeters, the inefficiencies in the tracker, and the non-linear response of the calorimeter to hadronic particles. The bias is reduced by correcting the transverse momentum of the jets to particle jet p_T via the JEC and propagating it to the missing transverse momentum taking into account the energy

$$\begin{aligned} \vec{p}_T^{\text{corr}} &= - \sum_{i=1}^{N_{\text{jets}}} \vec{p}_{T,i}^{\text{corr.}} - \sum_{i=1}^{N_{\text{unclustered}}} \vec{p}_{T,i}^{\text{raw}}, \\ \vec{p}_T^{\text{corr}} &= \vec{p}_T^{\text{raw}} - \sum_{i=1}^{N_{\text{jets}}} (\vec{p}_{T,i}^{\text{JEC}} - \vec{p}_{T,i}^{\text{PU-only}}). \end{aligned} \quad (4.8)$$

The $\vec{p}_{T,i}^{\text{PU-only}}$ denotes the transverse momentum of the jet, where only the pile up related corrections are applied. The performance of the missing transverse energy reconstruction can be found in [169].

4.6 Summary of corrections

Throughout the chapter several corrections are introduced to improve the agreement between data and simulation. These corrections are sources of systematic uncertainties for the analysis presented in this thesis. Therefore a summary of the corrections and their associated uncertainties is provided.

Lepton scale factors The systematic uncertainty on the lepton scale factors consist of three sources: identification, isolation and tracking. The applied scale factors are varied independently within one standard deviation of their measured uncertainties to account for their systematic impact on the measurements.

1406 **Jet energy corrections** The momenta of the reconstructed jets are corrected to match the
 1407 expected true energy derived from the hadronisation products of partons in simulation.
 1408 Furthermore, residual corrections and smearing is applied to match the overall energy
 1409 scale and resolution for simulation and data. These corrections are also propagated to
 1410 the missing transverse energy. The systematic uncertainties due to these scale factors are
 1411 estimated by varying them within their uncertainties and repeating the measurements
 1412 with recalibrated jets and missing transverse energy.

1413 **CSVv2 discriminant shape reweighting** There are three sources of uncertainty contributing
 1414 to the measurement of the scale factors: statistical uncertainties, jet energy scale and
 1415 the purity of the sample. The jet energy scale uncertainty is 100% correlated to the jet
 1416 energy uncertainties and is evaluated simultaneously. The uncertainty coming from the
 1417 purity of the sample is subdivided into two uncorrelated uncertainties based on the purity
 1418 of the light flavoured (lf) and heavy flavoured (hf) jet contributions in the sample. A
 1419 one sigma shift in each of the two purity contributions corresponds to a higher/lower
 1420 contribution in the purity of the considered flavours. The statistical uncertainties has
 1421 four uncorrelated sources, two for heavy flavour and two for light flavour jets. One of
 1422 the uncertainties correspond to the shift consistent with the statistical uncertainties of
 1423 the sample, while the other is propagated in a way that the upper and lower ends of the
 1424 distribution are affected with respect to the centre of the distribution. The uncertainty
 1425 on the charm jet scale factors (cf) is obtained from the uncertainty on the heavy flavour
 1426 scale factors, doubling it in size and constructing two nuisance parameters to control the
 1427 charm flavour scale factors and treating them as independent uncertainties.

1428 **Pile up** Varying the minimum bias cross section, used to calculate the pile up distribution by
 1429 $\pm 4.6\%$, results in a systematic shift in the pile up distribution. The uncertainty is estimated
 1430 by recalculating the pile up weights to the distributions associated to the minimum bias
 1431 cross sections.

1432 **Luminosity** The luminosity is measured with a global uncertainty of 2.5%, affecting the ex-
 1433 pected number of events.

Event selection and categorisation

5

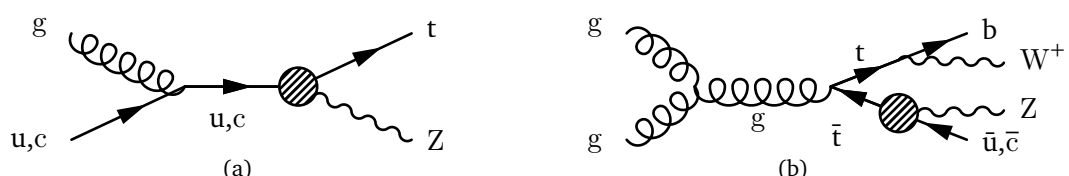
1434

1435 A basic event selection is made for selecting signal like events. The necessary event requirement
1436 are discussed in [Section 5.2](#).

1437 The analysis uses signal and background regions to constrain the huge SM background
1438 compared to the expected signal. [Section 5.4](#) discusses each region that is entering the analysis.
1439 On top of the use of background estimation from control regions, backgrounds that have prompt
1440 leptons contaminated by real leptons either from decays of tau leptons or from hadronized
1441 mesons or baryons (collectively commonly referred as “non-prompt leptons”) as well as by
1442 hadrons or jets misidentified as leptons¹ are evaluated with a data-driven method discussed in
1443 [Section 5.3](#).

1444 5.1 Baseline event selection and filters

1445 The CMS collaboration recorded in the course of 2016 proton at 13 TeV collisions data with a
1446 total recorded integrated luminosity of $35.9 \pm 2.5\% \text{ fb}^{-1}$. The baseline event selection has a
1447 goal to substantially reject SM background events, whilst maintaining a high signal efficiency.
1448 In this analysis a search is performed in a final state made up of a Z boson and a top quark,
1449 associated or not with a jet, in the leptonic decay of the Z boson and the top quark. The leading
order Feynman diagrams can be seen in [Figure 5.1](#).



NOTE:
adapt to
leptonic de-
cay

Figure 5.1: Feynman diagrams for the tZq FCNC interaction with a fully leptonic decay, where the FCNC interaction is indicated with the shaded dot. (a) Single top production through an FCNC interaction. (b) Top pair production with an FCNC induced decay.

1450

¹These two classes of contamination will be referred to as not prompt-lepton (NPL) samples.

1451 The signal considers both the single top FCNC (tZ in the final state) and the top pair FCNC
 1452 ($t\bar{Z}q$ in the final state) events. Their final state signatures consist of three leptons, considering
 1453 electrons or muons in our analysis, and a jet originating from a b quark. For FCNC $t\bar{Z}q$, there is
 1454 an additional up or charm jet. Leptons from tau decays are not vetoed and are entering the
 1455 analysis. Four different lepton channels based on lepton flavour are considered (eee , $e\mu\mu$, $\mu\mu\mu$,
 1456 and $\mu\mu\mu$).

1457 The CMS trigger system, described in Section 2.2.3, filters out the main of the collision events
 1458 from uninteresting processes and dedicated trigger paths are define to single out the events
 1459 with our required detector signature. The trigger paths are chosen based on on-line triggering
 1460 objects with at least one muon (M), at least one electron (E), at least two muons (MM), at
 1461 least two electrons (EE), at least one muon and an electron (ME), at least three muons (MMM),
 1462 at least three electrons (EEE), at least two muons and one electron (MME), or at least two
 1463 electrons and one muon (EEM). For the MC simulation a simple *or* of all triggers is taken and
 1464 the event is taken if it passes one of the trigger paths. For data however, double counting of the
 1465 same event has to be taken into account and a procedure to avoid double counting has been
 1466 put into place. It consists of vetoing in a given dataset the events that are already selected in
 another, as given in Table 5.1.

Table 5.1: Trigger logic used to select data events in order to avoid double counting

| Dataset | Trigger Logic |
|--------------|--|
| $e\mu$ | $EM \parallel EEM \parallel MME$ |
| $\mu\mu$ | $(MM \parallel MMM) \&\& !(EM \parallel EEM \parallel MME)$ |
| ee | $(EE \parallel EEE) \&\& !(MM \parallel MMM) \&\& !(EM \parallel EEM \parallel MME)$ |
| single μ | $M \&\& !(EE \parallel EEE) \&\& !(MM \parallel MMM) \&\& !(EM \parallel EEM \parallel MME)$ |
| single e | $E \&\& !M \&\& !(EE \parallel EEE) \&\& !(MM \parallel MMM) \&\& !(EM \parallel EEM \parallel MME)$ |

1467

1468 This trigger selection strategy is to allow the maximum statistics on the signal region since it
 1469 does not discard events from any dataset. For the single lepton triggers, at least one electron
 1470 (muon) with a transverse momentum p_T higher than 32 GeV (24 GeV) is required. The dilepton
 1471 triggers require an electron (muon) with $p_T > 23$ GeV and a muon (electron) with $p_T > 8$ GeV,
 1472 or an electron (muon) with $p_T > 23$ GeV (17 GeV) and an electron (muon) with $p_T > 12$ GeV
 1473 (8 GeV). Events collected by the trilepton triggers require an electron (muon) with $p_T > 16$ GeV
 1474 (12 GeV), a second electron (muon) of $p_T > 12$ GeV (10 GeV), and a third electron (muon)
 1475 with $p_T > 8$ GeV (5 GeV). The mixed trilepton trigger events require two electrons (muons)
 1476 with $p_T > 12$ GeV (9 GeV) and a third muon (electron) with $p_T > 8$ GeV (9 GeV). The HLT
 1477 trigger paths used in data and simulation are summarised in Table 5.2.

1478 In order to ensure a full trigger efficiency, the offline p_T tresholds are set higher than the on-
 1479 line trigger thresholds. Selected electrons (muons) are required to have $p_T > 35$ (30) GeV and
 1480 $|\eta| < 2.1$ (2.4). A quantity for evaluating lepton isolation is calculated as the summed energy of
 1481 all particles (charged hadrons, neutral hadrons, photons) in a cone of radius $\Delta R < 0.3$ (0.4)
 1482 around the electron (muon), excluding the electron (muon) itself, and divided by the lepton p_T
 1483 . An electron candidate is selected if this isolation quantity is below 0.059 in the barrel region

Table 5.2: HLT trigger paths used to select data and simulation events.

| Trigger path name | Trigger type |
|---|--------------|
| HLT_Mu23_TrkIsoVVL_Ele8_CaloIdL_TrackIdL_IsoVL_v | ME |
| HLT_Mu23_TrkIsoVVL_Ele8_CaloIdL_TrackIdL_IsoVL_DZ_v | ME |
| HLT_Mu8_TrkIsoVVL_Ele23_CaloIdL_TrackIdL_IsoVL_v | ME |
| HLT_Mu8_TrkIsoVVL_Ele23_CaloIdL_TrackIdL_IsoVL_DZ_v | ME |
| HLT_DiMu9_Ele9_CaloIdL_TrackIdL_v | MME |
| HLT_Mu8_DiEle12_CaloIdL_TrackIdL_v | EEM |
| HLT_IsoMu24_v | M |
| HLT_IsoTkMu24_v | M |
| HLT_Ele32_eta2p1_WPTight_Gsf_v | E |
| HLT_Mu17_TrkIsoVVL_Mu8_TrkIsoVVL_v | MM |
| HLT_Mu17_TrkIsoVVL_TkMu8_TrkIsoVVL_v | MM |
| HLT_Mu17_TrkIsoVVL_Mu8_TrkIsoVVL_DZ_v | MM |
| HLT_Mu17_TrkIsoVVL_TkMu8_TrkIsoVVL_DZ_v | MM |
| HLT_TripleMu_12_10_5_v | MMM |
| HLT_Ele23_Ele12_CaloIdL_TrackIdL_IsoVL_DZ_v | EE |
| HLT_Ele16_Ele12_Ele8_CaloIdL_TrackIdL_v | EEE |

1484 and below 0.057 in the end caps. A muon candidate is selected if this isolation quantity is
 1485 below 0.15. Other lepton selection criteria are applied in analysis based on the values of various
 1486 quantities determined during the reconstruction, such as number of missing track hits or the
 1487 electromagnetic shower created by the particles. These are given in [Section 4.5.1](#) ([Table 4.1](#))
 1488 and [Section 4.5.2](#) ([Table 4.3](#)). The trigger efficiency estimation is described in [Section 5.1.2](#).

1489 The samples are pre-selected off-line to ensure that all reconstructed particles considered
 1490 for the analysis are corresponding to a proton interaction and that signals from beam halo
 1491 particles as well as detector noise is removed. For this reason, several filters are used. These are
 1492 described in [Section 5.1.1](#).

1493 On top of leptons, jets and missing transverse energy are expected from the signal signature.
 1494 The jets are reconstructed using the anti- k_T algorithm with a distance parameter of 0.4 using
 1495 the particle flow particles that are not identified as isolated leptons as input. The jet momentum
 1496 is determined as the vectorial sum of the particles contained in the jet. Additional selection
 1497 criteria are applied to each event to remove spurious jet-like features originating from isolated
 1498 noise patterns in certain hadron calorimeter regions. More information about the jets used for
 1499 this analysis can be found in [Section 4.5.3](#). The jets are calibrated in simulation and in data
 1500 separately, accounting for deposits from pileup and the non-linear detector response. Calibrated
 1501 jets with $p_T > 30$ GeV and $|\eta| < 2.4$ are selected. A selected jet may still overlap with the
 1502 selected leptons leading to a double-counting. To prevent such cases, jets that are found within
 1503 a cone of $R = 0.3$ around any of the signal electrons (muons) are removed from the set of
 1504 selected jets.

1505 The jets originating from b quarks are tagged using the CSVv2 algorithm, which combines
 1506 the information of displaced tracks with information of secondary vertices associated with the
 1507 jet using a multivariate technique. The jets are tagged as a jet coming from a b quark (b-tagged)
 1508 if the CSVv2 discriminator is above a certain threshold. This analysis uses a threshold that
 1509 results in an average b-tagging efficiency of 81% and a misidentification rate of 10%. More
 1510 information about b-tagging can be found in [Section 4.5.4](#).

1511 The missing transverse momentum vector \vec{p}_T is defined as the projection on the plane
 1512 perpendicular to the beams of the negative vector sum of the momenta of all reconstructed
 1513 particles in an event. Its magnitude is denoted by E_T^{miss} as shown in [Section 4.5.5](#). Its longitudinal
 1514 component is calculated by limiting the lepton + neutrino to the W boson mass. In case two
 1515 solutions arise, the mass closest to the known top quark mass is used. The events and their
 1516 corresponding object collections reconstructed using the reconstruction criteria described in
 1517 [Section 4.1](#), are used as input for the analysis. Further requirements on the momenta and the
 1518 pseudo rapidities are made to fulfil the trigger requirements and reconstruction algorithms.

1519 5.1.1 Event cleaning

1520 Some events arising from instrumental noise and beam backgrounds might end up in the
 1521 data [[169](#), [170](#)]. Spurious deposits may appear in the ECAL from non collision origins such
 1522 as beam halo particles, or from particles striking the sensors in the ECAL photo detectors.
 1523 Conjointly, dead ECAL cells can cause artificial missing transverse energy. The HCAL can cause
 1524 spurious energy from particle interactions with the light guides and the photomultiplier tubes
 1525 of the HF, as well as noisy hybrid photo diodes. In CMS, different algorithms, so-called filters,
 1526 are developed to identify and suppress these events.

1527 The ECAL electronics noise and spurious signals from particle interactions with photo detectors
 1528 are mostly removed via topological and timings based selection using ECAL information only.
 1529 The remaining effects such as anomalously high energy crystals and the lack of information
 1530 for channels due to inefficiencies in the read out are removed through dedicated events filters.
 1531 Five ECAL endcap supercrystal have been identified for giving anomalously high energies due
 1532 to high amplitude pulses in several channels at once, and are masked. Furthermore, the crystal
 1533 read out from a small amount of ECAL towers is not available. However, their trigger primitive
 1534 information is still available making it possible to estimate the magnitude of unmeasured energy
 1535 and when the value is too large, the event is filtered out.

1536 The machine induced particles, via beam-gas / beam-pipe/... interactions, that are flying with
 1537 the beam affect the physics analysis. They leave a calorimeter deposit along a line at constant
 1538 ϕ in the calorimeter, and interactions in the CSCs will often line up with this deposit. This
 1539 can be seen in [Figure 5.2](#). Therefore, events containing such beam halo particles are removed
 1540 from the selection with the CSC Beam Halo Filter. This filter uses information related to the
 1541 geometric quantities, energy deposits, and timing signatures. For 2016, the filter rejects 85% in
 1542 a halo-enriched sample, whereas the mistag probability determined from simulation if found to
 1543 be less than 0.01%.

1544 Furthermore, there is anomalous high missing transverse energy coming from low quality
 1545 muons that lead to high- p_T tracks, but are considered not good by the particle flow algorithm.

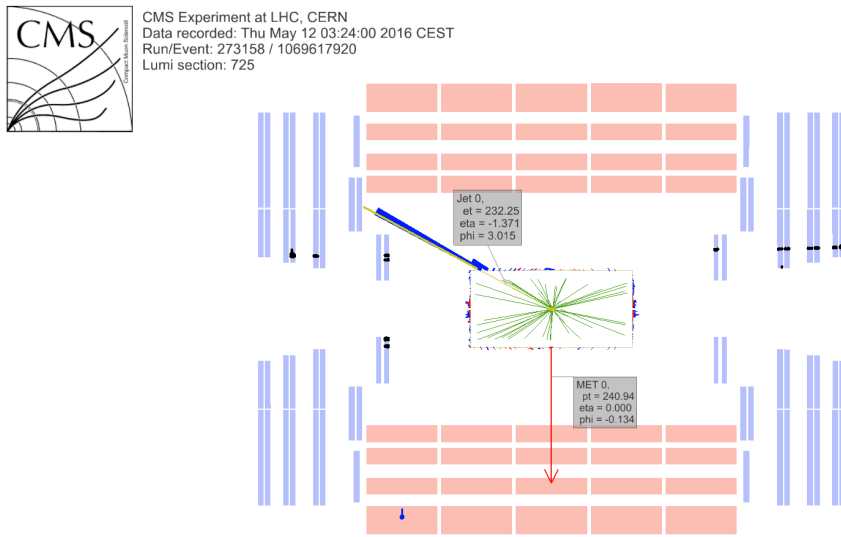


Figure 5.2: Event display of a beam halo event with collinear hits in the CSC (black), missing transverse energy of 250 GeV and a jet of 232 GeV. The hadronic deposit is spread in η , but narrow in ϕ . Figure taken from [169].

1546 These low quality tracks will be mislabelled as charged hadrons and will therefore be used in
 1547 the calculation of the missing transverse energy. By investigating the purity of the reconstructed
 1548 tracks and the relative transverse momentum error of the muons, these events can be filtered
 1549 out.

1550 Supplementary to previous filters, only events with where the first primary vertex is a well
 1551 reconstructed primary vertex are selected. The reconstructed primary vertex should have at
 1552 least five degrees of freedom, the longitudinal distance from the beam spot is maximally 24 cm
 1553 ($d_z < 24$ cm), and the transversal distance from the beam spot is maximally 2 cm ($d_{xy} < 2$ cm).

1554 5.1.2 Estimation of the trigger efficiency

1555 The trigger efficiency in data is estimated using a data sample collected using unprescaled E_T^{miss}
 1556 triggers. These allow events with a missing transverse energy higher than 110 GeV(120 GeV)
 1557 and that the scalar sum of the transverse momenta of the reconstructed PF jets $H_T^{\text{trig.}}$ is at least
 1558 300 GeV (120 GeV), or a calorimeter/PF E_T^{miss} higher than 200 GeV/300 GeV. For an HB-HE
 1559 cleaned event the PF missing transverse energy threshold is lowered to 170 GeV. These trigger
 1560 paths are summarised in Table 5.3 and chosen to be completely uncorrelated with the lepton
 1561 triggers given in Table 5.2.

Table 5.3: Unprescaled E_T^{miss} HLT trigger paths for estimating the trigger efficiency. An *or* of the triggers is used to select events.

| Trigger path | Requirement |
|--------------------------------|--|
| HLT_PFHT300_PFMET110_v* | PF $E_T^{\text{miss}} > 110 \text{ GeV}$, PF $H_T^{\text{trig.}} > 300 \text{ GeV}$ |
| HLT_MET200_v* | calorimeter $E_T^{\text{miss}} > 200 \text{ GeV}$ |
| HLT_PFMET300_v* | PF $E_T^{\text{miss}} > 300 \text{ GeV}$ |
| HLT_PFMET120_PFT120_IDTight_v* | PF $E_T^{\text{miss}} > 120 \text{ GeV}$, PF $H_T^{\text{trig.,tightWP}} > 120 \text{ GeV}$ |
| HLT_PFMET170_HBHECleaned_v* | PF $E_T^{\text{miss}} > 170 \text{ GeV}$, cleaned for HB/HE anomalous signals |

The studied simulation sample is the main background, WZ+jets, with all corrections applied. For this study, the events passing a three lepton cut and at least one jet are being used. The corresponding efficiencies are then calculated as

$$\epsilon_{\text{data}} = \frac{\text{Nb. of events passing lepton and MET triggers}}{\text{Nb. of events passing MET triggers}} \quad (5.1)$$

$$\epsilon_{\text{MC}} = \frac{\text{Nb. of events passing lepton triggers}}{\text{Nb. of total events}} \quad (5.2)$$

The resulting efficiencies and scale factors can be found in [Table 5.4](#), where the scale factors are defined as

$$SF = \frac{\epsilon_{\text{data}}}{\epsilon_{\text{MC}}} \quad (5.3)$$

More detailed scale factors and efficiencies can be found in [Appendix A](#).

Table 5.4: Trigger scale factors for each channel, after three lepton + jets cut, in the Z mass window. by counting number of events.

| | all | $\mu\mu\mu$ | eee | ee μ | e $\mu\mu$ |
|--|--------|-------------|--------|----------|------------|
| | 1.0000 | 1.0000 | 0.9541 | 1.0006 | 1.0004% |

1562

1563 The trigger efficiencies are also measured in function of the p_T of the leptons for which the
 1564 distributions can be found in [Appendix A](#). The resulting scale factors in can be found in Figure
 1565 [Figure 5.3](#). The trigger efficiencies are measured to be nearly 100% for both simulation and
 1566 data. The results are dominated by statistics and assigning a large uncertainty to the trigger
 1567 efficiency based on the dataset collected by E_T^{miss} triggers would be over conservative. A one
 1568 percent uncertainty on the trigger selection for the ee μ and $\mu\mu\mu$ final states, and 5% for the
 1569 eee and e $\mu\mu$ final states is assigned instead. No scale factors will be applied on simulation as
 1570 they are close to unity. Control plots are made in the dilepton region to validate all corrections
 applied to simulation and can be found in [Appendix B](#).

NOTE: 1571
Make sure
this is the
case

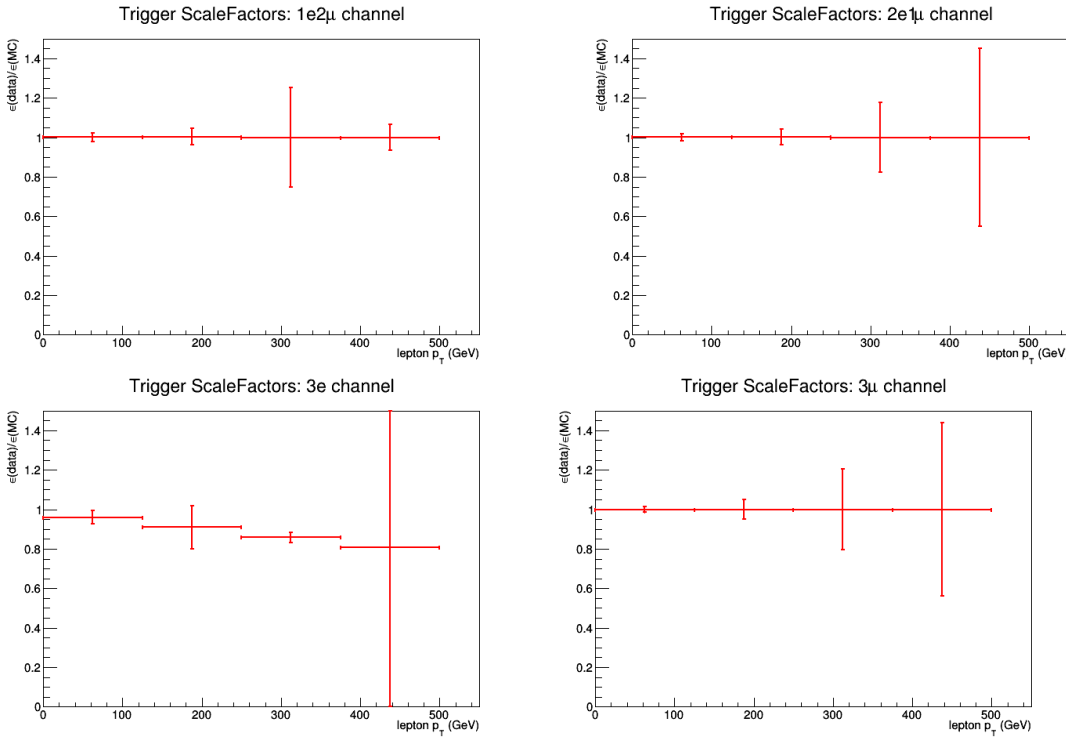


Figure 5.3: The trigger scale factors measured as a function of lepton p_T , using the dataset collected by E_T^{miss} triggers and WZ simulation, after a 3 lepton and jets selection, in the Z mass window. All corrections to simulation are applied. Left, upper: ee μ channel. Right, upper: ee μ channel. Left, lower: ee channel. Right, lower: $\mu\mu\mu$ channel

1572 5.1.3 Corrections

1573 Mismatches between data and simulation are corrected for via the use of scale factors. These
 1574 are elaborately discussed in [Section 4.5](#). In this section a short overview of the applied corrections
 1575 is given and their effect on a dilepton selection is shown.

1576 Pile up reweighting

1577 In data, the number of interactions per bunch crossing (pile up) is calculated with a minimum
 1578 bias cross section of 69.2 mb. The number of simulated pile up events is then reweighted to
 1579 match the expected number of pile up events in data. Pile up reweighting manifests itself as an
 1580 altered shape of the number of reconstructed primary vertices as can be seen in [Figure 5.4](#).

1581 Note that [Figure 5.4](#) indicates that even after pile up reweighting, the primary vertex multi-
 1582 plicity is not well described by simulation. This is a known effect, and using a minimum bias
 1583 cross section with a slightly lower value is found to better describe the data. However, the b
 1584 tagging scale factors are only provided for the nominal inelastic cross section, and thus this
 1585 value is used.

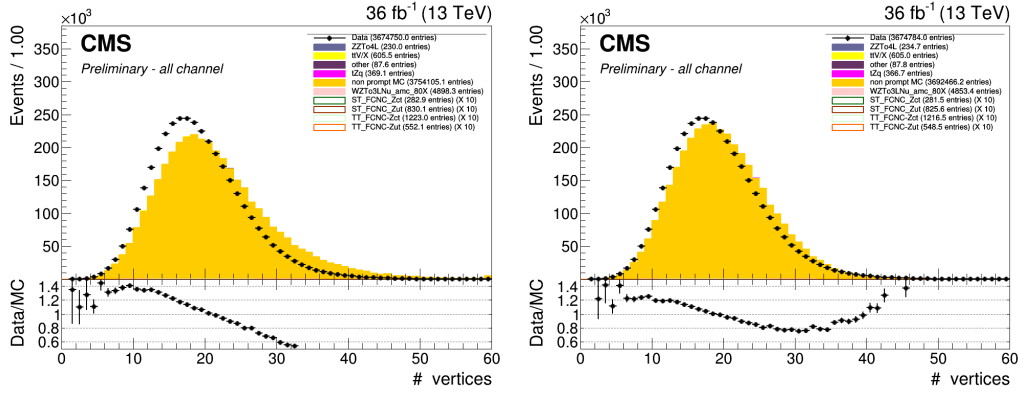


Figure 5.4: The number of primary vertices before (left) and after (right) pile up reweighting. After a 2 lepton plus jets selection, in the Z mass window.

1586 Lepton scale factors

The efficiency to select leptons is different in simulation (ϵ_{MC}) compared to the data (ϵ_{data}). This is corrected for by applying lepton scale factors (SF) to the simulation that are defined as

$$SF = \frac{\epsilon_{\text{data}}}{\epsilon_{\text{MC}}}. \quad (5.4)$$

These scale factors are measured for the identification, isolation, tracking and trigger efficiencies of the objects as a function of p_{T} and η (see Section 4.5.1 and Section 4.5.2). Multiplying these scale factors for each lepton provides an overall efficiency:

$$SF_{\text{global}}^{\mu} = \prod_{\text{i}}^{\#\mu} SF_{\text{ID}}^{\mu}(p_{\text{T}}, \eta) SF_{\text{Iso.}}^{\mu}(p_{\text{T}}, \eta) SF_{\text{Trig.}}^{\mu}(p_{\text{T}}, \eta) SF_{\text{track}}^{\mu}(p_{\text{T}}, \eta), \quad (5.5)$$

$$SF_{\text{global}}^e = \prod_{\text{i}}^{\#e} SF_{\text{ID}}^e(p_{\text{T}}, \eta) SF_{\text{Iso.}}^e(p_{\text{T}}, \eta) SF_{\text{Trig.}}^e(p_{\text{T}}, \eta) SF_{\text{track}}^e(p_{\text{T}}, \eta). \quad (5.6)$$

1587 The effect of the scale factors can be found in Figure 5.6 for the electron scaling and Figure 5.5
1588 for the muons. The trigger efficiencies are estimated in Section 5.1.2.

1589 Additionally, corrections are made for the energy resolution of the leptons. For the electrons,
1590 energy smearing and regression is applied [171]. The energy regression uses the detector
1591 information to correct the electron energy in order to have the best energy resolution by
1592 correcting local energy containment, material effects, etc.. The energy scale and smearing
1593 is done in order to bring the data energy scale to simulation level. It smears the simulation
1594 energies to have identical energy resolution in simulation and data. For the muons, the p_{T} is
1595 corrected using the Rochester method [172, 173]. This correction removes the bias of the muon
1596 p_{T} from any detector misalignment or any possible error of the magnetic field. The effect of
1597 the Rochester correction can be found in Figure 5.7.

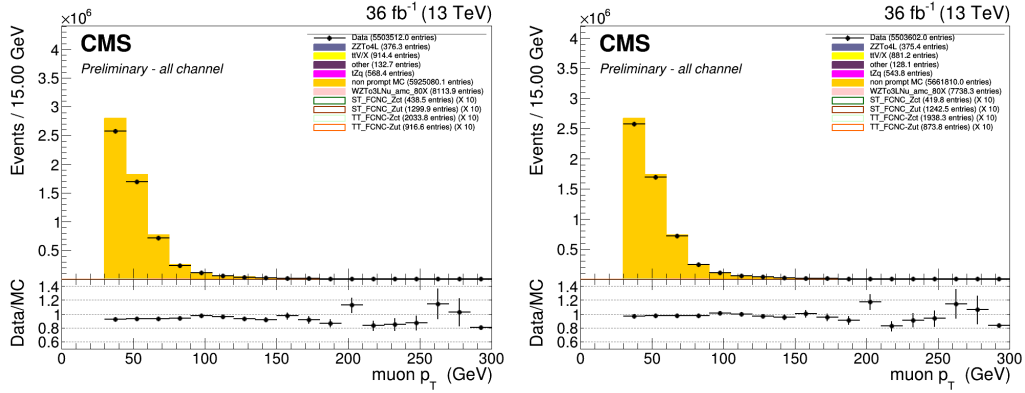


Figure 5.5: The p_T of the muons before (left) and after (right) muon scale factors. After a 2 lepton plus jets selection, in the Z mass window. Both after the Rochester correction.

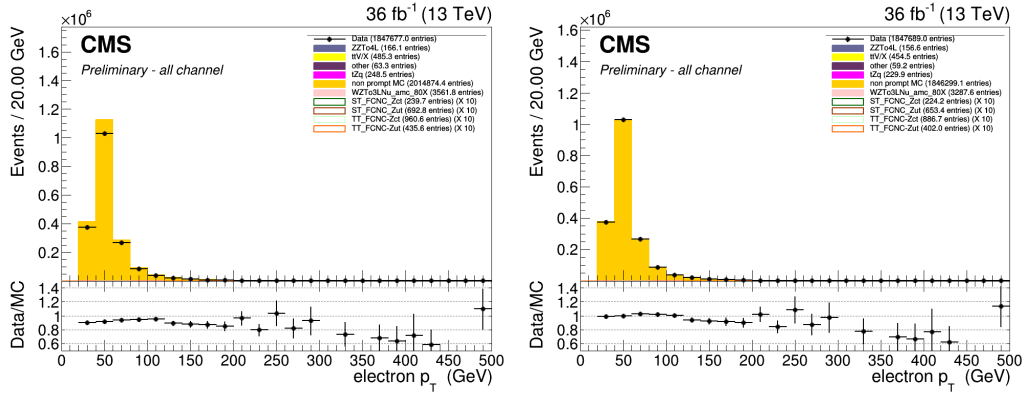


Figure 5.6: The p_T of the electrons before (left) and after (right) electron scale factors. After a 2 lepton plus jets selection, in the Z mass window. Both after energy scale corrections and smearing.

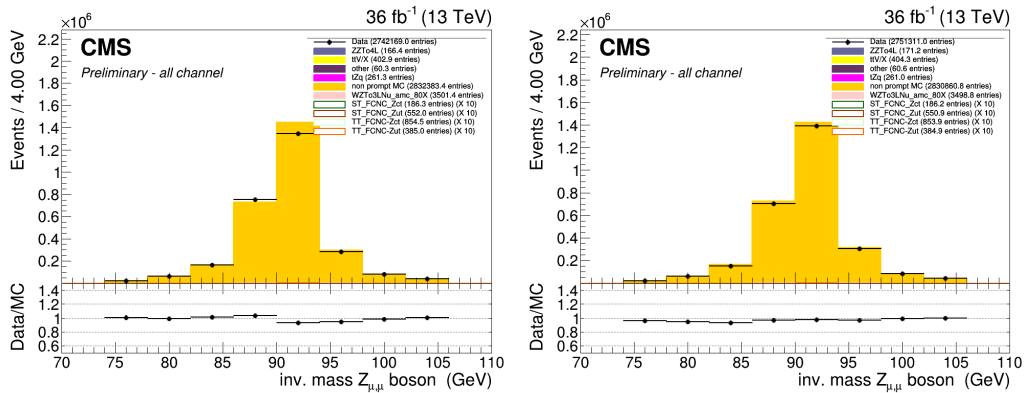


Figure 5.7: The mass of the Z boson consisting of the muons before (left) and after (right) the rochester correction. After a 2 lepton plus jets selection, in the Z mass window.

1598 CSVv2 shape correction

1599 In order to make the shape of the CSVv2 b-tagging discriminant in simulation agree with data,
 1600 jet-by-jet based scale factors are applied. These scale factors are a function of the p_T , η and
 1601 CSVv2 value of the jet as discussed in Section 4.5.4. The effect of these scale factors can be
 1602 found in Figure 5.8.

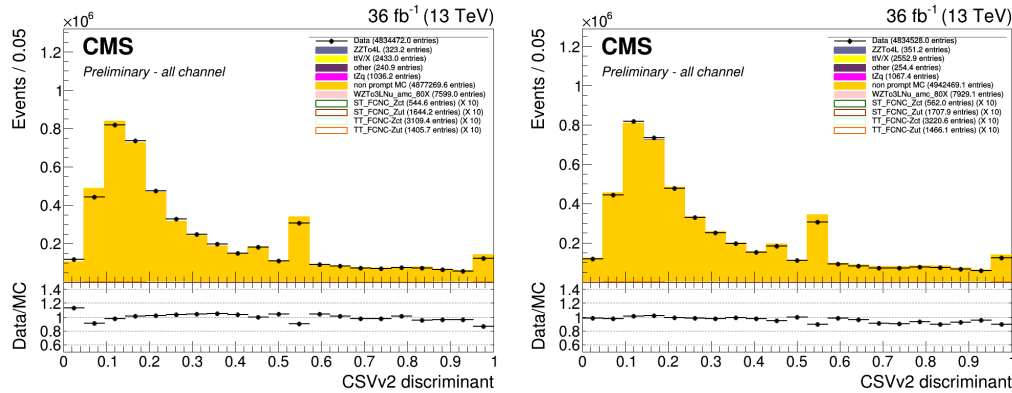


Figure 5.8: The CSVv2 discriminant of the jets before (left) and after (right) b-tag scale factors. After a 2 lepton plus jets selection, in the Z mass window.

1603 Jet energy

1604 The jet energy in data and simulation is corrected by the measured energy response of the
 1605 detector. This provides p_T - η dependent scale factors and are directly taken from the frontier
 1606 condition database as discussed in Section 4.5.3. The effect of the jet energy corrections can be
 found in Figure 5.9 and Figure 5.10.

NOTE: Figure 1607
jer plot

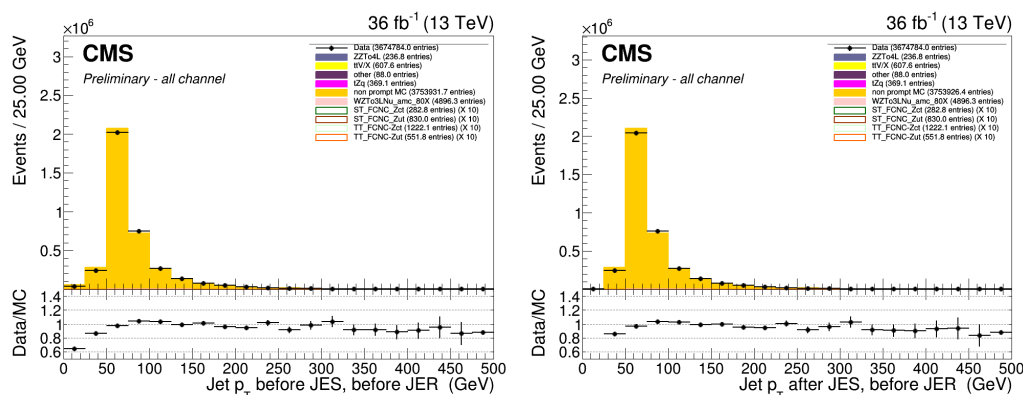


Figure 5.9: The p_T of the jets before (left) and after (right) jet energy scale corrections. After a 2 lepton plus jets selection, in the Z mass window.

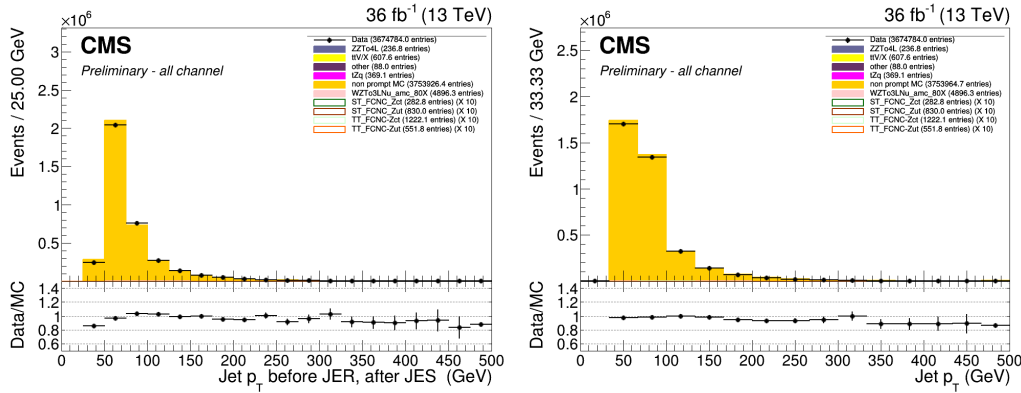


Figure 5.10: The p_T of the jets before (left) and after (right) jet energy resolution smearing. After a 2 lepton plus jets selection, in the Z mass window.

1608 Missing transverse energy

1609 The energy scale and resolution corrections applied to the jets are propagated back to the
 1610 missing transverse energy (smeared Type I correction). This rebalances the transverse net
 1611 momentum of the event and improves the missing transverse energy resolution itself.

1612 5.2 Analysis Strategy

1613 The analysis strategy uses five statistically independent regions to extract limits using a likelihood
 1614 fit of various observables. Two signal regions, the tZ (STSR) and tZq (TTSR) signal region, are
 1615 constructed using the jet multiplicity, focussed on each signal signature (see Tab. 5.7). In order
 1616 to constrain the rate of WZ +jet events as well as that of NPL backgrounds three control regions
 1617 are defined. The WZ control region (WZCR) focusses on NPLs originating from Z/γ^* + jets and
 1618 simultaneously constrains the WZ +jets background rate. The NPL backgrounds coming from
 1619 $t\bar{t}$, are constrained by two control regions, TTCSR and STCSR, one for each signal region (TTSR
 1620 and STSR). In the STSR and TTSR multivariate discriminants based on Boosted Decision Trees
 1621 (BDT) are used to respectively discriminate FCNC tZ and FCNC tZq from backgrounds. In the
 1622 WZCR a discriminating variable between the two backgrounds, WZ +jets and NPLs, is used.
 1623 In TTCSR and STCSR the dominating process is $t\bar{t}$ +jets, and its rate is estimated by subtracting
 1624 all other background predictions from data. A simultaneous global fit is performed taking
 1625 into account each region (STSR, TTSR, WZCR, TTCSR and STCSR) for the four different leptonic
 1626 channels.

1627 5.3 Data driven NPL background simulation

1628 The MC samples are used to model the backgrounds as well as for training the boosted decision
 1629 trees for signal to background separation. One of the most important background consist of
 1630 events with not prompt leptons. These are mostly instrumental background and are therefore
 1631 very difficult to model. The NPL background is estimated from data for both its shape and its
 1632 normalisation.

1633 The NPL sources are

- 1634 • hadronic objects wrongly reconstructed as leptons,
 1635 • real leptons coming from the semi leptonic decay of a b or c hadron,
 1636 • real leptons coming from the conversion of photons,

1637 that pass the identification and isolation requirements. The dominant source of these NPLs
 1638 depend on the flavour of the lepton and therefore the events with a noy prompt muon ($\text{NP}\mu$)
 1639 are treated differently than those with a not prompt electron (NPE). For muons, the dominant
 1640 source is the semi leptonic decay of heavy flavour hadrons. For electrons, the dominant sources
 1641 are hadrons and photon conversions.

1642 The backgrounds causing NPL contributions are mostly $Z/\gamma^* + \text{jets}$ (Drell–Yan) and $t\bar{t} + \text{jets}$
 1643 dilepton processes, and in a smaller amount WW and tWZ. All of these backgrounds contain
 1644 two real leptons and one NPLDue to the fact that the probability for a lepton to be a NPL is
 1645 small, backgrounds containing two or more NPL s are neglected. The assumption is made that
 1646 for DY the two leptons compatible with a Z boson decay are the real leptons, and the additional
 1647 lepton is coming from a NPL source, while for $t\bar{t} + \text{jets}$ the NPL is associated to the Z boson.

1648 The NPL sample is constructed from data by requiring exactly three leptons, from which two
 1649 are considered real, isolated leptons and the third is a NPL. This NPL is created by loosening its
 1650 identification and inverting its isolation criteria. The full requirements on the not prompt leptons
 1651 are given in [Table 5.5](#) and [Table 5.6](#). For NPEs, a large fraction is coming from misidentified
 1652 photons. These are removed by applying a tighter cut on the $1/E - 1/p$ variable, and by limiting
 1653 the isolation values to be smaller than one.

1654 The NPL samples are defined in a given control region and are used to describe their contribu-
 1655 tion in the other regions.

Table 5.5: Non prompt electron requirements used in this analysis. The requirements are set in the barrel ($|\eta_{\text{supercluster}}| \leq 1.479$) and the end caps ($|\eta_{\text{supercluster}}| > 1.479$).

| | $ \eta_{\text{supercluster}} \leq 1.479$ | $ \eta_{\text{supercluster}} > 1.479$ |
|-----------------------------|---|--|
| $\sigma_{\eta\eta}$ | < 0.011 | < 0.0314 |
| $ \Delta\eta_{\text{in}} $ | < 0.00477 | < 0.00868 |
| $ \Delta\phi_{\text{in}} $ | < 0.222 | < 0.212 |
| H/E | < 0.298 | < 0.101 |
| relative isolation | $\geq 0.0588 \&& < 1$ | $\geq 0.0571 \&& < 1$ |
| $ 1/E - 1/p $ | $< 0.0129 \text{ GeV}^{-1}$ | $< 0.0129 \text{ GeV}^{-1}$ |
| expected missing inner hits | ≤ 1 | ≤ 1 |
| pass conversion veto | Y | Y |
| p_T | $> 35 \text{ GeV}$ | $> 35 \text{ GeV}$ |

Table 5.6: Non prompt muon requirements used in the analysis.

| | modified Loose Muon WP |
|--|------------------------|
| Global muon or Tracker Muon | Both |
| Particle Flow muon | Y |
| $\chi^2/ndof$ of global muon track fit | N/A |
| Nb. of hit muon chambers | N/A |
| Nb. of muon stations contained in the segment | N/A |
| Size of the transverse impact parameter of the track wrt. PV | N/A |
| Longitudinal distance wrt. PV | N/A |
| Nb. of pixel hits | N/A |
| Nb. of tracker layers with hits | N/A |
| Relative Isolation | ≥ 0.15 |
| p_T | > 30 GeV |

5.4 Regions and channels

The regions are defined as in Table 5.7 after a common selection of

- exactly 3 leptons containing one opposite sign, same flavour pair that are assigned to the Z boson,
- at least 1 jet and at the most 3 jets,
- the transverse mass of the W boson to be maximal 300 GeV,

The cut on the transverse mass of the W boson is done to remove events that are passing the events cleaning elading to anomalous large missing transverse energy. The transverse mass $m_T(W)$ is reconstructed using

$$m_T(W) = \sqrt{(p_T(l_W) + p_T(v_W))^2 - (p_x(l_W) + p_x(v_W))^2 - (p_y(l_W) + p_y(v_W))^2} \quad (5.7)$$

Table 5.7: The statistically independent regions used in the analysis.

| | WZCR | STSR | TTSR | STCR | TTCR |
|--------------------------------|----------|------|----------|------|----------|
| Number of jets | ≥ 1 | 1 | ≥ 2 | 1 | ≥ 2 |
| Number of b jets | 0 | 1 | ≥ 1 | 1 | ≥ 1 |
| $ m_Z^{reco} - m_Z < 7.5$ GeV | Yes | Yes | Yes | No | No |

Additional leptons are vetoed in order to reduce the contamination of backgrounds with four or more leptons in the final state, e.g. ZZ, t̄Z, and t̄H. The most important backgrounds are the ones that contain three prompt leptons in the final state. These are mainly WZ+jets, t̄Z and SM tZq. For these backgrounds, the three lepton topology is identical to the FCNC signal:

1666 two opposite sign leptons of the same flavour decaying from the Z boson, and a third additional,
 1667 high p_T lepton coming from the W boson decay.

1668 For the FCNC tZ final state, one b jet coming from the SM top decay is expected. For the
 1669 FCNC tZq, an additional light jet is expected. In the t \bar{t} Z final state, two b jets are present in the
 1670 final state. However, due to inefficiencies of the b-tagging algorithm, one of the two b jets may
 1671 be identified as a light quark jet, giving the same final state as the FCNC tZq final state. For
 1672 the WZ+jets final states, one of the b jets produced by gluon splitting can be b-tagged or light
 1673 flavour jets coming from the WZ+jets production can be mis-tagged as b jets. The SM tZq final
 1674 state expects the same signal as FCNC tZq.

1675 The NPL events give a significant background contribution. This background is coming mainly
 1676 from Z/ γ^* + jets and t \bar{t} +jets processes (in a less significant way, also WW and tWZ contributes),
 1677 which have very high cross sections and causes a large number of NPL background events
 1678 compared to signal.

1679 In order to reduce the large uncertainties in backgrounds, five independent regions are used
 1680 as defined in Table 5.7.

1681 5.4.1 WZ control region

1682 In this region, a fit is performed on the transverse mass of the W boson, in order to estimate
 1683 the NPL yield coming from Z/ γ^* + jets and the WZ+jets backgrounds.

A transfer factor is used to account for going from a region without b-tagged jets to a region with exactly one b-tagged jet, or at least one b-tagged jet. For this the probability of tagging at least one jet with the CSVv2 loose working point is used to calculate the expected number of events, N_b , after b tagging:

$$N_b = \frac{\sum_{\text{events}} \mathcal{P}_b}{\text{total nb of events}}, \quad (5.8)$$

where \mathcal{P}_b is the probability that an event survives the b-tagging requirement

$$\begin{aligned} \mathcal{P}_b &= 1 - P(\text{event doesn't survive b tag}) \\ &= 1 - \left(\prod_b P(\text{b not tagged}) \prod_c P(\text{c not tagged}) \prod_{uds} P(\text{light not tagged}) \right) \end{aligned} \quad (5.9)$$

1684 with the products going over all b-, c-, and light jets. The jet flavour is determined by means
 1685 of matching the reconstructed jet to the generated quark based on the distance in the $\eta\phi$
 1686 plane. In order to estimate the probability for exactly one b-tagged jet, the expected number of
 1687 events is corrected by the fraction of events with exactly one jet in the WZCR. The resulting
 1688 transfer factors are given in Appendix C. One can see that the yield of WZ+jets events in the
 1689 signal region estimated using the above described transfer factor and the yield calculated with
 1690 simulated events are in agreement.

NOTE: 1688
make ap-
pendix 1689
1690

1691 **5.4.2 TTCR and STCR**

The TTCR and STCR have the same selection criteria as TTSR and STSR but are outside the Z mass window (sidebands):

$$7.5 \text{ GeV} < |m_Z^{\text{reco}} - m_Z| < 30 \text{ GeV}. \quad (5.10)$$

where $M(Z_{\text{reco}})$ is the reconstructed mass of the Z boson in the event, and $M(Z)$ the mass of the Z boson. These regions are dominated by $t\bar{t}$ +jets (see [Appendix C](#)) and are used to estimate the NPL coming from $t\bar{t}$ +jets in the STSR and TTSR. Since there aren't enough events entering these regions, no shapes are used in the fit. The distribution of the mass of the Z boson is flat for $t\bar{t}$ +jets events, as shown in [Figure 5.11](#), and thus the number of expected events, N_s , in the signal regions estimated from the number of expected events, N_c , in the control region is obtained as

$$N_s = \frac{15}{60 - 15} N_c. \quad (5.11)$$

1692 The resulting transfer factors are given in [Appendix C](#). The expected yield in the signal region
1693 estimated from the TTCR (STCR) is in agreement with the yield calculated from simulated events.

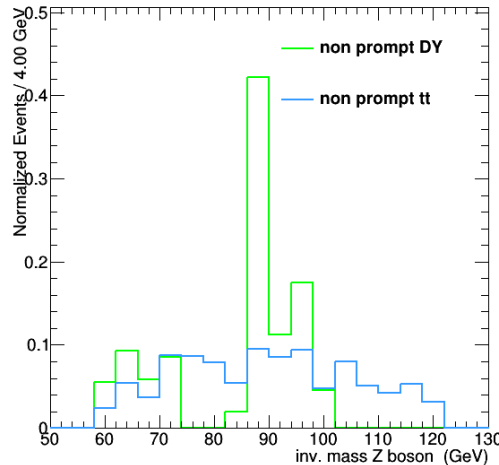


Figure 5.11: The normalized distribution for $Z/\gamma^* + \text{jets}$ and $t\bar{t} + \text{jets}$ events before dividing the events in to regions, after $|m_Z^{\text{reco}} - m_Z| < 30 \text{ GeV}$. All leptonic channels combined.

1694

1695 5.4.3 TTSR and STSR

1696 The TTSR is defined to target top quark pair FCNC (tZq), while the STSR focusses on single top
1697 quark FCNC (tZ). They have NPL contributions coming from $Z/\gamma^* + \text{jets}$ and $t\bar{t} + \text{jets}$ events. In
1698 this region, the data driven NPL template is split into two templates based on the presence of
1699 the NPL in the Z boson:

- 1700 • NPL associated with W boson is assigned to $Z/\gamma^* + \text{jets}$ and estimated in the WZCR.
1701 • NPL associated with Z boson is assigned to $t\bar{t} + \text{jets}$ and estimated in the TTCR and STCR.

The search for FCNC involving a top quark and a Z boson

1702

6

1703 **6.1 Construction of template distributions**

1704 **6.2 Systematic uncertainties**

1705 **6.3 Limit setting procedure**

1706 **6.4 Result and discussion**

Denouement of the top-Z FCNC hunt at 13 TeV

1707

7

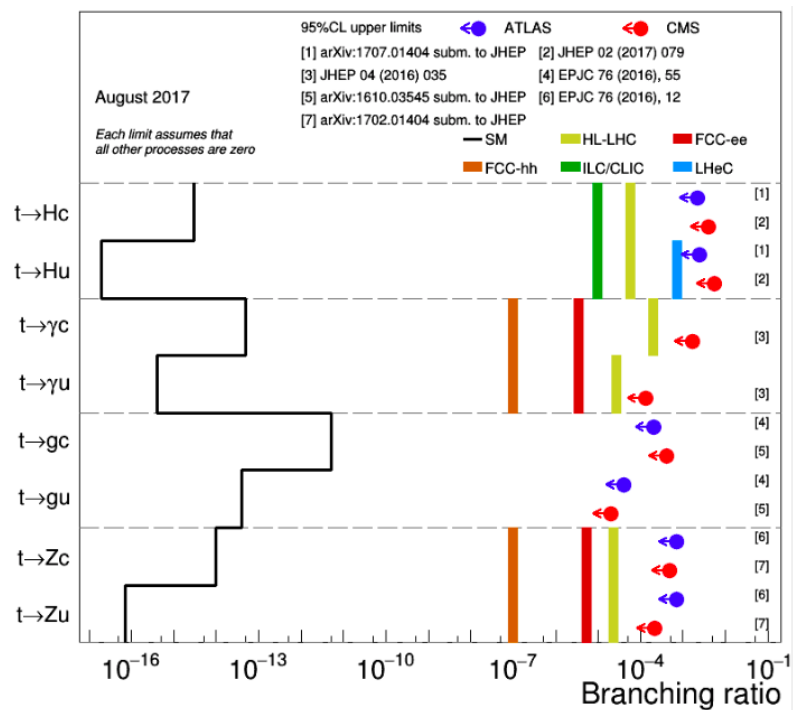


Figure 7.1:

Trigger scale factors

A

1709 The trigger scale factors measured as a function of lepton p_T , using the dataset collected by
 1710 E_T^{miss} triggers and WZ simulation, after a 3 lepton and jets selection, in the Z mass window. All
 1711 corrections to simulation are applied.

Table A.1: Trigger efficiencies on data events selected with E_T^{miss} triggers and WZ simulation for all leptonic channels together. The unweighted number of events is quoted. When there are no events passing the cuts, it is indicated with N/A. The uncertainties are statistical uncertainties.

| ALL CHANNEL | data | | WZ simulations | |
|-------------------------|-------------------|--------|----------------------|-------|
| | Efficiency | unc. | Efficiency | unc. |
| 3 lep, at least one jet | 117/118 = 99.15 % | 12.94% | 18047/18055 = 99.96% | 1.05% |
| STSR | 6/6 = 100.00% | 57.74% | 1541/1541 = 100.00% | 3.60% |
| TTSR | 26/27 = 96.30% | 26.46% | 1791/1792 = 99.94% | 3.34% |
| WZCR | 69/69 = 100.00 % | 17.03% | 14405/14412=99.95% | 1.18% |

Table A.2: Trigger efficiencies on data events selected with E_T^{miss} triggers and WZ simulation for $\mu\mu\mu$ leptonic channel together. The unweighted number of events is quoted. When there are no events passing the cuts, it is indicated with N/A. The uncertainties are statistical uncertainties.

| $\mu\mu\mu$ CHANNEL | data | | WZ simulations | |
|-------------------------|------------------|---------|---------------------|-------|
| | Efficiency | unc. | Efficiency | unc. |
| 3 lep, at least one jet | 40/40 = 100.00 % | 22.36 % | 7814/7814 = 100.00% | 1.60% |
| STSR | N/A | N/A | 687/687 = 100% | 5.40% |
| TTSR | 13/13 = 100.00% | 39.22% | 763/763 = 100.00% | 5.12% |
| WZCR | 22/22 = 100.00 % | 30.15% | 6238/6238=100.00% | 1.79% |

Table A.3: Trigger efficiencies on data events selected with E_T^{miss} triggers and WZ simulation for eee leptonic channel together. The unweighted number of events is quoted. When there are no events passing the cuts, it is indicated with N/A. The uncertainties are statistical uncertainties.

| eee CHANNEL | data | | WZ simulations | |
|-------------------------|------------------|--------|---------------------|--------|
| | Efficiency | unc. | Efficiency | unc. |
| 3 lep, at least one jet | 20/21 = 95.24% | 29.76% | 2211/2215 = 99.82 % | 3.00% |
| STS R | 4/4 = 100.00% | 70.71% | 176/176 = 100.00% | 10.66% |
| TTS R | 2/3 = 66.67% | 60.86% | 242/242 = 100.00% | 9.09% |
| WZCR | 14/14 = 100.00 % | 37.80% | 1744/1748=99.77% | 3.38% |

Table A.4: Trigger efficiencies on data events selected with E_T^{miss} triggers and WZ simulation for ee μ leptonic channel together. The unweighted number of events is quoted. When there are no events passing the cuts, it is indicated with N/A. The uncertainties are statistical uncertainties.

| ee μ CHANNEL | data | | WZ simulations | |
|-------------------------|------------------|---------|--------------------|-------|
| | Efficiency | unc. | Efficiency | unc. |
| 3 lep, at least one jet | 32/32 = 100.00 % | 25.00 % | 3116/3118 = 99.94% | 2.53% |
| STS R | 1/1 = 100.00% | 141.42% | 255/255 = 100% | 8.86% |
| TTS R | 9/9 = 100.00% | 47.14% | 291/291 = 100.00% | 8.29% |
| WZCR | 14/14 = 100.00 % | 37.80% | 2529/2531=99.92% | 2.81% |

Table A.5: Trigger efficiencies on data events selected with E_T^{miss} triggers and WZ simulation for e $\mu\mu$ leptonic channel together. The unweighted number of events is quoted. When there are no events passing the cuts, it is indicated with N/A. The uncertainties are statistical uncertainties.

| e $\mu\mu$ CHANNEL | data | | WZ simulations | |
|-------------------------|------------------|---------|---------------------|-------|
| | Efficiency | unc. | Efficiency | unc. |
| 3 lep, at least one jet | 25/25 = 100.00% | 28.28% | 4906/4908 = 99.96 % | 2.02% |
| STS R | 1/1 = 100.00% | 141.42% | 423/423 = 100.00% | 6.88% |
| TTS R | 2/2 = 100.00% | 100.00% | 495/496 = 99.80% | 6.34% |
| WZCR | 19/19 = 100.00 % | 32.44% | 3894/3895 =99.97% | 2.27% |

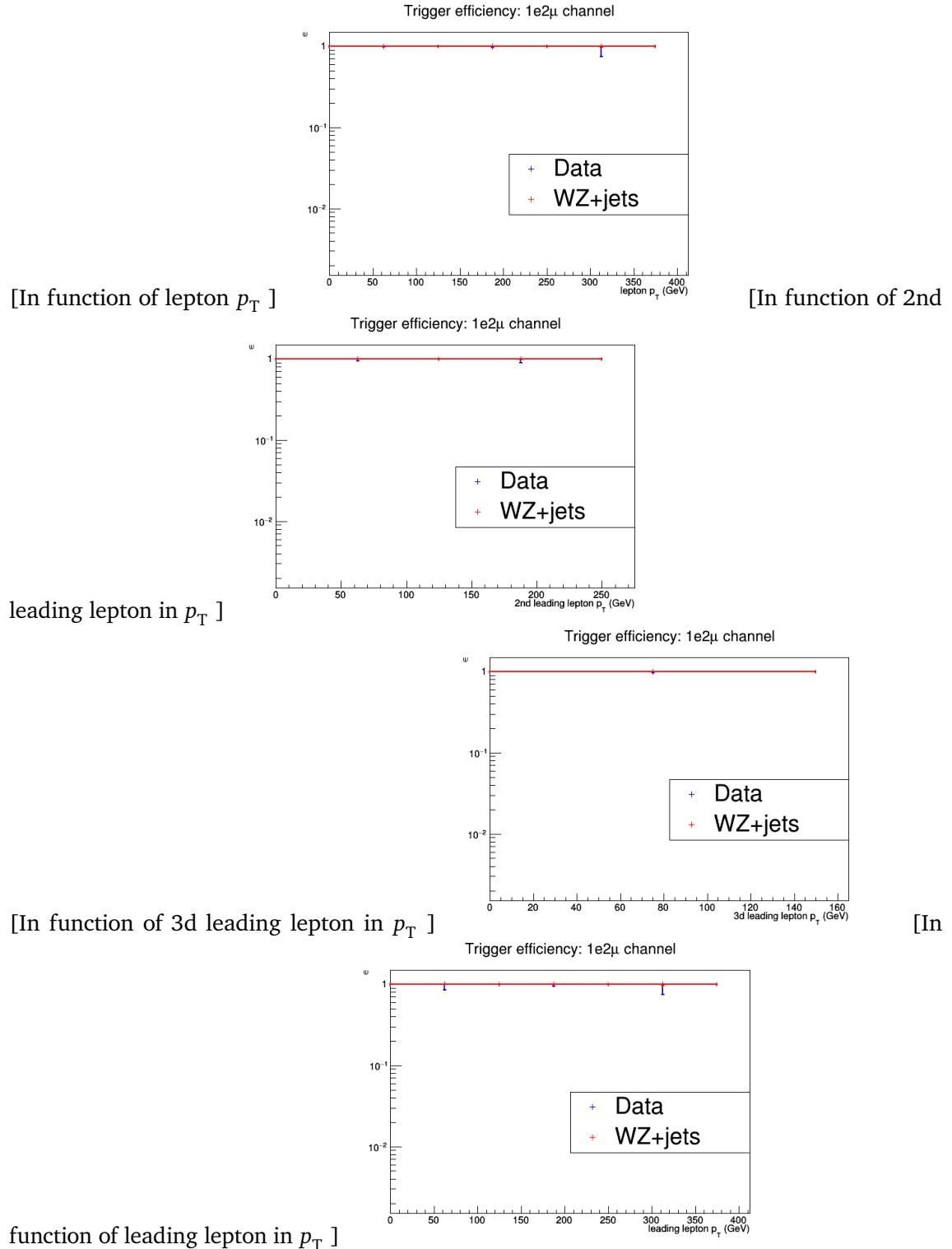


Figure A.1: The trigger efficiencies measured as a function of lepton p_T , using the dataset collected by E_T^{miss} triggers and WZ simulation, after a 3 lepton and jets selection, in the Z mass window. All corrections to simulation are applied. 1e2μ channel.

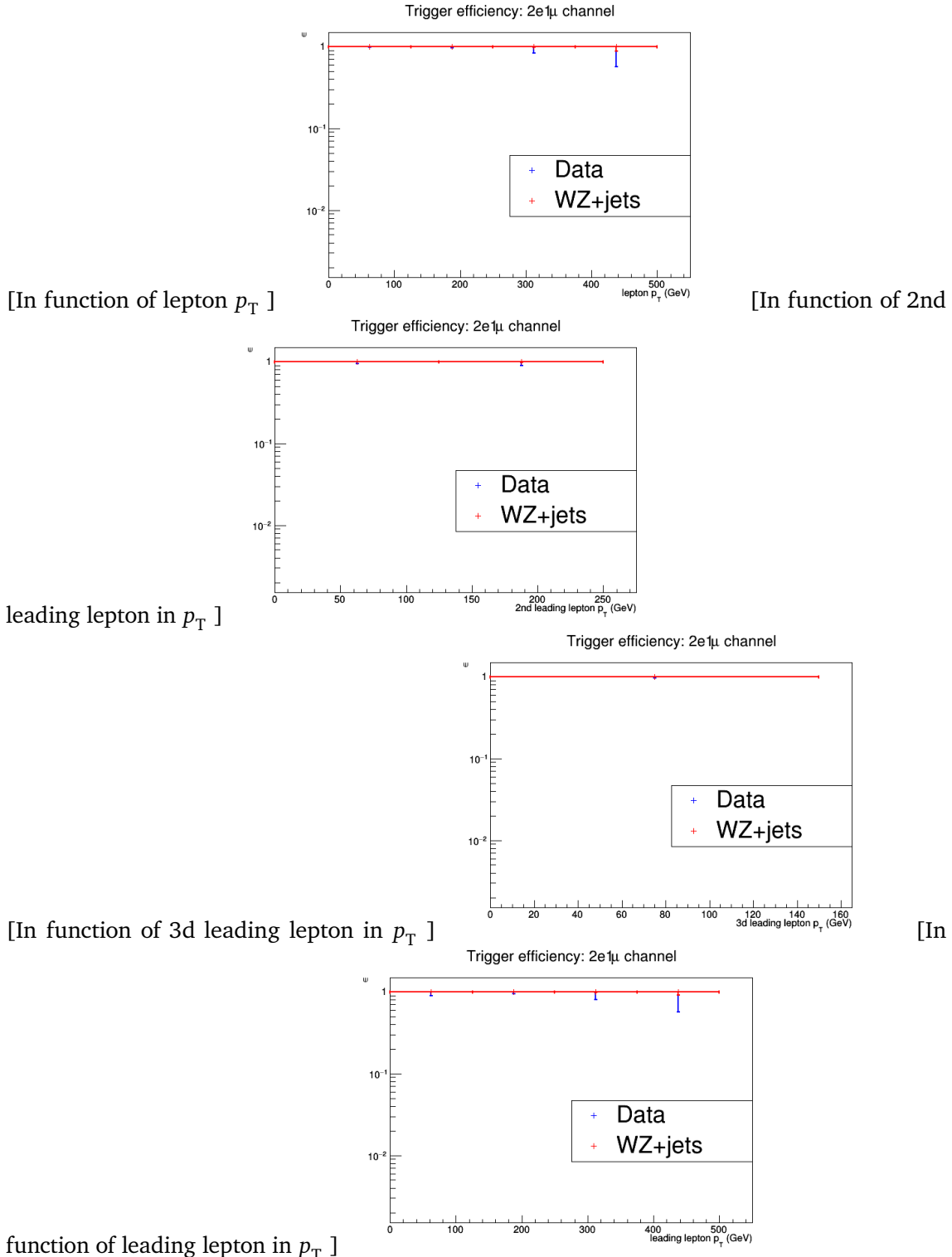


Figure A.2: The trigger efficiencies measured as a function of lepton p_T , using the dataset collected by E_T^{miss} triggers and WZ simulation, after a 3 lepton and jets selection, in the Z mass window. All corrections to simulation are applied. 2e1μ channel.

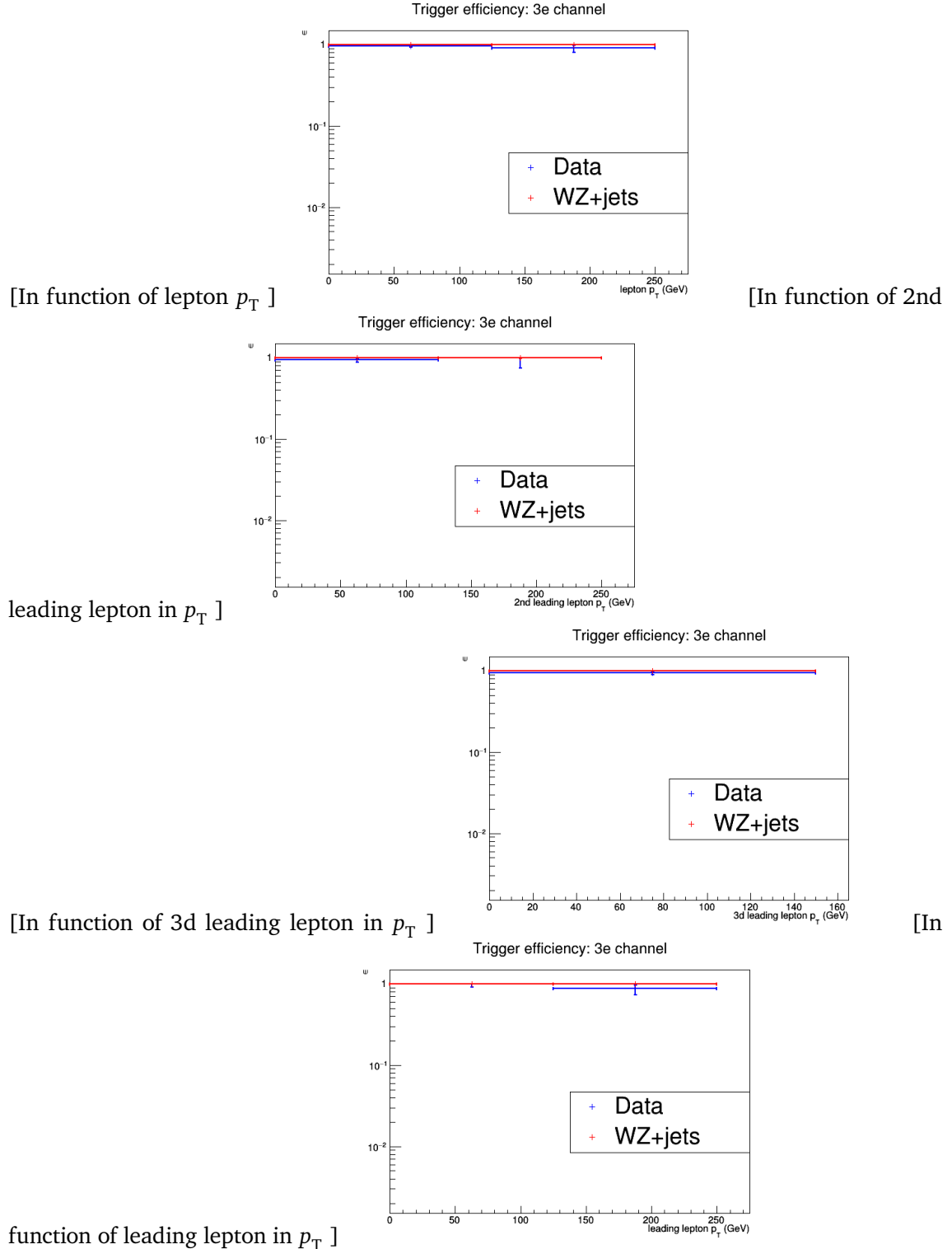


Figure A.3: The trigger efficiencies measured as a function of lepton p_T , using the dataset collected by E_T^{miss} triggers and WZ simulation, after a 3 lepton and jets selection, in the Z mass window. All corrections to simulation are applied. 3e channel.

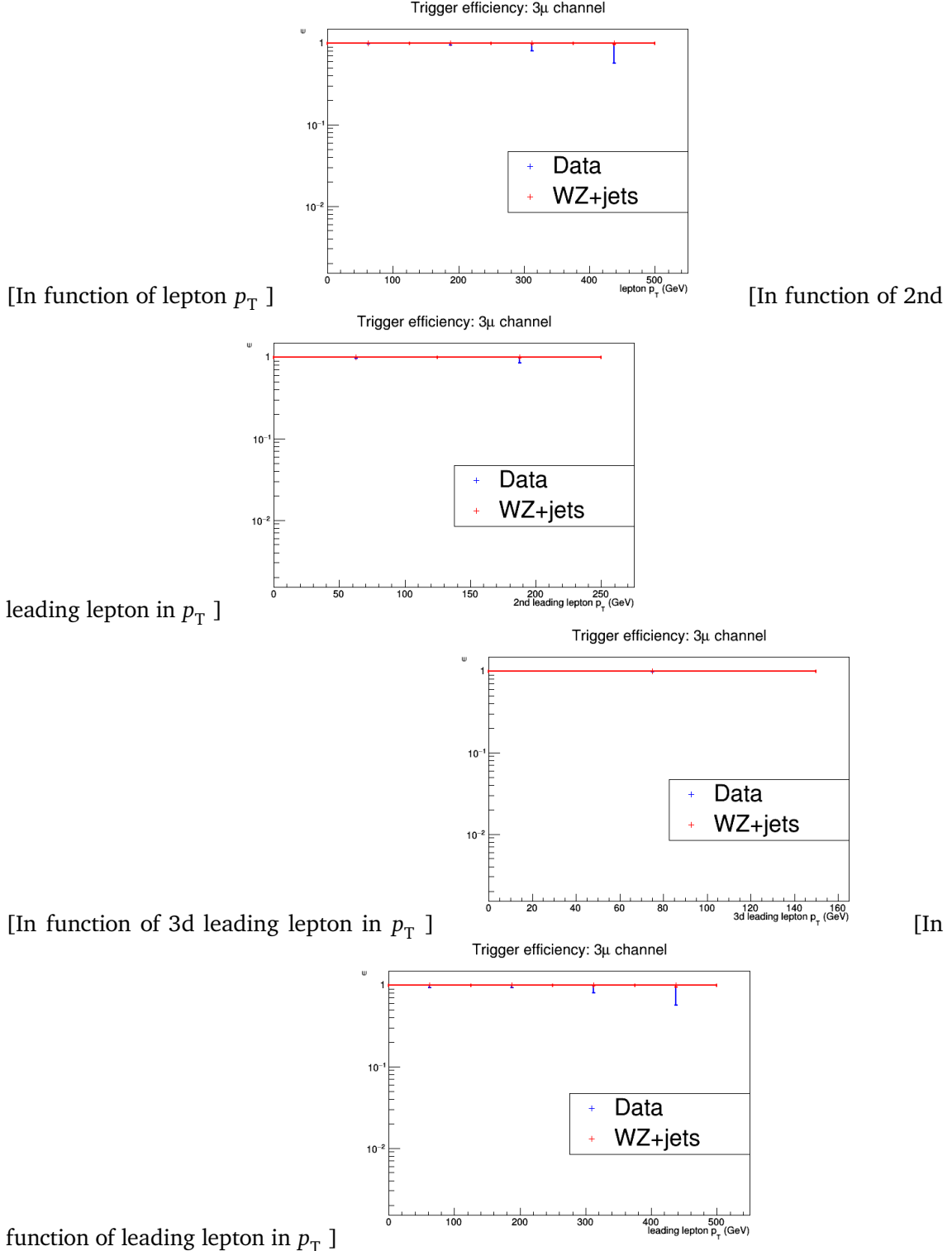


Figure A.4: The trigger efficiencies measured as a function of lepton p_T , using the dataset collected by E_T^{miss} triggers and WZ simulation, after a 3 lepton and jets selection, in the Z mass window. All corrections to simulation are applied. 3μ channel.

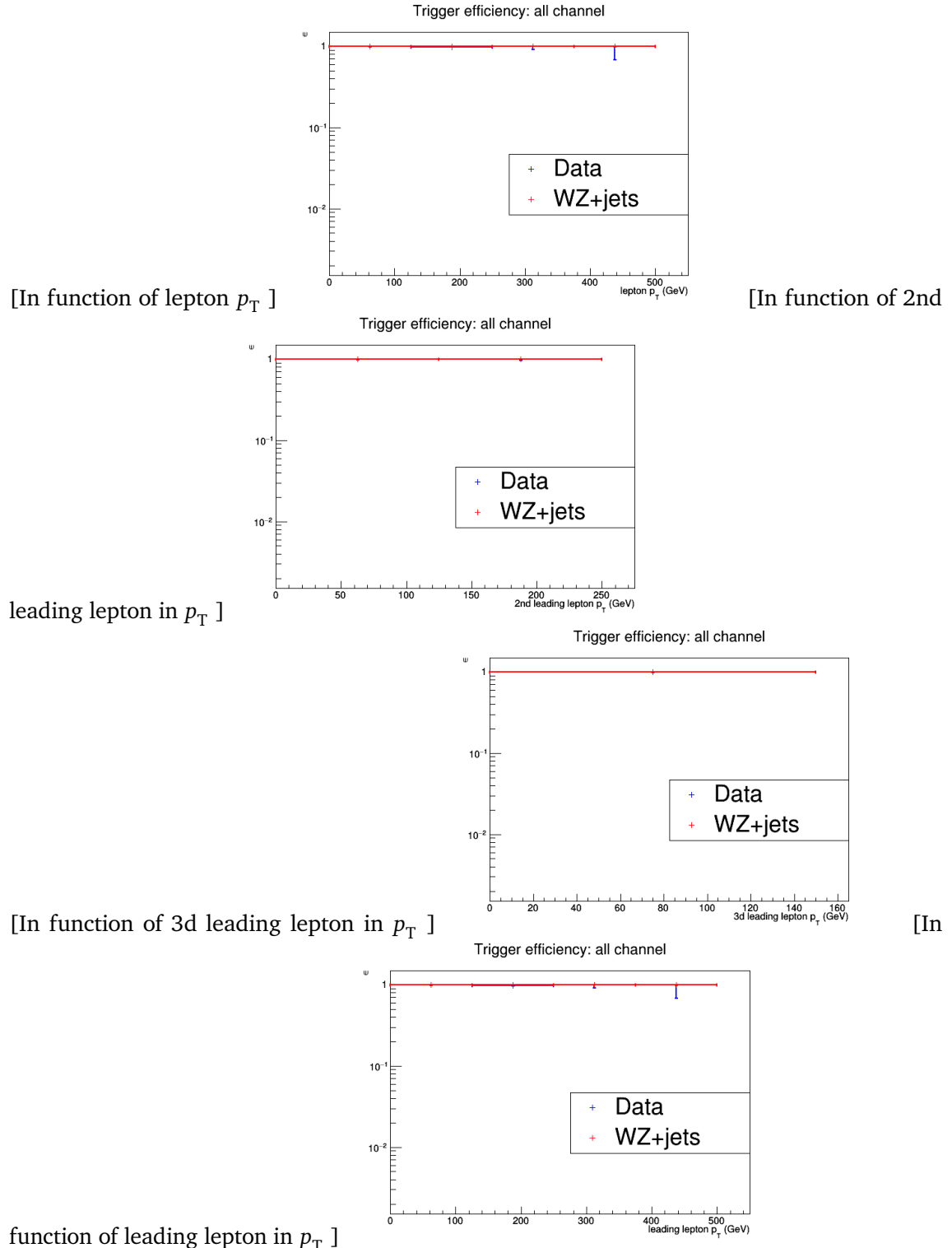


Figure A.5: The trigger efficiencies measured as a function of lepton p_T , using the dataset collected by E_T^{miss} triggers and WZ simulation, after a 3 lepton and jets selection, in the Z mass window. All corrections to simulation are applied. All channel.

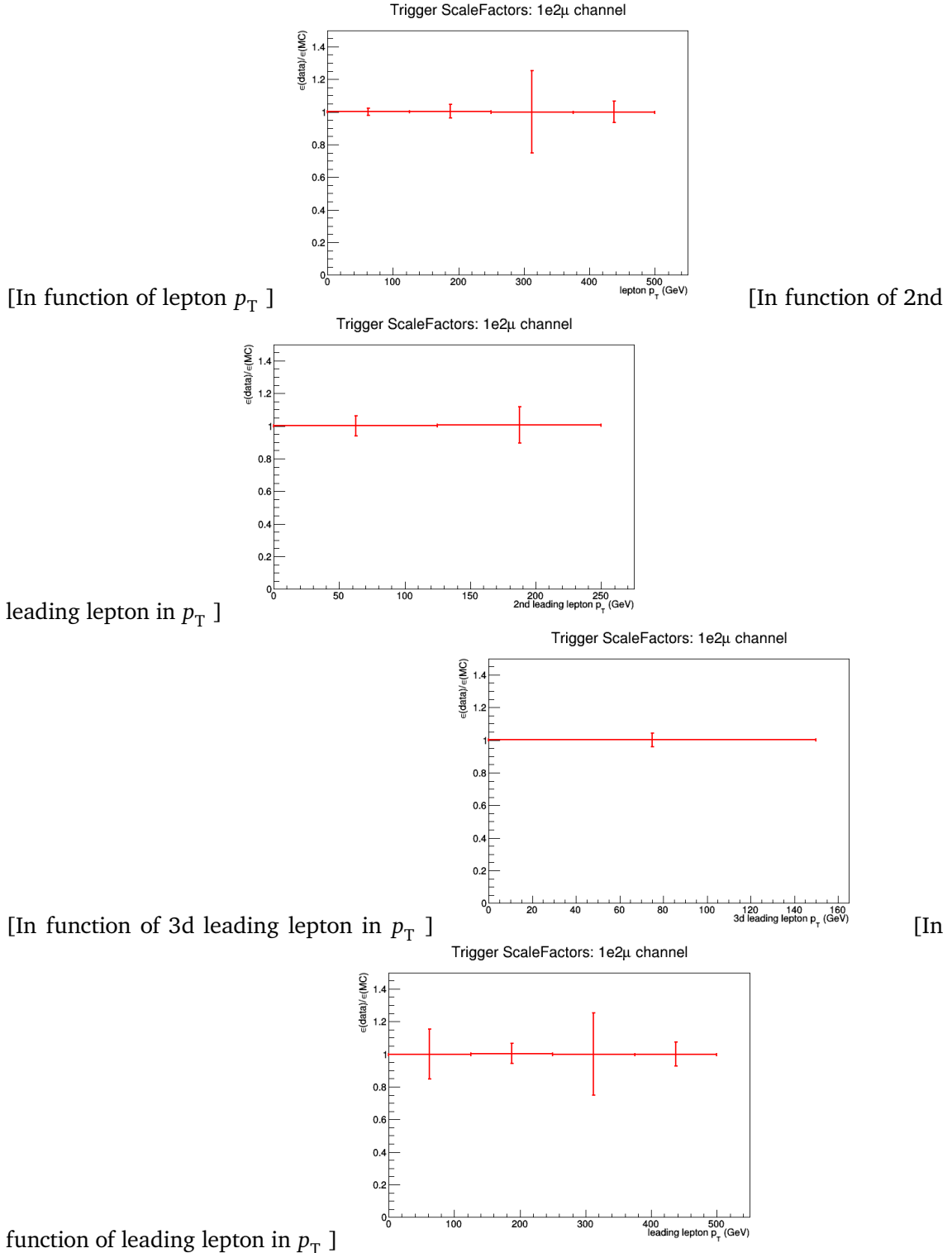


Figure A.6: The trigger scale factors measured as a function of lepton p_T , using the dataset collected by E_T^{miss} triggers and WZ simulation, after a 3 lepton and jets selection, in the Z mass window. All corrections to simulation are applied. 1e2μ channel.

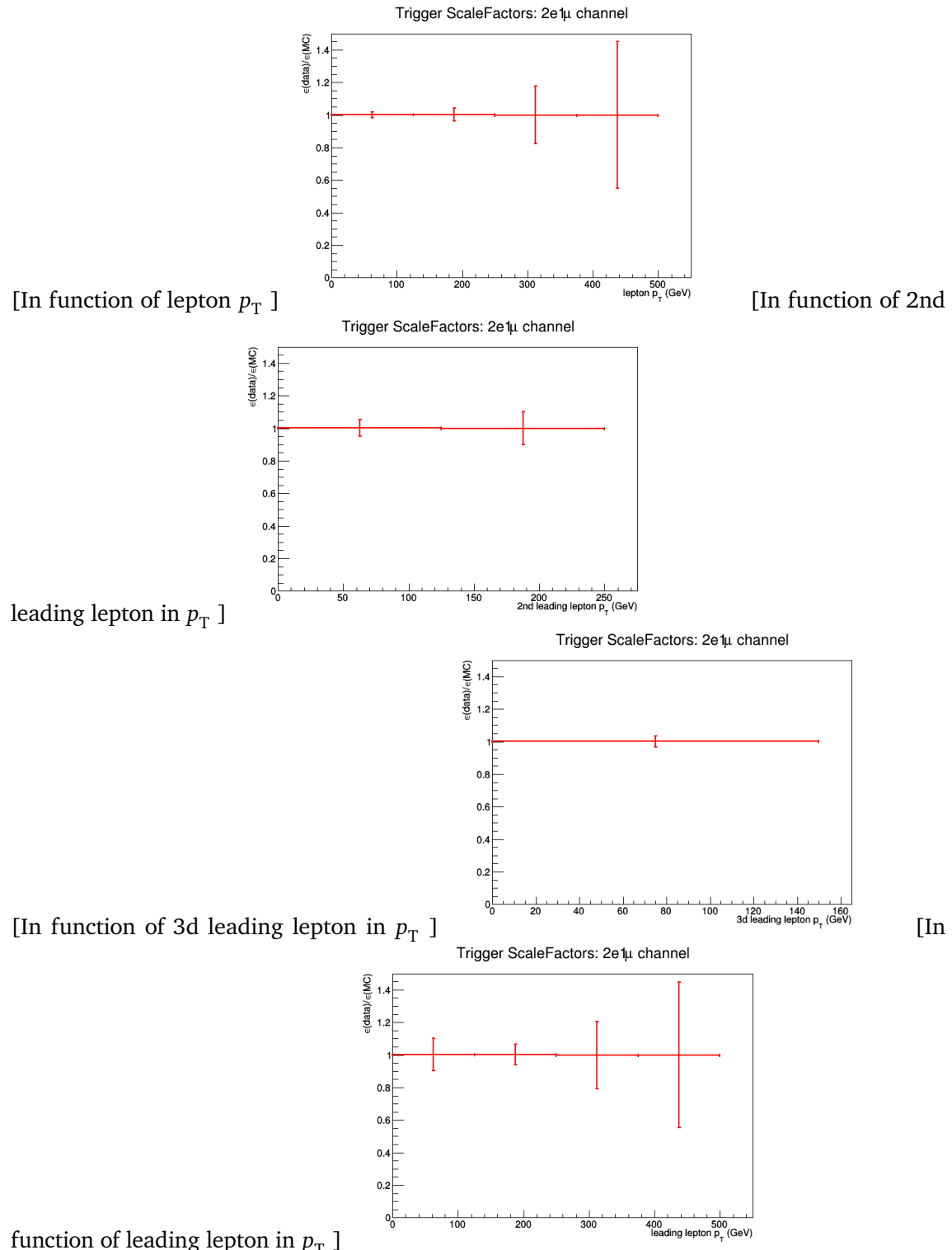


Figure A.7: The trigger scale factors measured as a function of lepton p_T , using the dataset collected by E_T^{miss} triggers and WZ simulation, after a 3 lepton and jets selection, in the Z mass window. All corrections to simulation are applied. 2e1μ channel.

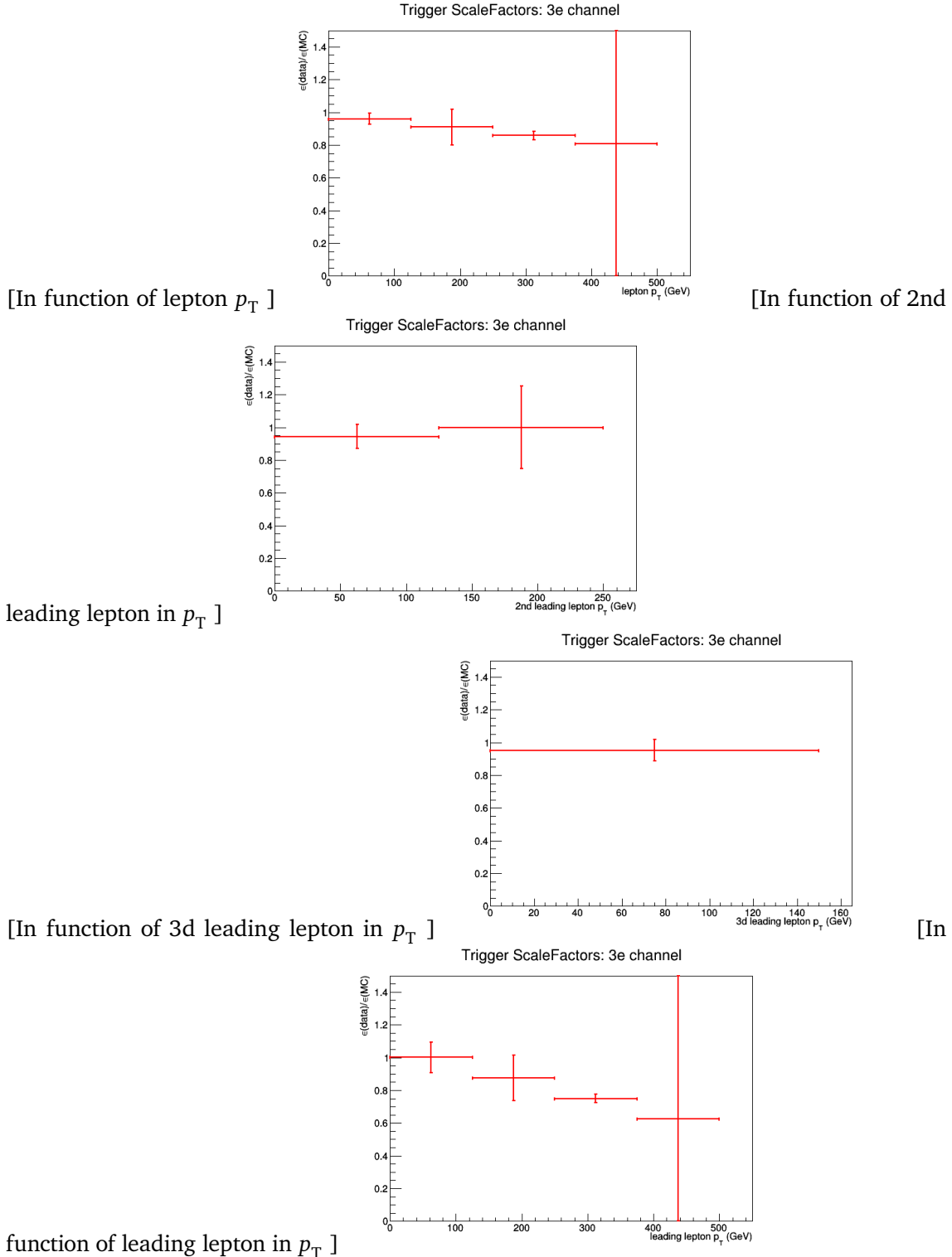


Figure A.8: The trigger scale factors measured as a function of lepton p_T , using the dataset collected by E_T^{miss} triggers and WZ simulation, after a 3 lepton and jets selection, in the Z mass window. All corrections to simulation are applied. 3e channel.

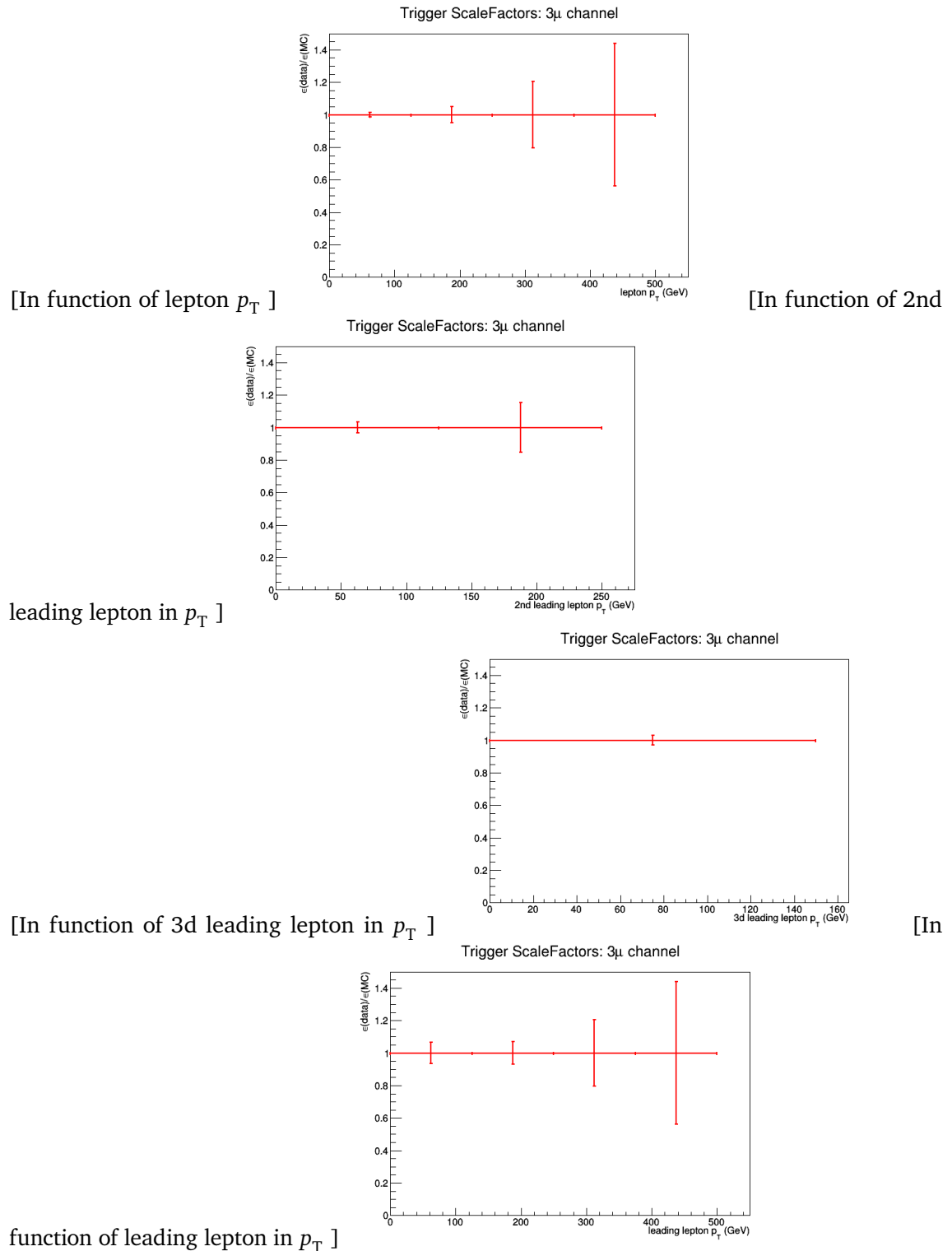


Figure A.9: The trigger scale factors measured as a function of lepton p_T , using the dataset collected by E_T^{miss} triggers and WZ simulation, after a 3 lepton and jets selection, in the Z mass window. All corrections to simulation are applied. 3μ channel.

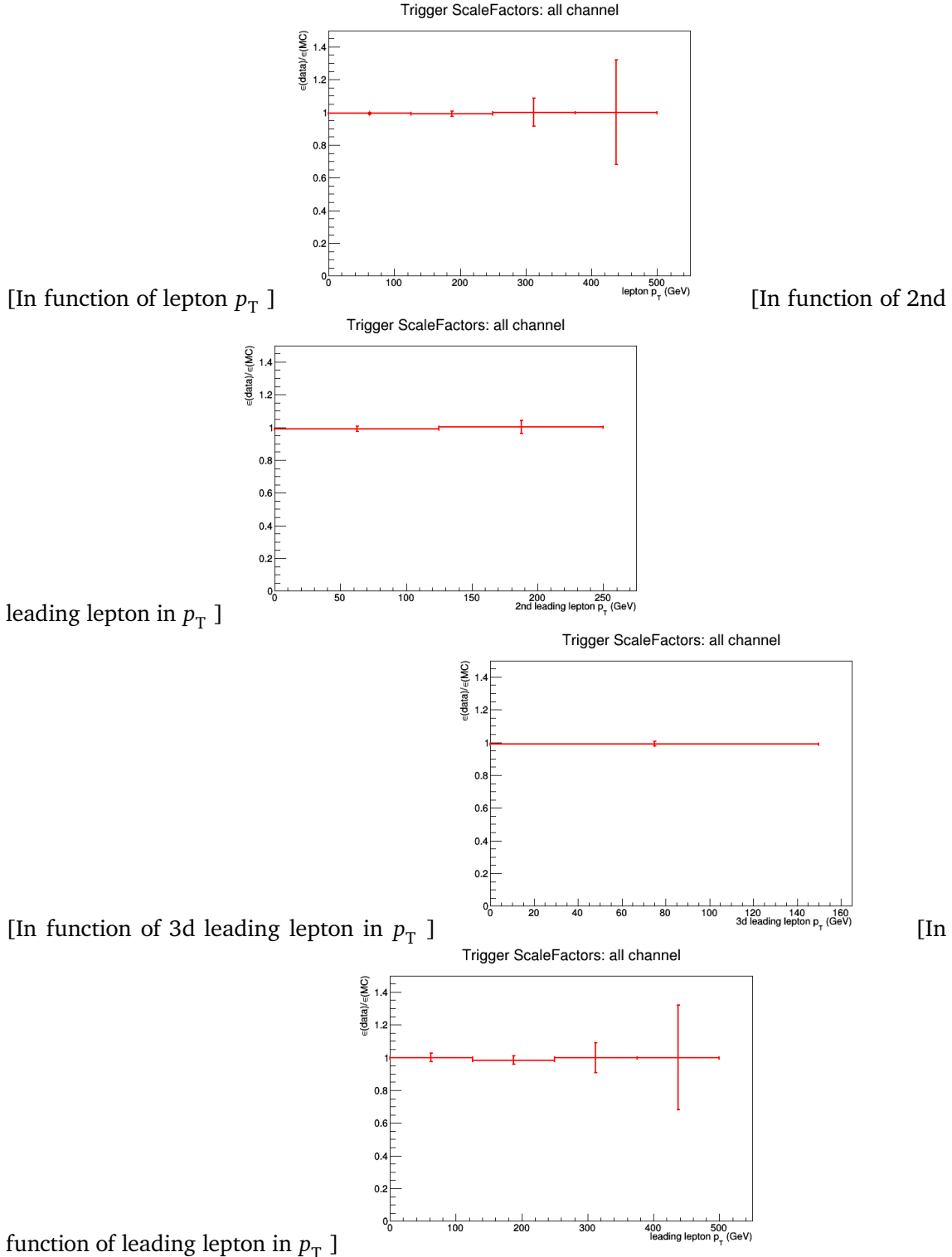


Figure A.10: The trigger scale factors measured as a function of lepton p_T , using the dataset collected by E_T^{miss} triggers and WZ simulation, after a 3 lepton and jets selection, in the Z mass window. All corrections to simulation are applied. All channel.

Dilepton controlplots

B

Statistical independent regions

1713

C

Bibliography

- 1715 [1] MICHAEL E PESKIN and DANIEL V SCHROEDER: **An introduction to quantum field**
 1716 **theory; 1995 ed.** Includes exercises. Boulder, CO: Westview, 1995. URL: <https://cds.cern.ch/record/257493> (see pp. 1, 5).
- 1718 [2] C. P. BURGESS: **Introduction to Effective Field Theory**. In: *Ann. Rev. Nucl. Part. Sci.*, **57**: (2007), pp. 329–362. DOI: [10.1146/annurev.nucl.56.080805.140508](https://doi.org/10.1146/annurev.nucl.56.080805.140508). arXiv: [hep-th/0701053 \[hep-th\]](https://arxiv.org/abs/hep-th/0701053) (see p. 1).
- 1721 [3] NADIA ROBOTTI: **The discovery of the electron: I**. In: *European Journal of Physics*,
 1722 **18**:3 (1997), p. 133. URL: <http://stacks.iop.org/0143-0807/18/i=3/a=002> (see p. 2).
- 1723 [4] Y. FUKUDA et al.: **Evidence for oscillation of atmospheric neutrinos**. In: *Phys. Rev. Lett.*, **81**: (1998), pp. 1562–1567. DOI: [10.1103/PhysRevLett.81.1562](https://doi.org/10.1103/PhysRevLett.81.1562). arXiv: [hep-ex/9807003 \[hep-ex\]](https://arxiv.org/abs/hep-ex/9807003) (see pp. 2, 13).
- 1726 [5] Y. ABE et al.: **Indication of Reactor $\bar{\nu}_e$ Disappearance in the Double Chooz Experiment**. In: *Phys. Rev. Lett.*, **108**: (13 Mar. 2012), p. 131801. DOI: [10.1103/PhysRevLett.108.131801](https://doi.org/10.1103/PhysRevLett.108.131801) (see pp. 2, 13).
- 1729 [6] C. PATRIGNANI et al.: **Review of Particle Physics**. In: *Chin. Phys.*, **C40**:10 (2016),
 1730 p. 100001. DOI: [10.1088/1674-1137/40/10/100001](https://doi.org/10.1088/1674-1137/40/10/100001) (see pp. 2–3, 6–9, 38–39, 69).
- 1731 [7] S. ABACHI et al.: **Observation of the top quark**. In: *Phys. Rev. Lett.*, **74**: (1995),
 1732 pp. 2632–2637. DOI: [10.1103/PhysRevLett.74.2632](https://doi.org/10.1103/PhysRevLett.74.2632). arXiv: [hep-ex/9503003 \[hep-ex\]](https://arxiv.org/abs/hep-ex/9503003)
 1733 (see p. 2).
- 1734 [8] F. ABE et al.: **Observation of top quark production in $\bar{p}p$ collisions**. In: *Phys. Rev. Lett.*, **74**: (1995), pp. 2626–2631. DOI: [10.1103/PhysRevLett.74.2626](https://doi.org/10.1103/PhysRevLett.74.2626). arXiv: [hep-ex/9503002 \[hep-ex\]](https://arxiv.org/abs/hep-ex/9503002) (see p. 2).
- 1737 [9] **First combination of Tevatron and LHC measurements of the top-quark mass**. In:
 1738 (2014). arXiv: [1403.4427 \[hep-ex\]](https://arxiv.org/abs/1403.4427) (see p. 2).
- 1739 [10] SERGUEI CHATRCHYAN et al.: **Observation of a new boson at a mass of 125 GeV**
 1740 **with the CMS experiment at the LHC**. In: *Phys. Lett.*, **B716**: (2012), pp. 30–61. DOI:
 1741 [10.1016/j.physletb.2012.08.021](https://doi.org/10.1016/j.physletb.2012.08.021). arXiv: [1207.7235 \[hep-ex\]](https://arxiv.org/abs/1207.7235) (see pp. 2, 19).
- 1742 [11] GEORGES AAD et al.: **Observation of a new particle in the search for the Standard**
 1743 **Model Higgs boson with the ATLAS detector at the LHC**. In: *Phys. Lett.*, **B716**:
 1744 (2012), pp. 1–29. DOI: [10.1016/j.physletb.2012.08.020](https://doi.org/10.1016/j.physletb.2012.08.020). arXiv: [1207.7214 \[hep-ex\]](https://arxiv.org/abs/1207.7214)
 1745 (see pp. 2, 19).

- 1746 [12] NICOLA CABIBBO: **Unitary Symmetry and Leptonic Decays**. In: *Phys. Rev. Lett.*, **10**:
 1747 (12 June 1963), pp. 531–533. doi: [10.1103/PhysRevLett.10.531](https://doi.org/10.1103/PhysRevLett.10.531) (see p. 5).
- 1748 [13] S. L. GLASHOW, J. ILIOPoulos, and L. MAIANI: **Weak Interactions with Lepton-Hadron
 1749 Symmetry**. In: *Phys. Rev. D*, **2**: (7 Oct. 1970), pp. 1285–1292. doi: [10.1103/PhysRevD.2.1285](https://doi.org/10.1103/PhysRevD.2.1285) (see p. 5).
- 1750 [14] B.J. BJØRKEN and S.L. GLASHOW: **Elementary particles and SU(4)**. In: *Physics Letters*,
 1751 **11**:3 (1964), pp. 255–257. doi: [https://doi.org/10.1016/0031-9163\(64\)90433-0](https://doi.org/10.1016/0031-9163(64)90433-0) (see
 1752 p. 5).
- 1753 [15] LUCIANO MAIANI: **The GIM Mechanism: origin, predictions and recent uses**. In:
 1754 *Proceedings, 48th Rencontres de Moriond on Electroweak Interactions and Unified Theories:
 1755 La Thuile, Italy, March 2-9, 2013*. 2013, pp. 3–16. arXiv: [1303.6154 \[hep-ph\]](https://arxiv.org/abs/1303.6154). URL:
 1756 <https://inspirehep.net/record/1225307/files/arXiv:1303.6154.pdf> (see p. 5).
- 1757 [16] PATRICK KOPPENBURG and SEBASTIEN DESCOTES-GENON: **The CKM Parameters**. In:
 1758 (2017). arXiv: [1702.08834 \[hep-ex\]](https://arxiv.org/abs/1702.08834) (see p. 6).
- 1759 [17] J. A. AGUILAR-SAAVEDRA: **Top flavor-changing neutral interactions: Theoretical
 1760 expectations and experimental detection**. In: *Acta Phys. Polon.*, **B35**: (2004),
 1761 pp. 2695–2710. arXiv: [hep-ph/0409342 \[hep-ph\]](https://arxiv.org/abs/hep-ph/0409342) (see pp. 6, 14–15).
- 1762 [18] S. ABACHI et al.: **Observation of the top quark**. In: *Phys. Rev. Lett.*, **74**: (1995),
 1763 pp. 2632–2637. doi: [10.1103/PhysRevLett.74.2632](https://doi.org/10.1103/PhysRevLett.74.2632). arXiv: [hep-ex/9503003 \[hep-ex\]](https://arxiv.org/abs/hep-ex/9503003)
 1764 (see p. 6).
- 1765 [19] F. ABE et al.: **Observation of top quark production in $\bar{p}p$ collisions**. In: *Phys. Rev.
 1766 Lett.*, **74**: (1995), pp. 2626–2631. doi: [10.1103/PhysRevLett.74.2626](https://doi.org/10.1103/PhysRevLett.74.2626). arXiv: [hep-ex/9503002 \[hep-ex\]](https://arxiv.org/abs/hep-ex/9503002) (see p. 6).
- 1767 [20] ANDREA GIAMMANCO and JEANNINE WAGNER-KUHR: **Measurement of the t-channel
 1768 single Top-quark production rates in pp collisions at 7 TeV**. 2011. URL: <http://cms.web.cern.ch/news/measurement-t-channel-single-top-quark-production-rates-pp-collisions-7-tev> (see p. 8).
- 1769 [21] LHCTOP WORKING GROUP: **ATLAS-CMS recommended predictions for single top
 1770 cross sections using the Hathor v2.1 program**. 2017. URL: https://twiki.cern.ch/twiki/bin/view/LHCPhysics/SingleTopRefXsec#Predictions_at_7_8_13_and_14_TeV
 1771 (see p. 9).
- 1772 [22] CMS COLLABORATION: **Summaries of CMS cross section measurements**. 2017. URL:
 1773 <https://twiki.cern.ch/twiki/bin/view/CMSPublic/PhysicsResultsCombined> (see
 1774 pp. 10, 17–18).
- 1775 [23] LHCTOP WORKING GROUP: **LHCTopWG Summary plots**. 2017. URL: <https://twiki.cern.ch/twiki/bin/view/LHCPhysics/LHCTopWGSummaryPlots> (see pp. 11–12).
- 1776 [24] B. GRZADKOWSKI, M. ISKRZYNSKI, M. MISIAK, and J. ROSIEK: **Dimension-Six Terms
 1777 in the Standard Model Lagrangian**. In: *JHEP*, **10**: (2010), p. 085. doi: [10.1007/JHEP10\(2010\)085](https://doi.org/10.1007/JHEP10(2010)085). arXiv: [1008.4884 \[hep-ph\]](https://arxiv.org/abs/1008.4884) (see p. 12).
- 1778 [25] ANDY BUCKLEY, CHRISTOPH ENGLERT, JAMES FERRANDO, et al.: **Constraining top
 1779 quark effective theory in the LHC Run II era**. In: *JHEP*, **04**: (2016), p. 015. doi:
 1780 [10.1007/JHEP04\(2016\)015](https://doi.org/10.1007/JHEP04(2016)015). arXiv: [1512.03360 \[hep-ph\]](https://arxiv.org/abs/1512.03360) (see p. 12).
- 1781
- 1782
- 1783
- 1784
- 1785
- 1786
- 1787

- 1788 [26] P. A. R. ADE et al.: **Planck 2015 results. XIII. Cosmological parameters.** In: *Astron.*
 1789 *Astrophys.*, **594**: (2016), A13. doi: [10.1051/0004-6361/201525830](https://doi.org/10.1051/0004-6361/201525830). arXiv: [1502.01589](https://arxiv.org/abs/1502.01589)
 1790 [[astro-ph.CO](#)] (see p. 13).
- 1791 [27] P. J. E. PEEBLES and BHARAT RATRA: **The Cosmological constant and dark energy.**
 1792 In: *Rev. Mod. Phys.*, **75**: (2003), pp. 559–606. doi: [10.1103/RevModPhys.75.559](https://doi.org/10.1103/RevModPhys.75.559). arXiv:
 1793 [[astro-ph/0207347](#) [[astro-ph](#)]] (see p. 13).
- 1794 [28] A. D. SAKHAROV: **Violation of CP Invariance, c Asymmetry, and Baryon Asym-**
 1795 **metry of the Universe.** In: *Pisma Zh. Eksp. Teor. Fiz.*, **5**: (1967). [*Usp. Fiz.*
 1796 *Nauk* **161**, 61(1991)], pp. 32–35. doi: [10.1070/PU1991v034n05ABEH002497](https://doi.org/10.1070/PU1991v034n05ABEH002497) (see p. 13).
- 1797 [29] GUSTAVO BURDMAN: **New solutions to the hierarchy problem.** In: *Braz. J. Phys.*, **37**:
 1798 (2007), pp. 506–513. doi: [10.1590/S0103-97332007000400006](https://doi.org/10.1590/S0103-97332007000400006). arXiv: [hep-ph/0703194](https://arxiv.org/abs/hep-ph/0703194)
 1799 [[hep-ph](#)] (see p. 13).
- 1800 [30] T. ET AL. AALTONEN: **Search for the Flavor-Changing Neutral-Current Decay $t \rightarrow Zq$**
 1801 **in $p\bar{p}$ Collisions at $\sqrt{s} = 1.96$ TeV.** In: *Phys. Rev. Lett.*, **101**: (19 Nov. 2008),
 1802 p. 192002. doi: [10.1103/PhysRevLett.101.192002](https://doi.org/10.1103/PhysRevLett.101.192002) (see p. 14).
- 1803 [31] VICTOR MUKHAMEDOVICH ABAZOV et al.: **Search for flavour changing neutral cur-**
 1804 **rents via quark-gluon couplings in single top quark production using 2.3 fb^{-1} of**
 1805 **$p\bar{p}$ collisions.** In: *Phys. Lett.*, **B693**: (2010), pp. 81–87. doi: [10.1016/j.physletb.2010.08.011](https://doi.org/10.1016/j.physletb.2010.08.011). arXiv: [1006.3575](https://arxiv.org/abs/1006.3575) [[hep-ex](#)] (see p. 14).
- 1807 [32] GEORGES AAD et al.: **Search for flavour-changing neutral current top-quark decays**
 1808 **to qZ in pp collision data collected with the ATLAS detector at $\sqrt{s} = 8$ TeV.** In: *Eur. Phys. J.*, **C76**:1 (2016), p. 12. doi: [10.1140/epjc/s10052-015-3851-5](https://doi.org/10.1140/epjc/s10052-015-3851-5). arXiv:
 1810 [1508.05796](https://arxiv.org/abs/1508.05796) [[hep-ex](#)] (see p. 14).
- 1811 [33] GEORGES AAD et al.: **Search for single top-quark production via flavour-changing**
 1812 **neutral currents at 8 TeV with the ATLAS detector.** In: *Eur. Phys. J.*, **C76**:2 (2016),
 1813 p. 55. doi: [10.1140/epjc/s10052-016-3876-4](https://doi.org/10.1140/epjc/s10052-016-3876-4). arXiv: [1509.00294](https://arxiv.org/abs/1509.00294) [[hep-ex](#)] (see pp. 14,
 1814 17).
- 1815 [34] GEORGES AAD et al.: **Search for flavour-changing neutral current top quark decays**
 1816 **$t \rightarrow Hq$ in pp collisions at $\sqrt{s} = 8$ TeV with the ATLAS detector.** In: *JHEP*, **12**:
 1817 (2015), p. 061. doi: [10.1007/JHEP12\(2015\)061](https://doi.org/10.1007/JHEP12(2015)061). arXiv: [1509.06047](https://arxiv.org/abs/1509.06047) [[hep-ex](#)] (see
 1818 p. 14).
- 1819 [35] MORAD AABOUD et al.: **Search for top quark decays $t \rightarrow qH$, with $H \rightarrow \gamma\gamma$, in**
 1820 **$\sqrt{s} = 13$ TeV pp collisions using the ATLAS detector.** In: (2017). arXiv: [1707.01404](https://arxiv.org/abs/1707.01404)
 1821 [[hep-ex](#)] (see pp. 14, 17).
- 1822 [36] **Search for flavour-changing neutral current top quark decays $t \rightarrow qZ$ in proton-**
 1823 **proton collisions at $\sqrt{s} = 13$ TeV with the ATLAS Detector.** Tech. rep. ATLAS-CONF-
 1824 2017-070. Geneva: CERN, Sept. 2017. URL: <https://cds.cern.ch/record/2285808>
 1825 (see pp. 14, 17).
- 1826 [37] ALBERT M SIRUNYAN et al.: **Search for associated production of a Z boson with a**
 1827 **single top quark and for tZ flavour-changing interactions in pp collisions at \sqrt{s}**
 1828 **= 8 TeV.** In: (2017). arXiv: [1702.01404](https://arxiv.org/abs/1702.01404) [[hep-ex](#)] (see pp. 14, 16).

- 1829 [38] SERGUEI CHATRCHYAN et al.: **Search for Flavor-Changing Neutral Currents in Top-**
 1830 **Quark Decays $t \rightarrow Zq$ in pp Collisions at $\sqrt{s} = 8\text{TeV}$** . In: *Phys. Rev. Lett.*, **112**:17
 1831 (2014), p. 171802. DOI: [10.1103/PhysRevLett.112.171802](https://doi.org/10.1103/PhysRevLett.112.171802). arXiv: [1312.4194](https://arxiv.org/abs/1312.4194) [hep-ex]
 1832 (see p. 14).
- 1833 [39] VARDAN KHACHATRYAN et al.: **Search for anomalous single top quark production in**
 1834 **association with a photon in pp collisions at $\sqrt{s} = 8\text{ TeV}$** . In: *JHEP*, **04**: (2016),
 1835 p. 035. DOI: [10.1007/JHEP04\(2016\)035](https://doi.org/10.1007/JHEP04(2016)035). arXiv: [1511.03951](https://arxiv.org/abs/1511.03951) [hep-ex] (see pp. 14, 17).
- 1836 [40] VARDAN KHACHATRYAN et al.: **Search for top quark decays via Higgs-boson-mediated**
 1837 **flavor-changing neutral currents in pp collisions at $\sqrt{s} = 8\text{ TeV}$** . In: *JHEP*, **02**:
 1838 (2017), p. 079. DOI: [10.1007/JHEP02\(2017\)079](https://doi.org/10.1007/JHEP02(2017)079). arXiv: [1610.04857](https://arxiv.org/abs/1610.04857) [hep-ex] (see
 1839 p. 14).
- 1840 [41] **Search for the flavor-changing interactions of the top quark with the Higgs boson**
 1841 **in $H \rightarrow b\bar{b}$ channel at $\sqrt{s} = 13\text{ TeV}$** . Tech. rep. CMS-PAS-TOP-17-003. Geneva:
 1842 CERN, 2017. URL: <https://cds.cern.ch/record/2284743> (see p. 14).
- 1843 [42] J. A. AGUILAR-SAAVEDRA: **A Minimal set of top anomalous couplings**. In: *Nucl. Phys.*,
 1844 **B812**: (2009), pp. 181–204. DOI: [10.1016/j.nuclphysb.2008.12.012](https://doi.org/10.1016/j.nuclphysb.2008.12.012). arXiv: [0811.3842](https://arxiv.org/abs/0811.3842)
 1845 [hep-ph] (see p. 14).
- 1846 [43] J. A. AGUILAR-SAAVEDRA: **A Minimal set of top-Higgs anomalous couplings**. In: *Nucl.*
 1847 *Phys.*, **B821**: (2009), pp. 215–227. DOI: [10.1016/j.nuclphysb.2009.06.022](https://doi.org/10.1016/j.nuclphysb.2009.06.022). arXiv:
 1848 [0904.2387](https://arxiv.org/abs/0904.2387) [hep-ph] (see p. 14).
- 1849 [44] M. BENEKE et al.: **Top quark physics**. In: *1999 CERN Workshop on standard model*
 1850 *physics (and more) at the LHC, CERN, Geneva, Switzerland, 25-26 May: Proceedings*.
 1851 2000, pp. 419–529. arXiv: [hep-ph/0003033](https://arxiv.org/abs/hep-ph/0003033) [hep-ph]. URL: <http://weblib.cern.ch/abstract?CERN-TH-2000-100> (see p. 15).
- 1853 [45] JUN GAO, CHONG SHENG LI, and HUA XING ZHU: **Top Quark Decay at Next-to-Next-**
 1854 **to Leading Order in QCD**. In: *Phys. Rev. Lett.*, **110**:4 (2013), p. 042001. DOI:
 1855 [10.1103/PhysRevLett.110.042001](https://doi.org/10.1103/PhysRevLett.110.042001). arXiv: [1210.2808](https://arxiv.org/abs/1210.2808) [hep-ph] (see p. 16).
- 1856 [46] STEPHEN MYERS: **The LEP Collider, from design to approval and commissioning**.
 1857 John Adams' Lecture. Delivered at CERN, 26 Nov 1990. Geneva: CERN, 1991. URL:
 1858 [http://cds.cern.ch/record/226776](https://cds.cern.ch/record/226776) (see p. 19).
- 1859 [47] STEPHEN HOLMES, RONALD S MOORE, and VLADIMIR SHILTSEV: **Overview of the**
 1860 **Tevatron collider complex: goals, operations and performance**. In: *Journal of In-*
 1861 *strumentation*, **6**:08 (2011), T08001. URL: <http://stacks.iop.org/1748-0221/6/i=08/a=T08001> (see p. 19).
- 1863 [48] R. BARATE et al.: **Search for the standard model Higgs boson at LEP**. In: *Phys.*
 1864 *Lett.*, **B565**: (2003), pp. 61–75. DOI: [10.1016/S0370-2693\(03\)00614-2](https://doi.org/10.1016/S0370-2693(03)00614-2). arXiv: [hep-ex/0306033](https://arxiv.org/abs/hep-ex/0306033) [hep-ex] (see p. 19).
- 1866 [49] KENNETH HERNER: **Higgs Boson Studies at the Tevatron**. In: *Nucl. Part. Phys. Proc.*,
 1867 **273-275**: (2016), pp. 852–856. DOI: [10.1016/j.nuclphysbps.2015.09.131](https://doi.org/10.1016/j.nuclphysbps.2015.09.131) (see p. 19).
- 1868 [50] ABDELHAK DJOUADI: **The Anatomy of electro-weak symmetry breaking. I: The**
 1869 **Higgs boson in the standard model**. In: *Phys. Rept.*, **457**: (2008), pp. 1–216. DOI:
 1870 [10.1016/j.physrep.2007.10.004](https://doi.org/10.1016/j.physrep.2007.10.004). arXiv: [hep-ph/0503172](https://arxiv.org/abs/hep-ph/0503172) [hep-ph] (see p. 19).

- 1871 [51] LYNDON EVANS and PHILIP BRYANT: **LHC Machine**. In: *Journal of Instrumentation*,
 1872 3:08 (2008), S08001. URL: <http://stacks.iop.org/1748-0221/3/i=08/a=S08001> (see
 1873 p. 19).
- 1874 [52] THOMAS SVEN PETTERSSON and P LEFÈVRE: **The Large Hadron Collider: conceptual
 1875 design**. Tech. rep. CERN-AC-95-05-LHC. Oct. 1995, p. 20 and 22. URL: <https://cds.cern.ch/record/291782> (see p. 19).
- 1877 [53] JORG WENNINGER and EZIO TODESCO: **Large Hadron Collider momentum calibration
 1878 and accuracy**. Tech. rep. CERN-ACC-2017-0007. Geneva: CERN, Feb. 2017. URL:
 1879 <https://cds.cern.ch/record/2254678> (see p. 20).
- 1880 [54] CINZIA DE MELIS: **The CERN accelerator complex. Complexe des accélérateurs du
 1881 CERN**. In: (July 2016). General Photo. URL: <https://cds.cern.ch/record/2197559>
 1882 (see p. 20).
- 1883 [55] OLIVER SIM BRÜNING, PAUL COLLIER, P LEBRUN, et al.: **LHC Design Report**. CERN
 1884 Yellow Reports: Monographs. Geneva: CERN, 2004. URL: <https://cds.cern.ch/record/782076> (see p. 20).
- 1886 [56] G. AAD et al.: **The ATLAS Experiment at the CERN Large Hadron Collider**. In: *JINST*,
 1887 3: (2008), S08003. DOI: [10.1088/1748-0221/3/08/S08003](https://doi.org/10.1088/1748-0221/3/08/S08003) (see p. 21).
- 1888 [57] S. CHATRCHYAN et al.: **The CMS Experiment at the CERN LHC**. In: *JINST*, 3: (2008),
 1889 S08004. DOI: [10.1088/1748-0221/3/08/S08004](https://doi.org/10.1088/1748-0221/3/08/S08004) (see pp. 21, 28–30).
- 1890 [58] K. AAMODT et al.: **The ALICE experiment at the CERN LHC**. In: *JINST*, 3: (2008),
 1891 S08002. DOI: [10.1088/1748-0221/3/08/S08002](https://doi.org/10.1088/1748-0221/3/08/S08002) (see p. 21).
- 1892 [59] A. AUGUSTO ALVES JR. et al.: **The LHCb Detector at the LHC**. In: *JINST*, 3: (2008),
 1893 S08005. DOI: [10.1088/1748-0221/3/08/S08005](https://doi.org/10.1088/1748-0221/3/08/S08005) (see p. 21).
- 1894 [60] M. BONGI et al.: **Astroparticle physics at LHC: The LHCf experiment ready for data
 1895 taking**. In: *Nucl. Instrum. Meth.*, A612: (2010), pp. 451–454. DOI: [10.1016/j.nima.2009.08.039](https://doi.org/10.1016/j.nima.2009.08.039) (see p. 21).
- 1897 [61] G. ANELLI et al.: **The TOTEM experiment at the CERN Large Hadron Collider**. In: *JINST*, 3: (2008), S08007. DOI: [10.1088/1748-0221/3/08/S08007](https://doi.org/10.1088/1748-0221/3/08/S08007) (see p. 21).
- 1899 [62] B. ACHARYA et al.: **The Physics Programme Of The MoEDAL Experiment At The LHC**.
 1900 In: *Int. J. Mod. Phys.*, A29: (2014), p. 1430050. DOI: [10.1142/S0217751X14300506](https://doi.org/10.1142/S0217751X14300506).
 1901 arXiv: [1405.7662 \[hep-ph\]](https://arxiv.org/abs/1405.7662) (see p. 21).
- 1902 [63] BY JAMES GILLIES: **Luminosity? Why don't we just say collision rate?** In: (Mar.
 1903 2011). URL: <http://cds.cern.ch/record/1997001> (see p. 21).
- 1904 [64] BY HARRIET JARLETT and HARRIET KIM JARLETT: **LHC pushes limits of performance**.
 1905 In: (Aug. 2016). URL: <http://cds.cern.ch/record/2212301> (see p. 22).
- 1906 [65] CMS COLLABORATION. 2017. URL: https://twiki.cern.ch/twiki/bin/view/CMSPublic/LumiPublicResults#Online_Luminosity_AN2 (see p. 22).
- 1908 [66] **Technical proposal**. LHC Tech. Proposal. Cover title : CMS, the Compact Muon
 1909 Solenoid : technical proposal. Geneva: CERN, 1994. URL: <https://cds.cern.ch/record/290969> (see p. 22).
- 1911 [67] G. L. BAYATIAN et al.: **CMS physics: Technical design report**. In: (2006) (see p. 22).

- 1912 [68] G L BAYATIAN, S CHATRCHYAN, G HMAYAKYAN, et al.: **CMS Physics: Technical Design**
 1913 **Report Volume 1: Detector Performance and Software.** Technical Design Report
 1914 CMS. There is an error on cover due to a technical problem for some items. Geneva:
 1915 CERN, 2006. URL: <https://cds.cern.ch/record/922757> (see pp. 22, 27, 54).
- 1916 [69] CMS COLLABORATION: **Detector Drawings.** CMS Collection. Mar. 2012. URL: <https://cds.cern.ch/record/1433717> (see p. 23).
- 1918 [70] S CHATRCHYAN, V KHACHATRYAN, A M SIRUNYAN, et al.: **Performance of the CMS Drift**
 1919 **Tube Chambers with Cosmic Rays.** In: *J. Instrum.*, 5:arXiv:0911.4855. CMS-CFT-
 1920 09-012 (Nov. 2009), T03015 . 47 p. URL: <http://cds.cern.ch/record/1223944> (see
 1921 pp. 25–26).
- 1922 [71] TOM DODINGTON: **News from the CMS experimental site: 22 November 2013.** 2013.
 1923 URL: <http://cms.web.cern.ch/news/news-point-5-22-november-2013> (see p. 26).
- 1924 [72] INSTITUTE OF RESEARCH INTO THE FUNDAMENTAL LAWS THE UNIVERSE: **The CMS**
 1925 **detector superconducting solenoid.** 2006. URL: http://irfu.cea.fr/en/Phocea/Vie_des_labos/Ast/ast_visu.php?id_ast=839 (see p. 28).
- 1927 [73] FERGUS WILSON: **Experimental Particle Physics.** 2012. URL: <http://slideplayer.com/slide/794631/> (see p. 28).
- 1929 [74] EMRAH TIRAS, BURAK BILKI, and YASAR ONEL: **Commissioning of CMS Forward**
 1930 **Hadron Calorimeters with Upgraded Multi-anode PMTs and μTCA Readout.** In:
 1931 (2016). arXiv: 1611.05232 [physics.ins-det] (see p. 29).
- 1932 [75] LUCAS TAYLOR: **Experimental Particle Physics.** 2011. URL: <http://cms.web.cern.ch/news/electromagnetic-calorimeter> (see p. 29).
- 1934 [76] **Proceedings, 34th International Conference on High Energy Physics (ICHEP 2008)** ■
 1935 URL: <http://www.slac.stanford.edu/econf/C080730> (see p. 29).
- 1936 [77] L. BRIANZA: **Precision crystal calorimetry in LHC Run II with the CMS ECAL.** In:
 1937 *Journal of Instrumentation*, 12:01 (2017), p. C01069. URL: <http://stacks.iop.org/1748-0221/12/i=01/a=C01069> (see pp. 30, 33).
- 1939 [78] SERGUEI CHATRCHYAN, VARDAN KHACHATRYAN, ALBERT M SIRUNYAN, et al.: **Description**
 1940 **and performance of track and primary-vertex reconstruction with the CMS**
 1941 **tracker.** In: *J. Instrum.*, 9:arXiv:1405.6569. CERN-PH-EP-2014-070. CMS-TRK-11-001
 1942 (May 2014). Comments: Replaced with published version. Added journal reference
 1943 and DOI, P10009. 80 p. URL: <http://cds.cern.ch/record/1704291> (see pp. 30, 57).
- 1944 [79] BY CHRISTINE SUTTON: **Chronicles of CMS: the saga of LS1.** In: (May 2015). URL:
 1945 <http://cds.cern.ch/record/2024986> (see p. 31).
- 1946 [80] **A beautiful barrel for CMS.** In: (Mar. 2014). URL: <http://cds.cern.ch/record/1998635> (see p. 31).
- 1948 [81] VARDAN KHACHATRYAN et al.: **The CMS trigger system.** In: *JINST*, 12:01 (2017),
 1949 P01020. doi: 10.1088/1748-0221/12/01/P01020. arXiv: 1609.02366 [physics.ins-det] ■
 1950 (see p. 32).
- 1951 [82] BY CORINNE PRALAVORIO and CORINNE PRALAVORIO: **Major work to ready the LHC**
 1952 **experiments for Run 2.** In: (May 2015). URL: <http://cds.cern.ch/record/2024977>
 1953 (see p. 32).

- 1954 [83] LUIGI GUIDUCCI: **CMS muon system towards LHC Run 2 and beyond.** Tech. rep.
 1955 CMS-CR-2014-333. Geneva: CERN, Oct. 2014. URL: <https://cds.cern.ch/record/1966038> (see p. 33).
- 1957 [84] CARLO BATTILANA: **The CMS muon system status and upgrades for LHC run-2 and**
 1958 **performance of muon reconstruction with 13 TeV data.** Tech. rep. CMS-CR-2016-
 1959 437. Geneva: CERN, Dec. 2016. URL: <http://cds.cern.ch/record/2239185> (see
 1960 p. 33).
- 1961 [85] SERGUEI CHATRCHYAN et al.: **Energy Calibration and Resolution of the CMS Elec-**
 1962 **tromagnetic Calorimeter in pp Collisions at $\sqrt{s} = 7$ TeV.** In: *JINST*, 8: (2013).
 1963 [JINST8,9009(2013)], P09009. doi: [10.1088/1748-0221/8/09/P09009](https://doi.org/10.1088/1748-0221/8/09/P09009). arXiv: [1306.2016 \[hep-ex\]](https://arxiv.org/abs/1306.2016) (see p. 33).
- 1965 [86] **Cool running for CMS tracker.** In: (Mar. 2014). URL: <http://cds.cern.ch/record/1998606> (see p. 33).
- 1967 [87] L. CADAMURO: **The CMS Level-1 trigger system for LHC Run II.** In: *Journal of*
 1968 *Instrumentation*, 12:03 (2017), p. C03021. URL: <http://stacks.iop.org/1748-0221/12/i=03/a=C03021> (see p. 33).
- 1970 [88] DAVID AARON MATZNER DOMINGUEZ, D. ABBANEO, K. ARNDT, et al.: **CMS Technical**
 1971 **Design Report for the Pixel Detector Upgrade.** In: (2012) (see p. 34).
- 1972 [89] HANNO CHRISTOPHER PERREY: **Plans and Status of the Phase I Upgrade of the**
 1973 **CMS Pixel Tracker.** Tech. rep. CMS-CR-2014-005. Geneva: CERN, Jan. 2014. URL:
 1974 <http://cds.cern.ch/record/1644757> (see p. 34).
- 1975 [90] CLAUDIO GRANDI, DAVID STICKLAND, LUCAS TAYLOR, ACHILLE PETRILLI, and ALAIN
 1976 HERVÉ: **CMS Computing Model: The "CMS Computing Model RTAG".** Tech. rep.
 1977 CMS-NOTE-2004-031. CERN-LHCC-2004-035. LHCC-G-083. Geneva: CERN, Dec.
 1978 2004. URL: <http://cds.cern.ch/record/814248> (see p. 34).
- 1979 [91] CHRISTOPH ECK, J KNOBLOCH, LESLIE ROBERTSON, et al.: **LHC computing Grid: Tech-**
 1980 **nical Design Report. Version 1.06 (20 Jun 2005).** Technical Design Report LCG.
 1981 Geneva: CERN, 2005. URL: <https://cds.cern.ch/record/840543> (see p. 34).
- 1982 [92] WORLDWIDE LHC COMPUTING GRID: **WorldWide LHC Computing Gird - 2017.** 2017.
 1983 URL: <http://wlcg-public.web.cern.ch> (see p. 35).
- 1984 [93] JOHN C. COLLINS, DAVISON E. SOPER, and GEORGE F. STERMAN: **Factorization of Hard**
 1985 **Processes in QCD.** In: *Adv. Ser. Direct. High Energy Phys.*, 5: (1989), pp. 1–91. doi:
 1986 [10.1142/9789814503266_0001](https://doi.org/10.1142/9789814503266_0001). arXiv: [hep-ph/0409313 \[hep-ph\]](https://arxiv.org/abs/hep-ph/0409313) (see p. 37).
- 1987 [94] RINGAILE PLACAKYTE: **Parton Distribution Functions.** In: *Proceedings, 31st Interna-*
 1988 *tional Conference on Physics in collisions (PIC 2011): Vancouver, Canada, August*
 1989 *28-September 1, 2011.* 2011. arXiv: [1111.5452 \[hep-ph\]](https://arxiv.org/abs/1111.5452). URL: <https://inspirehep.net/record/954990/files/arXiv:1111.5452.pdf> (see p. 37).
- 1991 [95] RICHARD D. BALL, VALERIO BERTONE, STEFANO CARRAZZA, et al.: **Parton distributions**
 1992 **for the LHC run II.** In: *Journal of High Energy Physics*, 2015:4 (2015), p. 40. doi:
 1993 [10.1007/JHEP04\(2015\)040](https://doi.org/10.1007/JHEP04(2015)040) (see p. 37).

- 1994 [96] JON BUTTERWORTH et al.: **PDF4LHC recommendations for LHC Run II**. In: *J. Phys.*, **G43**: (2016), p. 023001. doi: [10.1088/0954-3899/43/2/023001](https://doi.org/10.1088/0954-3899/43/2/023001). arXiv: [1510.03865](https://arxiv.org/abs/1510.03865) [hep-ph] (see pp. 37–38).
- 1997 [97] H. ABRAMOWICZ and A. CALDWELL: **HERA collider physics**. In: *Rev. Mod. Phys.*, **71**: (1999), pp. 1275–1410. doi: [10.1103/RevModPhys.71.1275](https://doi.org/10.1103/RevModPhys.71.1275). arXiv: [hep-ex/9903037](https://arxiv.org/abs/hep-ex/9903037) [hep-ex] (see p. 38).
- 2000 [98] STEPHEN HOLMES, RONALD S. MOORE, and VLADIMIR SHILTSEV: **Overview of the Tevatron Collider Complex: Goals, Operations and Performance**. In: *JINST*, **6**: (2011), T08001. doi: [10.1088/1748-0221/6/08/T08001](https://doi.org/10.1088/1748-0221/6/08/T08001). arXiv: [1106.0909](https://arxiv.org/abs/1106.0909) [physics.acc-ph] (see p. 38).
- 2004 [99] JUAN ROJO et al.: **The PDF4LHC report on PDFs and LHC data: Results from Run I and preparation for Run II**. In: *J. Phys.*, **G42**: (2015), p. 103103. doi: [10.1088/0954-3899/42/10/103103](https://doi.org/10.1088/0954-3899/42/10/103103). arXiv: [1507.00556](https://arxiv.org/abs/1507.00556) [hep-ph] (see p. 38).
- 2007 [100] ALAN D. MARTIN: **Proton structure, Partons, QCD, DGLAP and beyond**. In: *Acta Phys. Polon.*, **B39**: (2008), pp. 2025–2062. arXiv: [0802.0161](https://arxiv.org/abs/0802.0161) [hep-ph] (see p. 38).
- 2009 [101] J. PUMPLIN, D. STUMP, R. BROCK, et al.: **Uncertainties of predictions from parton distribution functions. 2. The Hessian method**. In: *Phys. Rev.*, **D65**: (2001), p. 014013. doi: [10.1103/PhysRevD.65.014013](https://doi.org/10.1103/PhysRevD.65.014013). arXiv: [hep-ph/0101032](https://arxiv.org/abs/hep-ph/0101032) [hep-ph] (see p. 38).
- 2012 [102] FRANZ MANDL and GRAHAM G SHAW: **Quantum field theory; 2nd ed.** New York, NY: Wiley, 2010. URL: <https://cds.cern.ch/record/1236742> (see p. 40).
- 2014 [103] S BANERJEE: **CMS Simulation Software**. In: *Journal of Physics: Conference Series*, **396**:2 (2012), p. 022003. URL: <http://stacks.iop.org/1742-6596/396/i=2/a=022003> (see p. 40).
- 2017 [104] M HILDRETH, V N IVANCHENKO, D J LANGE, and M J KORTELAINEN: **CMS Full Simulation for Run-2**. In: *Journal of Physics: Conference Series*, **664**:7 (2015), p. 072022. URL: <http://stacks.iop.org/1742-6596/664/i=7/a=072022> (see p. 40).
- 2020 [105] S. AGOSTINELLI, J. ALLISON, K. AMAKO, et al.: **Geant4-a simulation toolkit**. In: *Nuclear Instruments and Methods in Physics Research Section A: Accelerators, Spectrometers, Detectors and Associated Equipment*, **506**:3 (2003), pp. 250–303. doi: [https://doi.org/10.1016/S0168-9002\(03\)01368-8](https://doi.org/10.1016/S0168-9002(03)01368-8) (see pp. 40, 42).
- 2024 [106] MICHAEL H. SEYMOUR and MARILYN MARX: **Monte Carlo Event Generators**. In: *Proceedings, 69th Scottish Universities Summer School in Physics : LHC Phenomenology (SUSSP69): St.Andrews, Scotland, August 19-September 1, 2012*. 2013, pp. 287–319. doi: [10.1007/978-3-319-05362-2_8](https://doi.org/10.1007/978-3-319-05362-2_8). arXiv: [1304.6677](https://arxiv.org/abs/1304.6677) [hep-ph] (see p. 40).
- 2028 [107] TORBJORN SJÖSTRAND: **Monte Carlo Tools**. In: *Proceedings, 65th Scottish Universities Summer School in Physics: LHC Physics (SUSSP65): St. Andrews, UK, August 16-29, 2009*. 2009, pp. 309–339. doi: [10.1201/b11865-14](https://doi.org/10.1201/b11865-14). arXiv: [0911.5286](https://arxiv.org/abs/0911.5286) [hep-ph] (see p. 40).
- 2032 [108] STEFAN HÖCHE: **Introduction to parton-shower event generators**. In: *Proceedings, Theoretical Advanced Study Institute in Elementary Particle Physics: Journeys Through the Precision Frontier: Amplitudes for Colliders (TASI 2014): Boulder, Colorado, June 2-27, 2014*. 2015, pp. 235–295. doi: [10.1142/9789814678766_0005](https://doi.org/10.1142/9789814678766_0005). arXiv: [1411.4085](https://arxiv.org/abs/1411.4085) [hep-ph] (see pp. 40–41).

- 2037 [109] ADAM ALLOUL, NEIL D. CHRISTENSEN, CELINE DEGRANDE, CLAUDE DUHR, and BEN-
 2038 JAMIN FUKS: **FeynRules 2.0 - A complete toolbox for tree-level phenomenology**. In: *Comput. Phys. Commun.*, **185**: (2014), pp. 2250–2300. DOI: [10.1016/j.cpc.2014.04.012](https://doi.org/10.1016/j.cpc.2014.04.012). arXiv: [1310.1921 \[hep-ph\]](https://arxiv.org/abs/1310.1921) (see p. 40).
- 2041 [110] CELINE DEGRANDE, CLAUDE DUHR, BENJAMIN FUKS, et al.: **UFO - The Universal FeynRules Output**. In: *Comput. Phys. Commun.*, **183**: (2012), pp. 1201–1214. DOI: [10.1016/j.cpc.2012.01.022](https://doi.org/10.1016/j.cpc.2012.01.022). arXiv: [1108.2040 \[hep-ph\]](https://arxiv.org/abs/1108.2040) (see p. 40).
- 2044 [111] JOHAN ALWALL, MICHEL HERQUET, FABIO MALTONI, OLIVIER MATTELAER, and TIM STELZER: **MadGraph 5 : Going Beyond**. In: *JHEP*, **06**: (2011), p. 128. DOI: [10.1007/JHEP06\(2011\)128](https://doi.org/10.1007/JHEP06(2011)128). arXiv: [1106.0522 \[hep-ph\]](https://arxiv.org/abs/1106.0522) (see pp. 41, 44).
- 2047 [112] MICHELANGELO L. MANGANO, MAURO MORETTI, FULVIO PICCININI, and MICHELE TREC-
 2048 CANI: **Matching matrix elements and shower evolution for top-quark production**
 2049 **in hadronic collisions**. In: *JHEP*, **01**: (2007), p. 013. DOI: [10.1088/1126-6708/2007/01/013](https://doi.org/10.1088/1126-6708/2007/01/013). arXiv: [hep-ph/0611129 \[hep-ph\]](https://arxiv.org/abs/hep-ph/0611129) (see p. 41).
- 2051 [113] TORBJORN SJOSTRAND, STEFAN ASK, JESPER R. CHRISTIANSEN, et al.: **An introduction to {PYTHIA} 8.2**. In: *Computer Physics Communications*, **191**: (2015), pp. 159–177.
 2052 DOI: <http://dx.doi.org/10.1016/j.cpc.2015.01.024> (see pp. 41–42).
- 2054 [114] TORBJORN SJOSTRAND, STEPHEN MRENNA, and PETER Z. SKANDS: **PYTHIA 6.4 Physics and Manual**. In: *JHEP*, **0605**: (2006), p. 026. DOI: [10.1088/1126-6708/2006/05/026](https://doi.org/10.1088/1126-6708/2006/05/026). arXiv: [hep-ph/0603175 \[hep-ph\]](https://arxiv.org/abs/hep-ph/0603175) (see pp. 41–42).
- 2057 [115] TORBJORN SJOSTRAND, STEFAN ASK, JESPER R. CHRISTIANSEN, et al.: **An Introduction to PYTHIA 8.2**. In: *Comput. Phys. Commun.*, **191**: (2015), pp. 159–177. DOI: [10.1016/j.cpc.2015.01.024](https://doi.org/10.1016/j.cpc.2015.01.024). arXiv: [1410.3012 \[hep-ph\]](https://arxiv.org/abs/1410.3012) (see pp. 41–42, 44).
- 2060 [116] JOHAN ALWALL et al.: **Comparative study of various algorithms for the merging of parton showers and matrix elements in hadronic collisions**. In: *Eur. Phys. J.*, **C53**: (2008), pp. 473–500. DOI: [10.1140/epjc/s10052-007-0490-5](https://doi.org/10.1140/epjc/s10052-007-0490-5). arXiv: [0706.2569 \[hep-ph\]](https://arxiv.org/abs/0706.2569) (see p. 41).
- 2064 [117] J. ALWALL, R. FREDERIX, S. FRIXIONE, et al.: **The automated computation of tree-level and next-to-leading order differential cross sections, and their matching to parton shower simulations**. In: *JHEP*, **07**: (2014), p. 079. DOI: [10.1007/JHEP07\(2014\)079](https://doi.org/10.1007/JHEP07(2014)079). arXiv: [1405.0301 \[hep-ph\]](https://arxiv.org/abs/1405.0301) (see pp. 41, 44).
- 2068 [118] RIKKERT FREDERIX and STEFANO FRIXIONE: **Merging meets matching in MC@NLO**. In: *JHEP*, **12**: (2012), p. 061. DOI: [10.1007/JHEP12\(2012\)061](https://doi.org/10.1007/JHEP12(2012)061). arXiv: [1209.6215 \[hep-ph\]](https://arxiv.org/abs/1209.6215) (see p. 41).
- 2071 [119] SIMONE ALIOLI, PAOLO NASON, CARLO OLEARI, and EMANUELE RE: **A general framework for implementing NLO calculations in shower Monte Carlo programs: the POWHEG BOX**. In: *Journal of High Energy Physics*, **2010**:6 (2010), p. 43. DOI: [10.1007/JHEP06\(2010\)043](https://doi.org/10.1007/JHEP06(2010)043) (see p. 41).
- 2075 [120] SIMONE ALIOLI, PAOLO NASON, CARLO OLEARI, and EMANUELE RE: **NLO single-top production matched with shower in POWHEG: s - and t -channel contributions**. In: *Journal of High Energy Physics*, **2009**:09 (2009), p. 111. URL: <http://stacks.iop.org/1126-6708/2009/i=09/a=111> (see p. 41).

- 2079 [121] STEFANO FRIXIONE, PAOLO NASON, and CARLO OLEARI: Matching NLO QCD computations with parton shower simulations: the POWHEG method. In: *Journal of High Energy Physics*, **2007**:11 (2007), p. 070. URL: <http://stacks.iop.org/1126-6708/2007/i=11/a=070> (see p. 41).
- 2080
2081
2082
- 2083 [122] SIMONE ALIOLI, PAOLO NASON, CARLO OLEARI, and EMANUELE RE: A general framework for implementing NLO calculations in shower Monte Carlo programs: the POWHEG BOX. In: *JHEP*, **06**: (2010), p. 043. doi: [10.1007/JHEP06\(2010\)043](https://doi.org/10.1007/JHEP06(2010)043). arXiv: [1002.2581 \[hep-ph\]](https://arxiv.org/abs/1002.2581) (see p. 41).
- 2087 [123] STEFANO FRIXIONE, PAOLO NASON, and CARLO OLEARI: Matching NLO QCD computations with Parton Shower simulations: the POWHEG method. In: *JHEP*, **11**: (2007), p. 070. doi: [10.1088/1126-6708/2007/11/070](https://doi.org/10.1088/1126-6708/2007/11/070). arXiv: [0709.2092 \[hep-ph\]](https://arxiv.org/abs/0709.2092) (see p. 41).
- 2091 [124] PAOLO NASON: A New method for combining NLO QCD with shower Monte Carlo algorithms. In: *JHEP*, **11**: (2004), p. 040. doi: [10.1088/1126-6708/2004/11/040](https://doi.org/10.1088/1126-6708/2004/11/040). arXiv: [hep-ph/0409146 \[hep-ph\]](https://arxiv.org/abs/hep-ph/0409146) (see p. 41).
- 2094 [125] ANDREI V. GRITSAN, RAOUL RÖNTSCH, MARKUS SCHULZE, and MENG XIAO: Constraining anomalous Higgs boson couplings to the heavy flavor fermions using matrix element techniques. In: *Phys. Rev.*, **D94**:5 (2016), p. 055023. doi: [10.1103/PhysRevD.94.055023](https://doi.org/10.1103/PhysRevD.94.055023). arXiv: [1606.03107 \[hep-ph\]](https://arxiv.org/abs/1606.03107) (see pp. 41, 44).
- 2098 [126] IAN ANDERSON et al.: Constraining anomalous HVV interactions at proton and lepton colliders. In: *Phys. Rev.*, **D89**:3 (2014), p. 035007. doi: [10.1103/PhysRevD.89.035007](https://doi.org/10.1103/PhysRevD.89.035007). arXiv: [1309.4819 \[hep-ph\]](https://arxiv.org/abs/1309.4819) (see pp. 41, 44).
- 2101 [127] SARA BOLOGNESI, YANYAN GAO, ANDREI V. GRITSAN, et al.: On the spin and parity of a single-produced resonance at the LHC. In: *Phys. Rev.*, **D86**: (2012), p. 095031. doi: [10.1103/PhysRevD.86.095031](https://doi.org/10.1103/PhysRevD.86.095031). arXiv: [1208.4018 \[hep-ph\]](https://arxiv.org/abs/1208.4018) (see pp. 41, 44).
- 2104 [128] YANYAN GAO, ANDREI V. GRITSAN, ZIJIN GUO, et al.: Spin determination of single-produced resonances at hadron colliders. In: *Phys. Rev.*, **D81**: (2010), p. 075022. doi: [10.1103/PhysRevD.81.075022](https://doi.org/10.1103/PhysRevD.81.075022). arXiv: [1001.3396 \[hep-ph\]](https://arxiv.org/abs/1001.3396) (see pp. 41, 44).
- 2107 [129] PIERRE ARTOISENET, RIKKERT FREDERIX, OLIVIER MATTELAER, and ROBBERT RIETKERK: Automatic spin-entangled decays of heavy resonances in Monte Carlo simulations. In: *JHEP*, **03**: (2013), p. 015. doi: [10.1007/JHEP03\(2013\)015](https://doi.org/10.1007/JHEP03(2013)015). arXiv: [1212.3460 \[hep-ph\]](https://arxiv.org/abs/1212.3460) (see pp. 42, 44).
- 2111 [130] V. KHACHATRYAN and ETAL: Event generator tunes obtained from underlying event and multiparton scattering measurements. In: *The European Physical Journal C*, **76**:3 (Mar. 17, 2016), p. 155. doi: [10.1140/epjc/s10052-016-3988-x](https://doi.org/10.1140/epjc/s10052-016-3988-x) (see p. 42).
- 2114 [131] YUE ZHANG, Bo HUA LI, CHONG SHENG LI, JUN GAO, and HUA XING ZHU: Next-to-leading order QCD corrections to the top quark associated with γ production via model-independent flavor-changing neutral-current couplings at hadron colliders. In: *Phys. Rev.*, **D83**: (2011), p. 094003. doi: [10.1103/PhysRevD.83.094003](https://doi.org/10.1103/PhysRevD.83.094003). arXiv: [1101.5346 \[hep-ph\]](https://arxiv.org/abs/1101.5346) (see p. 43).
- 2119 [132] A. HOECKER, P. SPECKMAYER, J. STELZER, et al.: TMVA - Toolkit for Multivariate Data Analysis. In: *ArXiv Physics e-prints*, (Mar. 2007). eprint: [physics/0703039](https://arxiv.org/abs/physics/0703039) (see pp. 46–47).
- 2120
2121

- 2122 [133] R. BRUN and F. RADEMAKERS: **ROOT: An object oriented data analysis framework.**
 2123 In: *Nucl. Instrum. Meth.*, **A389**: (1997), pp. 81–86. DOI: [10.1016/S0168-9002\(97\)00048-X](https://doi.org/10.1016/S0168-9002(97)00048-X) (see p. 46).
- 2125 [134] A. MAYR, H. BINDER, O. GEFELLER, and M. SCHMID: **The Evolution of Boosting
 2126 Algorithms - From Machine Learning to Statistical Modelling.** In: *ArXiv e-prints*,
 2127 (Mar. 2014). arXiv: [1403.1452 \[stat.ME\]](https://arxiv.org/abs/1403.1452) (see p. 47).
- 2128 [135] OLAF BEHNKE, KEVIN KRONINGER, GREGORY SCHOTT, and THOMAS SCHORNER-SADENIUS: **Data Analysis in High Energy Physics: A Practical Guide to Statistical Methods.** 1st.
 2129 Wiley-VCH, 2013 (see pp. 47–48).
- 2131 [136] CHRISTIAN BÖSER, SIMON FINK, and STEFFEN RÖCKER: **Introduction to Boosted
 2132 Decision Trees: A multivariate approach to classification problems.** Presented at
 2133 the 'KSETA Doktoranden' workshop, Lauterbad. July 2014. URL: <https://indico.scc.kit.edu/indico/event/48/session/4/contribution/35/material/slides/0.pdf> (see
 2135 p. 48).
- 2136 [137] SERGUEI CHATRCHYAN et al.: **Combined results of searches for the standard model
 2137 Higgs boson in pp collisions at $\sqrt{s} = 7$ TeV.** In: *Phys. Lett.*, **B710**: (2012), pp. 26–
 2138 48. DOI: [10.1016/j.physletb.2012.02.064](https://doi.org/10.1016/j.physletb.2012.02.064). arXiv: [1202.1488 \[hep-ex\]](https://arxiv.org/abs/1202.1488) (see p. 48).
- 2139 [138] GLEN COWAN, KYLE CRANMER, EILAM GROSS, and OFER VITELLS: **Asymptotic formulae
 2140 for likelihood-based tests of new physics.** In: *Eur. Phys. J.*, **C71**: (2011). [Erratum:
 2141 *Eur. Phys. J.* C73,2501(2013)], p. 1554. DOI: [10.1140/epjc/s10052-011-1554-0](https://doi.org/10.1140/epjc/s10052-011-1554-0), [10.1140/epjc/s10052-013-2501-z](https://doi.org/10.1140/epjc/s10052-013-2501-z). arXiv: [1007.1727 \[physics.data-an\]](https://arxiv.org/abs/1007.1727) (see
 2143 pp. 48, 52).
- 2144 [139] **Observation of a new boson with a mass near 125 GeV.** Tech. rep. CMS-PAS-HIG-
 2145 12-020. Geneva: CERN, 2012. URL: <https://cds.cern.ch/record/1460438> (see pp. 48,
 2146 52).
- 2147 [140] **Procedure for the LHC Higgs boson search combination in Summer 2011.** Tech.
 2148 rep. CMS-NOTE-2011-005. ATL-PHYS-PUB-2011-11. Geneva: CERN, Aug. 2011. URL:
 2149 [http://cds.cern.ch/record/1379837](https://cds.cern.ch/record/1379837) (see pp. 48, 50–52).
- 2150 [141] HIGGS WORKING GROUP: **Documentation of the RooStats based statistics tools
 2151 for Higgs PAG.** 2017. URL: [SWGuideHiggsAnalysisCombinedLimit](https://twiki.cern.ch/twiki/bin/viewauth/CMS/

 2152 <a href=) (see p. 48).
- 2153 [142] LORENZO MONETA, KEVIN BELASCO, KYLE S. CRANMER, et al.: **The RooStats Project.**
 2154 In: *PoS, ACAT2010*: (2010), p. 057. arXiv: [1009.1003 \[physics.data-an\]](https://arxiv.org/abs/1009.1003) (see p. 48).
- 2155 [143] GLEN COWAN, KYLE CRANMER, EILAM GROSS, and OFER VITELLS: **Asymptotic formulae
 2156 for likelihood-based tests of new physics.** In: *The European Physical Journal C*, **71**:2
 2157 (Feb. 2011). DOI: [10.1140/epjc/s10052-011-1554-0](https://doi.org/10.1140/epjc/s10052-011-1554-0). arXiv: [1007.1727 \[hep-ph\]](https://arxiv.org/abs/1007.1727) (see
 2158 p. 48).
- 2159 [144] THOMAS JUNK: **Confidence level computation for combining searches with small
 2160 statistics.** In: *Nuclear Instruments and Methods in Physics Research Section A: Accelerators,
 2161 Spectrometers, Detectors and Associated Equipment*, **434**:2 (1999), pp. 435–443.
 2162 DOI: [https://doi.org/10.1016/S0168-9002\(99\)00498-2](https://doi.org/10.1016/S0168-9002(99)00498-2) (see p. 49).

- 2163 [145] AL READ: **Presentation of search results: the CL s technique.** In: *Journal of Physics G: Nuclear and Particle Physics*, **28**:10 (2002), p. 2693. URL: <http://stacks.iop.org/0954-3899/28/i=10/a=313> (see p. 49).
- 2166 [146] J. S. CONWAY: **Incorporating Nuisance Parameters in Likelihoods for Multisource Spectra.** In: *Proceedings, PHYSTAT 2011 Workshop on Statistical Issues Related to Discovery Claims in Search Experiments and Unfolding, CERN, Geneva, Switzerland 17-20 January 2011*. 2011, pp. 115–120. doi: [10.5170/CERN-2011-006.115](https://doi.org/10.5170/CERN-2011-006.115). arXiv: [1103.0354 \[physics.data-an\]](https://arxiv.org/abs/1103.0354) (see p. 51).
- 2171 [147] A. M. SIRUNYAN et al.: **Particle-flow reconstruction and global event description with the CMS detector.** In: *JINST*, **12**: (2017), P10003. doi: [10.1088/1748-0221/12/10/P10003](https://doi.org/10.1088/1748-0221/12/10/P10003). arXiv: [1706.04965 \[physics.ins-det\]](https://arxiv.org/abs/1706.04965) (see pp. 53–54, 57, 60, 62, 64).
- 2174 [148] R. FRÜHWIRTH: **Application of Kalman filtering to track and vertex fitting.** In: *Nuclear Instruments and Methods in Physics Research Section A: Accelerators, Spectrometers, Detectors and Associated Equipment*, **262**:2 (1987), pp. 444–450. doi: [http://dx.doi.org/10.1016/0168-9002\(87\)90887-4](http://dx.doi.org/10.1016/0168-9002(87)90887-4) (see p. 55).
- 2178 [149] PIERRE BILLOIR: **Progressive track recognition with a Kalman like fitting procedure.** In: *Comput. Phys. Commun.*, **57**: (1989), pp. 390–394. doi: [10.1016/0010-4655\(89\)90249-X](https://doi.org/10.1016/0010-4655(89)90249-X) (see p. 55).
- 2181 [150] SERGUEI CHATRHYAN et al.: **Performance of CMS muon reconstruction in pp collision events at $\sqrt{s} = 7$ TeV.** In: *JINST*, **7**: (2012), P10002. doi: [10.1088/1748-0221/7/10/P10002](https://doi.org/10.1088/1748-0221/7/10/P10002). arXiv: [1206.4071 \[physics.ins-det\]](https://arxiv.org/abs/1206.4071) (see p. 55).
- 2184 [151] W ADAM, R FRÜHWIRTH, A STRANDLIE, and T TODOROV: **Reconstruction of electrons with the Gaussian-sum filter in the CMS tracker at the LHC.** In: *Journal of Physics G: Nuclear and Particle Physics*, **31**:9 (2005), N9. URL: <http://stacks.iop.org/0954-3899/31/i=9/a=N01> (see p. 56).
- 2188 [152] **Performance of electron reconstruction and selection with the CMS detector in proton-proton collisions at $\sqrt{s} = 8\text{TeV}$.** In: *Journal of Instrumentation*, **10**:06 (2015), P06005. URL: <http://stacks.iop.org/1748-0221/10/i=06/a=P06005> (see p. 57).
- 2191 [153] **Electron and photon performance in CMS with the full 2016 data sample.** In: (Mar. 2017). URL: <http://cds.cern.ch/record/2255497> (see pp. 57, 64–65).
- 2193 [154] K. ROSE: **Deterministic annealing for clustering, compression, classification, regression, and related optimization problems.** In: *Proceedings of the IEEE*, **86**:11 (Nov. 1998), pp. 2210–2239. doi: [10.1109/5.726788](https://doi.org/10.1109/5.726788) (see p. 57).
- 2196 [155] WOLFGANG WALTENBERGER: **Adaptive Vertex Reconstruction.** Tech. rep. CMS-NOTE-2008-033. Geneva: CERN, July 2008. URL: <https://cds.cern.ch/record/1166320> (see p. 57).
- 2199 [156] ANDREAS KORNMAYER: **The CMS Pixel Luminosity Telescope.** Tech. rep. CMS-CR-2015-121. Geneva: CERN, June 2015. URL: <https://cds.cern.ch/record/2039978> (see p. 60).
- 2202 [157] **CMS Luminosity Measurements for the 2016 Data Taking Period.** Tech. rep. CMS-PAS-LUM-17-001. Geneva: CERN, 2017. URL: <http://cds.cern.ch/record/2257069> (see pp. 60–61).

- 2205 [158] **Pileup Removal Algorithms.** Tech. rep. CMS-PAS-JME-14-001. Geneva: *CERN*, 2014.
 2206 URL: <http://cds.cern.ch/record/1751454> (see p. 61).
- 2207 [159] **Muon Identification and Isolation efficiency on full 2016 dataset.** In: (Mar. 2017).
 2208 URL: <http://cds.cern.ch/record/2257968> (see pp. 61–63).
- 2209 [160] **Effective areas used for Summer16 samples.** 2017. URL: https://indico.cern.ch/event/482673/contributions/2187022/%20attachments/1282446/1905912/talk_electron_ID_spring16.pdf (see p. 64).
- 2212 [161] MATTEO CACCIARI, GAVIN P. SALAM, and GREGORY SOYEZ: **The Anti-k(t) jet clustering algorithm.** In: *JHEP*, **04**: (2008), p. 063. DOI: <10.1088/1126-6708/2008/04/063>. arXiv: [0802.1189 \[hep-ph\]](0802.1189) (see p. 66).
- 2215 [162] **Jet algorithms performance in 13 TeV data.** Tech. rep. CMS-PAS-JME-16-003. Geneva: *CERN*, 2017. URL: <http://cds.cern.ch/record/2256875> (see p. 66).
- 2217 [163] V. KHACHATRYAN et al.: **Jet energy scale and resolution in the CMS experiment in pp collisions at 8 TeV.** In: *Journal of Instrumentation*, **12**:02 (2017), P02014. URL: <http://stacks.iop.org/1748-0221/12/i=02/a=P02014> (see p. 67).
- 2220 [164] **Jet energy scale and resolution performances with 13TeV data.** In: (June 2016). URL: <http://cds.cern.ch/record/2160347> (see pp. 67–68).
- 2222 [165] THE CMS COLLABORATION: **Identification of b-quark jets with the CMS experiment.** In: *Journal of Instrumentation*, **8**:04 (2013), P04013. URL: <http://stacks.iop.org/1748-0221/8/i=04/a=P04013> (see p. 68).
- 2225 [166] **Identification of b quark jets at the CMS Experiment in the LHC Run 2.** Tech. rep. CMS-PAS-BTV-15-001. Geneva: *CERN*, 2016. URL: <http://cds.cern.ch/record/2138504> (see pp. 68, 70).
- 2228 [167] NAZAR BARTOSIK: **Diagram showing the common principle of identification of jets initiated by b-hadron decays.** 2016. URL: http://bartosik.pp.ua/hep_sketches/btagging (see p. 69).
- 2231 [168] **Identification of b quark jets at the CMS Experiment in the LHC Run 2.** Tech. rep. CMS-PAS-BTV-16-001. unpublished. Geneva: *CERN*, 2017 (see pp. 70–71).
- 2233 [169] **Performance of missing energy reconstruction in 13 TeV pp collision data using the CMS detector.** Tech. rep. CMS-PAS-JME-16-004. Geneva: *CERN*, 2016. URL: <http://cds.cern.ch/record/2205284> (see pp. 71, 76–77).
- 2236 [170] JORDAN DAMGOV: **Missing Et Optional Filters Run 2.** 2017. URL: <https://twiki.cern.ch/twiki/bin/viewauth/CMS/MissingETOptionalFiltersRun2> (see p. 76).
- 2238 [171] **EGM corrections for Moriond17.** URL: https://indico.cern.ch/event/613162/contributions/2472046/attachments/1410308/2156822/EGMSmearerAndRegression_PPD_022017.pdf (see p. 80).
- 2241 [172] **Misalignment and Muon Scale corrections.** URL: https://www-cdf.fnal.gov/~jyhan/cms_momscl/rochcor_cmsnote.pdf (see p. 80).
- 2243 [173] **Rochestor Correction.** Accessed: 2017-05-20. URL: <https://twiki.cern.ch/twiki/bin/viewauth/CMS/RochcorMuon> (see p. 80).